2015

Photoelectrons and Recombining Electrons in Atomic and Molecular Systems

Kristen D'Ann Fulfer
Louisiana State University and Agricultural and Mechanical College

Recommended Citation
Fulfer, Kristen D'Ann, "Photoelectrons and Recombining Electrons in Atomic and Molecular Systems" (2015). *LSU Doctoral Dissertations*. 1291.
https://digitalcommons.lsu.edu/gradschool_dissertations/1291

PHOTOELECTRONS AND RECOMBINING ELECTRONS IN ATOMIC AND MOLECULAR SYSTEMS

A Dissertation

Submitted to the Graduate Faculty of the
Louisiana State University and
Agricultural and Mechanical College
in partial fulfillment of the
requirements for the degree of
Doctor of Philosophy

in

The Department of Chemistry

by
Kristen D'Ann Fulfer
B.S., Texas State University - San Marcos, 2009
May 2015

This dissertation is dedicated to my loving husband, Bradford, who supported me and encouraged me throughout, and to my parents, Scott and Pam.

ACKNOWLEDGEMENTS

I would like to acknowledge my advisor, Dr. Erwin Poliakoff, who was an always patient and constant source of motivation.

TABLE OF CONTENTS

LIST OF TABLES

LIST OF FIGURES

LIST OF EQUATIONS

LIST OF ABBREVIATIONS AND SYMBOLS

B_0	amplitude of the magnetic component of electromagnetic radiation
θ	angle
ω	angular frequency
β	asymmetry parameter
β	beta parameter describing time a free electron spends in an electric field
BOA	Born-Oppenheimer Approximation
μ	dipole moment operator
e	charge of an electron
CCD	charge coupled device
CPA	chirped pulse amplification
CMOS	complimentary metal-oxide semiconductor
DNA	deoxyribonucleic acid
F	electric field strength
t_0	electron birthing time
t_r	electron recombination time
μ_{el}	electronic dipole moment operator
r	electronic distance
F	electronic factor
$\hat{T}_e$	electronic kinetic energy operator
eV	electron volt
ϕ	electronic wavefunction
E	energy
FCF	Franck-Condon Factor
ν	frequency

ω_t	frequency of an electron tunneling through a barrier
fwhm	full width at half maximum
hwp	half wave plate
$\widehat{H}$	Hamiltonian operator
n	harmonic order
HITS	High Intensity Tunable Source
HHG	high-order harmonic generation
I	intensity
r_i	inner radius
R	internuclear distance
I_p	ionization energy
JRM	James R. MacDonald Laboratory
KLS	Kansas Light Source
K	K-parameter
γ	Keldysh parameter
m_e	mass of an electron
MCP	microchannel plate
μ_n	nuclear dipole moment operator
$\hat{T}_N$	nuclear kinetic energy operator
χ	nuclear wavefunction
r_o	outer radius
E_p	pass energy
h	Planck’s Constant
λ_0	period of a magnet array
$h\nu$	photon energy

U_p	ponderamotive energy
$\hat{V}_{ee}$	potential energy operator for electron-electron interactions
$\hat{V}_{eN}$	potential energy operator for electron-nuclear interactions
$\hat{V}_{NN}$	potential energy operator for nuclear-nuclear interactions
qwp	quarter wave plate
m_0	resting mass of an electron
S	slit
c	speed of light
TRPES	time-resolved photoelectron spectroscopy
TOPAS	tunable optical parametric amplifier
UV	ultraviolet
U10	undulator of period length 10 cm
R	vibrational branching ratio
σ_v	vibrational cross section
q	vibrational mode coordinate
V	voltage
ψ	wavefunction
EXAFS	X-ray absorption fine structure
XANES	X-ray absorption near-edge structure

ABSTRACT

The work in this dissertation explores how photoelectrons enter and exit atoms and molecules. The electron rescattering events which may occur during photoionization or photorecombination processes play a dominant role in the understanding of how photoelectrons enter and exit molecules, which is intrinsically linked to how chemical reactions occur. Chapters 3-4 of this dissertation present evidence of vibrational mode specific breakdown of the Franck-Condon Principle in the photoionization of low symmetry molecules, acrolein and the singly halogenated thiophenes, due to resonant and non-resonant electron rescattering dynamics. In Chapters 5-6, the disentanglement of the valence electronic structure, as well as evidence for low-energy shape resonances, of the pyrimidine-type nucleobases, thymine, uracil, and cytosine, is shown using high-resolution photoelectron spectroscopy. Chapters 7-8 discuss the use of elliptically polarized light for high-order harmonic generation as a probe for electron rescattering dynamics in the gas-phase medium.

CHAPTER 1
INTRODUCTION AND SPECTROSCOPIC BACKGROUND

1.1 INTRODUCTION

The process of photoionization was first described by Albert Einstein in 1905 as the interaction between an atom or molecule and a high energy photon, which results in the ejection of an electron from the system.[1] Einstein's view of photoionization was suggested in the form of the following equation:

$$h\nu = I_p + \frac{1}{2}m_e v^2 \qquad \text{(Equation 1.1)}$$

where h is Planck's constant, ν is the frequency of the light, I_p is the ionization energy of the atom or molecule, m_e is the mass of an electron, and v is the velocity of the emitted electron. In photoionization, the kinetic energy of the photoelectron depends only on the photon energy, not on the intensity of the light. Since Einstein's first description, much has been learned about the various dynamics which occur during photoionization. Also, experimental methods and instrumentation have come a long way in the past 100 years, allowing for higher energy resolved, time resolved, and angular resolved measurements, increasing the knowledge of photoionization processes and electronic structure for many systems. At this point, photoionization is an established technique for elucidating the electronic structure of atoms and molecules.

While photoionization has been an active research field for at least the past 50 years, photorecombination is a relatively new concept, having been introduced in 1993.[2,3] Photorecombination is the final step of high-order harmonic generation (HHG),[3] and it is most simply viewed as the inverse of photoionization. The photorecombination process consists of a high-energy electron recombining with the parent ion and, in turn, releasing a high-energy photon, which contains information about both the electron/parent ion pair and the laser pulse from which it was created. With the further development of ultrafast lasers in the past few decades, much theoretical and experimental work has been done in the field of high-order harmonic generation.

Electron rescattering dynamics are known to occur in both photoionization and photorecombination processes. Electron dynamics occurring during photoionization describe how electrons are ejected from matter, which is important biologically in studying the damage of DNA by UV radiation, for instance. While photoionization spectroscopy techniques are well established, much about how the photoelectron leaves a molecule is still being discovered. Thus, one of the more interesting purposes of studying electron rescattering dynamics in polyatomic systems is that these dynamics are an relatively easy to manage example of how scattering processes affect molecules, which further provides valuable insight into how photoelectrons exit polyatomic systems. However, studying these dynamics also provides information about the electronic orbitals of a system; thus for a molecule, the study of the rescattering dynamics provides much insight into the molecular bonding within the system. These dynamics are also often connected to the geometry of the atomic or molecular system in which they occur. Thus, studying electron rescattering dynamics, either from the photoionization or the photorecombination point of view, can also provide information about the geometry, or rapid geometry changes, in a system.

In this dissertation, both photoelectron and HHG studies, which seek to further explore the electron rescattering dynamics of atoms and molecules, will be presented. An explanation of the experimental details is found in Chapter 2, Experimental Details. The $\widetilde{X}\ {}^2A'$ ionic state of acrolein, the $\tilde{B}\ {}^2A'$ states of several halogenated thiophenes, and the four outermost valence electronic states of the pyrimidine-type nucleobases, thymine, uracil, and cytosine, were all studied using energy-dependent high-resolution photoelectron spectroscopy. The acrolein studies showed mode-specific Franck-Condon breakdown due to shape resonances; these results are discussed in Chapter 3, Mode-Specific Non-Franck-Condon Behavior in Acrolein $\widetilde{X}\ {}^2A'$. A review of the halogenated thiophene results is found in Chapter 4, Photon Energy Dependence of the Photoelectron Spectra of the Halogenated Thiophenes. The electronic structure elucidation of the pyrimidine-type nucleobases is discussed in Chapter 5, Photoelectron Spectroscopy of the Pyrimidine-Type Nucleobases. In Chapter 6, Low Energy Shape Resonances in the Pyrimidine-Type Nucleobases, experimental results hinting at the presence of low-energy shape resonances in the nucleobases is shown. Chapters 7-8, Ellipticity Dependence of High-Order Harmonic Generation from Atomic Targets and Ellipticity Dependence of High-Order Harmonic Generation from CF_4, respectively, focus on HHG experiments, which used elliptically polarized laser pulses to probe electron rescattering dynamics in the following media: Ar, Kr and CF_4.

1.2 BORN-OPPENHEIMER APPROXIMATION

The reasoning behind the Born-Oppenheimer Approximation (BOA)[4] can be explained from classical principles as a simple mass difference. Atomic nuclei are several orders of magnitude larger in mass than a single electron. Thus, when a force is applied to the molecule, the electron will accelerate faster than the nuclei, since force, $F = ma$, where m is mass, and a is acceleration. So, even from a classical point of view, it is obvious that an electronic transition will occur on a different time scale than a nuclear transition.[5]

From this classical picture, Born and Oppenheimer argued that the electronic and nuclear contributions to the Hamiltonian operator could be considered separately.[4] The Hamiltonian can be written as a sum of nuclear and electronic terms, as follows:[6]

$$\hat{H} = \hat{T}_N + \hat{T}_e + \hat{V}_{ee} + \hat{V}_{eN} + \hat{V}_{NN} \qquad \text{(Equation 1.2)}$$

where $\hat{T}_N$ and $\hat{T}_e$ are the kinetic energy operators for the nuclei and electrons, respectively, and $\hat{V}_{ee}$, $\hat{V}_{eN}$ and $\hat{V}_{NN}$ are the potential energy operators for electron-electron, electron-nuclear, and nuclear-nuclear Coulombic interactions, respectively. To separate the electronic and nuclear terms in the Hamiltonian, it must be assumed that the nuclei are frozen during an electronic transition. By holding the nuclei as fixed during the electronic transition, the operator $\hat{T}_N$ can be neglected (infinitely large mass) and $\hat{V}_{NN}$ taken as a constant value. Now, Equation 1.2 can be rewritten as

$$\hat{H}_e = \hat{T}_e + \hat{V}_{ee} + \hat{V}_{eN} \qquad \text{(Equation 1.3)}$$

It then follows that the Schrodinger equation for the electronic transition is written as

$$\hat{H}_e \psi_i(r; R) = E_i(R) \psi_i(r; R) \qquad \text{(Equation 1.4)}$$

So that R is the fixed nuclear separation, r is the electronic distance, $E_i(R)$ is the electronic energy, and

$$\psi_i(r;R) = \chi_i\phi_i \qquad \text{(Equation 1.5)}$$

is the wavefunction composed of an electronic term, ϕ_i, and a nuclear term, χ_i. Furthermore, the electronic and nuclear terms can be considered separately; this approximation is known as the Born-Oppenheimer Approximation.

1.3 FRANCK-CONDON PRINCIPLE

In 1926, James Franck published his theory about the role of internuclear distance in the photodissociation of diatomic molecules.[7] Franck noticed that upon dissociating in ionization processes, molecules are able to emit radiation, which is multiple orders of magnitude larger than the minimum energy required for dissociation. Franck concluded that the internuclear distance for the molecule in the excited state relative to the ground state is inversely proportional to the change in dissociation energy. For many systems, the internuclear distance for the molecule in the excited state is larger than that of the ground state, so the dissociation energy is smaller for the excited state than for the ground state. Franck also noted the radiation would not only electronically excite the molecule, but that the nuclear potential would be altered upon electronic excitation since transitions occur vertically (constant internuclear distance). The excited state nuclear potential can then aid in the dissociation of the molecule.

Also in 1926, Edward Condon published a paper expanding on Franck's theory and introducing a quantitative explanation for the relative peak intensities of spectral lines.[8] Condon's paper discussed his theory that the vibrational state population distributions from electronic transitions should be constants; this theory is now known as the Franck-Condon Principle.

The Franck-Condon Principle follows directly from the BOA. When calculating a vibrational cross section, the electronic and nuclear terms can be separated, as in Equation 1.5:

$$\sigma_{v^+} \approx |\langle \chi^+ \varphi^+ | \mu | \chi_0 \varphi_0 \rangle|^2 \qquad \text{(Equation 1.6)}$$

where μ is the dipole moment operator. The dipole moment operator can be written as

$$\mu = \mu_{el} + \mu_n \qquad \text{(Equation 1.7)}$$

where μ_{el} is the electronic dipole moment operator, and μ_n is the nuclear dipole moment operator. From Equation 1.7, Equation 1.6 can be rewritten as

$$\sigma_{v^+} = |\langle \chi^+ \varphi^+ | \mu_{el} | \chi_0 \varphi_0 \rangle + \langle \chi^+ \varphi^+ | \mu_n | \chi_0 \varphi_0 \rangle|^2 \qquad \text{(Equation 1.8)}$$

The second half of Equation 1.8 can be written as

$$\langle \chi^+ \varphi^+ | \mu_n | \chi_0 \varphi_0 \rangle = \langle \chi^+ | \mu_n | \chi_0 \rangle \langle \varphi^+ | \varphi_0 \rangle \qquad \text{(Equation 1.9)}$$

However, since the ground and excited electronic states are orthogonal to one another, Equation 1.9 goes to zero. Further, since the electronic dipole moment operator affects only on the electronic components of the wavefunction, so we can rewrite the vibrational cross section as

$$\sigma_{v^+} = |\chi^+ \langle \varphi^+ | \mu_{el} | \varphi_0 \rangle \chi_0|^2 \qquad \text{(Equation 1.10)}$$

Since the inner matrix element in Equation 1.10 is generally considered to be slowly varying as a function of time, it is a reasonable approximation to completely separate the vibrational and electronic components into separate integrals, as follows:

$$\sigma_{v^+} = |\langle \chi^+ | \chi_0 \rangle|^2 \times |\langle \varphi^+ | \mu_{el} | \varphi_0 \rangle|^2 \qquad \text{(Equation 1.11)}$$

From Equation 1.11, it is apparent that the vibrational components of the wavefunction are not operated on. The squared integral containing only the vibrational wavefunctions, $|\langle \chi^{+} | \chi_0 \rangle|^2$, is then independent of the electronic dipole moment and thus independent of the incident photon energy which induces the electronic transition. A more detailed explanation of the above derivation of the Franck-Condon Principle can be found in Herzberg's Molecular Spectra and Molecular Structure.[9]

Franck and Condon were interested in the relative intensities of the vibrational spectral lines within the final electronic state. A vibrational branching ratio is calculated by taking the ratio of two vibrational cross sections from the same electronic state; generally, this ratio is that of an excited vibrational mode to the ground vibrational mode. Taking the ratio of two vibrational cross sections, as defined by Equation 1.11, it follows from basic algebra that the vibrational branching ratio is

$$\frac{\sigma_{\nu'+}}{\sigma_{\nu+}} = \frac{\left|\left\langle \chi^{'+} \middle| \chi_0 \right\rangle\right|^2}{\left|\left\langle {\chi_n}^{+} \middle| \chi_0 \right\rangle\right|^2} \qquad \text{(Equation 1.12)}$$

where the prime indicates an excited vibrational mode. The right-hand side of Equation 1.9 is known as the Franck-Condon Factor (FCF) for a particular pair of vibrational states. Since, the electronic component is the same for both vibrational states, the FCF is constant as a function of incident photon energy. Thus, Franck and Condon concluded that the relative population of vibrational states immediately after an electronic transition should be constant as functions of incident energy.[8] A diagram showing an example of a vertical transition between two bound electronic states, a simplified case, is shown in Figure 1.1, and a diagram showing a vertical transition between a bound state and a continuum state is shown in Figure 1.2.

While Figure 1.1 is the more simplified picture of the Franck-Condon principle, Figure 1.2 shows this same idea for the case of photoionization. In both Figures 1.1 and 1.2, the horizontal axes are internuclear distance, while the vertical axes are energy. Only when the differences in the kinetic energies of the ionic state vibrational modes are negligible does the Franck-Condon Principle also apply to bound state to continuum state transitions. The kinetic energy differences should be negligible starting from energies several eV above the ionization threshold to energies far above the ionization threshold, which is the case for all of the photoionization data presented in this dissertation. There are cases in which molecules have been shown to display non-Franck-Condon behavior; Section 1.6 will discuss these cases in further detail.

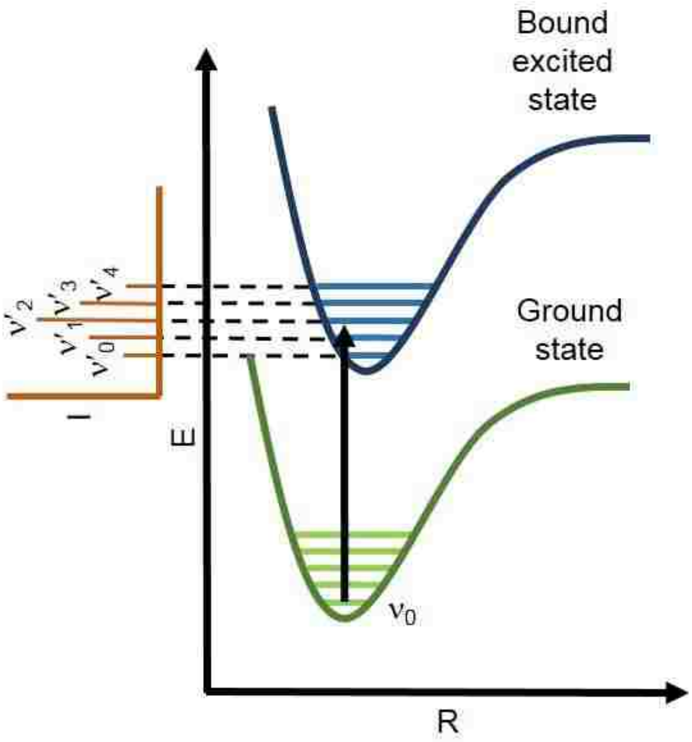

Figure 1.1. A vertical transition between a ground electronic state (green line) and a bound excited state (blue line) demonstrating the Franck-Condon Principle. The orange vibronic spectrum to the left illustrates the vibrational mode populations based on wavefunction overlap.

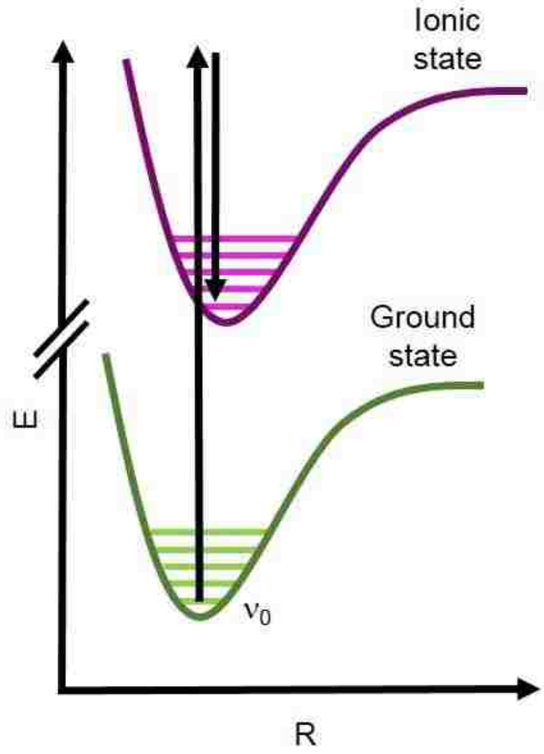

Figure 1.2. A vertical transition between a ground electronic state (green line) and an ionic state (purple line) demonstrating the Franck-Condon Principle.

1.4 FRANCK-CONDON BREAKDOWN

Several phenomena may lead to non-Franck-Condon behavior such as autoionization,[10] shape resonances,[11-23] Cooper minimum[24] and other interference effects,[25] interchannel coupling (coupling of two electronic states),[26-28] and intrachannel coupling.[29,30] Traditionally, instances of Franck-Condon breakdown which occur far above the ionization threshold have been far less studied.

Previously, non-Franck-Condon behavior occurring over wide energy ranges above the ionization threshold for several diatomic and triatomic molecules have been studied by the Poliakoff Research Group.[11,16-20,24,25,29-31] It has been found that shape resonances, in particular, often cause Franck-Condon breakdown over a range of several eV of photon energy. Section 1.4.1 will describe shape resonances in detail.

Interference effects are another common cause of breakdown of the Franck-Condon Principle in molecules. Two common types of interferences which may cause non-Franck-Condon behavior are Cooper mimina and Cohen-Fano interference. Cooper minima have been shown to cause non-Franck-Condon behavior over very broad photon energy ranges and often occur at energies far above the ionization threshold.[24] Cooper minima are further discussed in Section 1.4.2. Another type of interference which may affect the vibrational branching ratios is the interference described by Cohen and Fano.[25,32] Section 1.4.3 discussed Cohen-Fano interferences in further detail.

1.4.1 Shape Resonances

Shape resonances were first described by Joseph Dehmer in 1972,[33] and evidence of these resonant features was seen experimentally over the next two years.[34,35] Two dominant descriptions of shape resonances exist: one describes this phenomenon as an electron trapping mechanism caused by the potential energy surface;[36] the other describes these events based on unoccupied above ionization threshold molecular orbitals.[37] A simple schematic showing an electron transition involving a shape resonance is shown in Figure 1.3. Note the horizontal axis in Figure 1.3 is not internuclear distance, but merely the distance of an electron from some molecular origin.

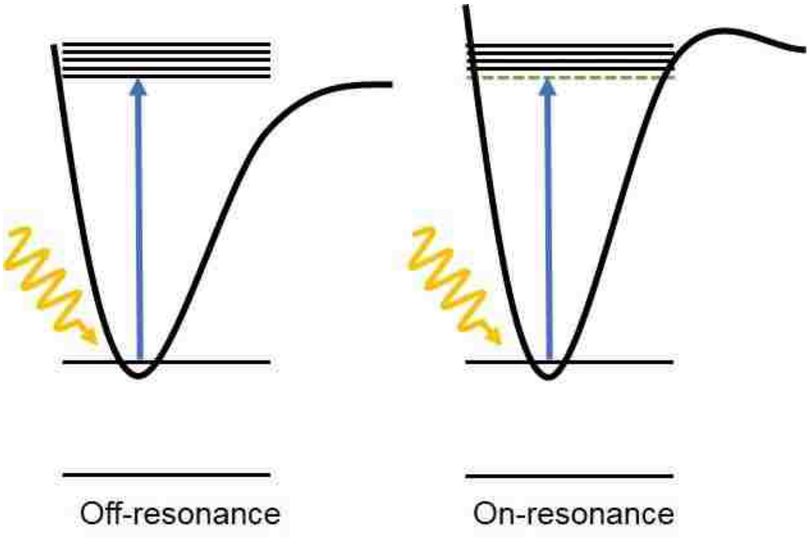

Figure 1.3. A schematic showing an electronic transition occurring off-resonance (left) and on-resonance (right) for a shape resonance. The potential energy curve is overlaid with the electron energy diagram to highlight the change in the barrier height at the energy of the shape resonance. The blue arrow represents the electron transition to the continuum. The green dashed line on the right represents the quasibound metastable state that the photoelectron is temporarily trapped in during a shape resonance.

Typically the strongest contribution to the potential that binds an electron to a system is the Coulombic force. The positively charged nucleus exerts an attractive force on the negatively charged electron. However, there is a weaker repulsive force which contributes to this potential called the centrifugal force, which comes from the angular momentum of an electron.[38] When a system is irradiated at the energy of a shape resonance, the strength of the centrifugal contribution to the potential experienced by the electron rapidly increases. This heightened strength of the potential effectively traps the electron in a quasibound, metastable continuum state. On resonance, the centrifugal potential fluctuates, eventually relaxing enough to allow the electron to tunnel through the barrier. This balance of the centrifugal and coulombic potentials is strongly tied to the symmetry of the system; thus, the resonance occurs only for particular channels in a system with specific angular momentum.[23]

The other method of describing shape resonances is by describing virtual valence molecular orbitals, which are energetically above the ionization threshold and thus overlapped with the continuum. Since these virtual orbitals are defined at a specific energy, that of the shape resonance, a transition between a lower bound state and the virtual state is possible at a specific energy. The concept of shape resonances simply being electronic transitions between a bound, occupied orbital and an above-ionization threshold unoccupied orbital has been described in detail by Langhoff.[37]

Shape resonances are important for many purposes. Since shape resonances are strongly linked to molecular geometry,[39] they are useful for determining structural details, such as bond lengths.[40] Sheehy, et al. established protocol for determining bond length from shape resonance information.[41]

It wasn’t until 1979 that Dehmer, et al. showed that shape resonances could cause a breakdown of the Franck-Condon Principle.[22,42,43] This Franck-Condon breakdown can be explained by the time which passes during the electron trapping. When the electron is finally released, or tunnels, from the quasibound state, the ionization has taken a much longer time than the process would have taken off-resonance. Due to the increased time the electron takes to exit the system, the nuclei have time to begin to move, meaning the timescales for the electronic transition and the nuclear transitions are similar for on resonance transitions. Since the electrons and the nuclei can move on relatively the same timescale at the energy of a shape resonance, there is a breakdown of the Franck-Condon approximation at shape resonances. Also, since shape resonances are localized within the molecule, they are also closely dependent on the molecular geometry, i.e., the internuclear separation. Thus, shape resonance can also cause vibrational mode specificity in the non-Franck-Condon behavior.

1.4.2 Cooper Minima

Cooper minima, first suggested in 1962, are the result of destructive interference between the bound electronic wavefunction and the continuum wavefunction, in other words, between the initial and final electronic wavefunctions during photoionization.[44] In order for this destructive interference to occur, as Cooper first noticed, the bound electronic wavefunction must contain a node. The presence of a node in the wavefunction means that it is possible the transition dipole moment matrix element will go through a change of sign as a function of photon energy. This interference pattern results in the partial photoionization cross section dropping to approximately zero for an atom and simply to a minimum for a molecule at a particular photon energy.

Cooper minima are generally localized on a single atom within a molecule and have significant atomic character. However, the Cooper minima are sensitive to the molecular environment, and thus constitute a decent probe into the nature of the molecular orbtials of the system.[45] These particular interference effects have also been associated with Franck-Condon breakdown. For instance, it was found that photoionizaton of N_2 ${}^2\sigma_u^{-1}$ displays Franck-Condon breakdown over an energy range of approximately 100 eV due to a Cooper minimum which has a strong dependence of internuclear separation.[24]

In 1993, the Cooper minimum, which arises from the Ar $^3\Pi$ state, was observed in a high-order harmonic spectrum generated from an Ar medium.[46] This was one of the first observations of the electron dynamics of the medium affecting the high-order harmonics spectrum.

1.4.3. Cohen-Fano Interference

In 1966, Howard Cohen and Ugo Fano described a Young’s type interference occurring as an outgoing photoelectron leaves a molecule.[32] Cohen and Fano described the multiple pathways of an outgoing photoelectron and the interference pattern that results from the various partial waves; this observation is similar to the various pathways of a photon through two slits in Youngs’s famous double-slit experiment. Cohen-Fano interference is a direct result of the interference of all the partial waves of various possible transitions from bound-states to continuum states. Since each partial wave declines with some oscillatory character, the sum of the partial waves, or the partial photoionization cross section, will show some interference fringes. It is clear that this effect is present in a homonuclear diatomic, since there are coherent orbitals from which the electron can be emitted. However, it was only relatively recently that this effect was realized in non-homonuclear molecules.[47] The evidence presented by Canton, et al. for Cohen-Fano interference in CO photoemission is explained by the large delocalized molecular orbitals spatially covering both atoms.

Franck-Condon breakdown due to Cohen-Fano Interference and Cooper mimina would be expected to appear very similar experimentally since these are both non-resonant effects. However, the differences between these two phenomena can be elucidated using calculated partial waves. Evidence of non-Franck-Condon behavior caused by a Cohen-Fano interference was also recently seen experimentally and explained with theory for photoionization leading to the N_2^+ $X^2\Sigma_g^+$ and CO^+ $X^2\Sigma^+$ states.[25]

1.5 STRONG FIELD IONIZATION

Photoionization can result from weak field or strong field techniques. Traditional photoelectron spectroscopy is carried out in the weak field regime, meaning the electric field of the incoming photon beam is too weak to significantly alter the electric field an electron experiences in a molecule. In strong field photoionization, the electric field an electron experiences in a molecule is distorted by the electric field of the ionizing radiation.

In weak field spectroscopy, the optical polarization has a linear response. On the contrary, in strong field spectroscopy the optical polarization has a non-linear response and depends not only on the linear term but also on higher-order terms.[48] Strong field ionization processes have non-linear responses due to the intensity of the light pulse; that is, there are many photons coming into the interaction region simultaneously. Strong field ionization techniques, and, consequently, non-linear spectroscopy techniques really expanded with the invention of the ultrafast laser. Further details on the history and concepts behind ultrafast lasers will be discussed in Section 1.6.1, and technical details about the ultrafast lasers used in the experiments discussed in this dissertation will be provided in Section 2.7.

Non-linear spectroscopy involves many light-matter interactions, as opposed to a single light-matter interaction in linear spectroscopy. Due to multiple light-matter interactions, non-linear spectroscopy can be useful for studying complex systems, such as molecules.

1.5.1 Keldysh Parameter

Leonid Keldysh derived a quantitative parameter to describe the field strength experienced by a bound electron as a method of predicting when tunneling ionization was probable over multiphoton ionization in the transparency region, $h\nu < I$.[49] The Keldysh parameter, γ, can be defined as

$$\gamma = \frac{\omega\sqrt{2m_e I_p}}{eF} \qquad \text{(Equation 1.13)}$$

where $\frac{\omega}{2\pi}$ is the frequency of the radiation, m_e is the mass of an electron, I_p is the ionization energy of the system, e is the charge of an electron and F is the electric field strength. Processes in which $\gamma \ll 1$ take place in the tunneling regime, while processes with $\gamma \gg 1$ are in the multiphoton regime. With the advent of ultrafast lasers, the focused intensity of the laser pulses is high enough so that tunneling is a dominant ionization process. The Keldysh parameter can also be described as the ratio between the frequency of the radiation, ω, and the frequency of an electron tunneling through a barrier, ω_t[50]

$$\gamma = \frac{\omega}{\omega_t} \qquad \text{(Equation 1.14)}$$

The tunneling regime was not easily studied before the advent of ultrafast lasers. Femtosecond pulse titanium sapphire lasers make it much easier to reach high peak intensities on the order of 10^{14} W/cm^2, since the entire beam is concentrated both spatially and temporally prior to focusing. Using these ultrafast lasers, it is also possible to create a short enough pulse that the atom or molecule does not have time to become ionized on the rising edge of the pulse; this pulse allows for the atom or molecule to experience the maximum intensity.[51]

1.5.2 The Evolution of Ultrafast Lasers

Laser technology has changed significantly over the past 20 years or so, making strong field experiments and time-resolved measurements feasible experimentally. The peak intensities have increased multiple orders of magnitude, the repetition rates have increased from shots per minute to thousands of shots per second, and the pulse durations have decreased from tens of picoseconds to less than ten femtoseconds.[52] With the evolution of ultrafast lasers, time-resolved measurements in the strong field regime have become possible. In particular, the current laser systems have opened the doors for studying HHG in the electron tunneling regime. However, these developments in laser technology are a huge contributing factor to the current popularity of strong field experiments, in general. Specific details about the ultrafast laser systems employed for the experiments discussed in this dissertation are reserved for Chapter 2, which discusses all the experimental details.

1.6 HIGH HARMONIC GENERATION AND THE THREE STEP MODEL

High-order harmonic generation (HHG) is a nonlinear process which produces attosecond pulses of UV and X-ray light. One of the potential applications of HHG is to provide a bright, tunable frequency, ultrafast tabletop source, making experiments which were traditionally confined to large synchrotron facilities feasible in a laboratory setting.[53-56] Another fundamentally interesting property of the high-order harmonics is that these harmonics are essentially the product of a self-probing experiment. The electron is first ionized and then forced to recombine with its parent ion. Therefore, the harmonics contain information not only about the laser pulse, but also time-resolved information about the electron-parent ion pair and their photorecombination dynamics.

In the early 1990s, Corkum[3] and Schafer, et al.[2] were the first scientists to provide theoretical explanations of the high-order harmonic generation process and suggest the photorecombination step. HHG is described most simply in three steps: tunnel ionization, free electron acceleration, and photorecombination.[57] The three step model for HHG is shown in Figure 1.4. First, the strong electric field distorts the potential energy well near a maximum intensity in the electric field, allowing the electron wave packet to tunnel out of the atom/molecule and into the laser field. For tunnel ionization to become a competitive process with multiphoton ionization, the field strength of the laser must be very high, on the order of 10^{14} W/cm^2.[51] It is important to note here that by tunnelling through the barrier, the electron enters the continuum with negligible kinetic energy. Since the electron has almost zero kinetic energy in the continuum, the laser field can sweep up the electron, accelerating and increasing the free electron’s kinetic energy. As the electric field of the laser changes direction, the electron is then accelerated back toward the atom/molecule. If the electron wave packet realigns with the parent ion, then recombination can occur. Upon recombining with the parent ion, all the excess energy the electron wave packet gains from being in the laser field is released in the form of a high-order harmonic of the fundamental wavelength.

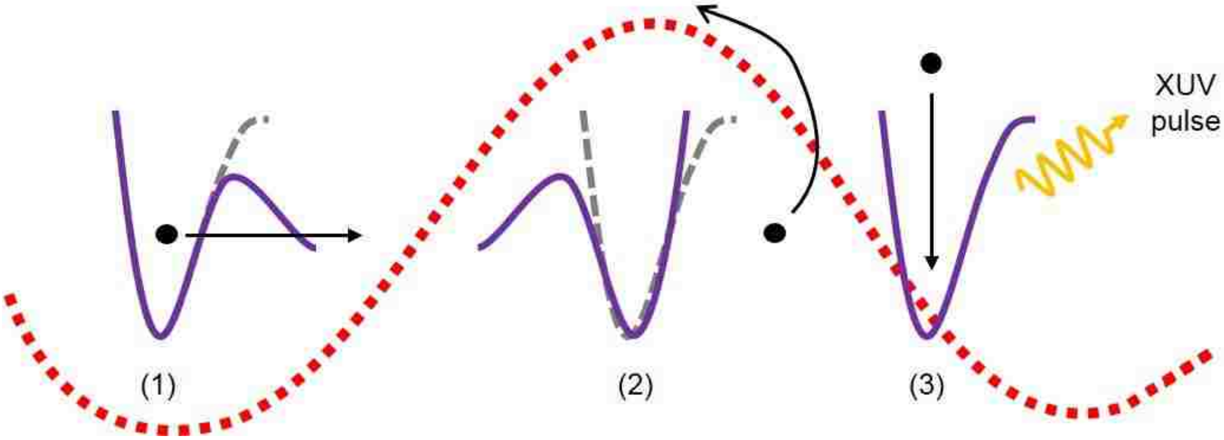

Figure 1.4. The three-step model to describe HHG: (1) is the tunnel ionization step, (2) shows the acceleration of the free electron, and (3) is the photorecombination step. The grey lines represent the unperturbed potential wells, and the blue lines represent the potential wells at particular points in the field of the laser. The red dashed line shows the oscillating electric field of the laser. The black circle represents the electron with the arrow pointing in the direction of electron motion.

Ionization always occurs near maximum intensity of the electric field, while photorecombination occurs at some intensity between opposing maximums. The timing of the electron between ionization and recombination relative to the wavelength of the electric field determines the order of the high harmonic. Two return times correspond to each harmonic order generated; these are referred to as the long and short trajectories. An electron along the long trajectory spends more time in the electric field of the laser than an electron along the short trajectory. As the energy of the harmonics increases, the times of an electron along either the long and short trajectory begin to converge. Thus, the cutoff harmonic, or the highest order harmonic generated, has only one corresponding electron trajectory.[58] In the early 1990’s, a paper by Krause, et al. concluded that the maximum harmonic seen, or the cut-off harmonic, can be described by the following law:[59]

$$E_{max} = I_p + 3.17U_p \qquad \text{(Equation 1.15)}$$

where I_p is the ionization potential of the atomic/molecular medium and U_p is the ponderamotive energy, which describes the energy of a free electron quivering within an electric field. The harmonic cutoff law, Equation 1.15, has been shown to match experimental results relatively well.[59]

The three-step model describes only the single atom-laser interaction. It is understood that the single atom-laser interaction is only part of the process. HHG requires not only an interaction with the laser pulse and a single atom but also propagation effects through the remainder of the medium. These macroscopic processes which contribute to HHG are described theoretically by Gaarde, et al.[60] Collectively the propagation effects lead to phase-matching, or phase-mismatching, between the fundamental driving laser and the many higher-order harmonic pulses. When the fundamental and high-order harmonic pulses are relatively in-phase with one another, the signal adds coherently, leading to a bright high-order harmonic spectrum. It has been found that the propagation effects, and thereby the degree of phase-matching in the generated harmonics, can be controlled by changing the focusing conditions within the medium gas jet[61], altering the density of the medium[61], or using a hollow-core fiber to guide the laser pulse[62]. For instance, it has been seen that with a gas jet or capillary, if the laser focus precedes the center of the gas, the harmonics are phase-matched off-axis and the long trajectories are most visible. However, when the laser focus follows the center of the gas, the harmonics are phase-matched on-axis, and the short trajectories are most visible.[63]

The experiments discussed in Chapter 7 involved using the polarization of the laser pulse as a probe for photorecombination dynamics. Since it is already known that the probability of the electron recombining with the parent ion is sensitive to the polarization, by adding small amounts of ellipticity to the laser pulse, we can systematically measure the decay of harmonic intensities as a function of polarization. It has been suggested that the harmonic intensity generated with an elliptical pulse normalized to the harmonic intensity generated with a linear pulse should decrease as a Gaussian function with increasing ellipticity according to the following model[64]

$$\frac{I_{XUV(\varepsilon)}}{i_{XUV(\varepsilon=0)}} \approx exp\left(-\frac{\beta^2\sqrt{2I_pI}}{4\pi^2c^2}\lambda^2\varepsilon^2\right) \qquad \text{(Equation 1.16)}$$

where I_{XUV} is the harmonic intensity, I_p is the ionization energy of the medium, I is the peak intensity of the laser, c is the speed of light, λ is the fundamental wavelength of the laser, ε is the ellipticity of the laser pulse, and β is a function of the time the electron spends in the electric field. The beta function can be defined as

$$\beta = \left(\frac{\sin\omega t_r - \sin\omega t_0}{\omega(t_r - t_0)} - \cos\omega t_0\right) \qquad \text{(Equation 1.17)}$$

where ω is the frequency of the laser pulse, t_0 is the birthing time of the electron into the electric field of the laser, and t_r is the time at which the electron recombines with the parent ion. This model has been shown to fit quite nicely to harmonics generated in Ne and He.[64] However, it should be noted that the energy regimes examined for both Ne and He do not display any known ionization dynamics. In Chapter 7, the way harmonic intensity decays as a function of ellipticity in a system with known ionization dynamics is explored.

The remainder of this dissertation explores both photoionization and photorecombination dynamics in various atomic and molecular systems. All experimental methods are discussed in detail in the Chapter 2. Chapter 3-6 discuss photoionization electron rescattering dynamics, which lead to non-Franck-Condon behavior in polyatomic and biologically relevant systems. Evidence for a method of probing photorecomination electron rescattering dynamics will is presented in Chapter 7.

1.7 REFERENCES

[1] A. Einstein, Ann. d. Physik 17 (1905) 132.

[2] K.J. Schafer, B. Yang, L.F. DiMauro, K.C. Kulander, Phys. Rev. Lett. 70 (1993) 1599.

[3] P.B. Corkum, Phys. Rev. Lett. 71 (1993) 1994.

[4] M. Born, R. Oppenheimer, Ann. Physik 84 (1927) 457.

[5] M. Born, W. Heinsenberg, Ann. d. Physik 74 (1924) 1.

[6] J.L. McHale, Molecular Spectroscopy, Pearson Education, Upper Saddle River, NJ, 1999.

[7] J. Franck, Trans. Faraday Soc. 21 (1926) 536.

[8] E. Condon, Phys. Rev. 28 (1926) 1182.

[9] G. Herzberg, Molecular Spectra and Molecular Structure, Robert E. Krieger Publishing Company, Malabar, Florida, 1950.

[10] J. Rius i Riu, A. Karawajczyk, M. Stankiewicz, K. Yoshiki Franzen, P. Winiarczyk, L. Veseth, Chem. Phys. Lett. 338 (2001) 285.

[11] R.R. Lucchese, R. Montuoro, K. Kotsis, M. Tashiro, M. Ehara, J.D. Bozek, A. Das, A. Landry, J. Rathbone, E.D. Poliakoff, Molecular Physics 108 (2010) 1055.

[12] R.R. Lucchese, J. Bozek, A. Das, E.D. Poliakoff, J. Chem. Phys. 131 (2009) 044311.

[13] R. Montuoro, R.R. Lucchese, J.D. Bozek, A. Das, E.D. Poliakoff, J. Chem. Phys. 126 (2007) 244309.

[14] A. Das, J.S. Miller, E.D. Poliakoff, R.R. Lucchese, J.D. Bozek, J. Chem. Phys. 127 (2007) 044312.

[15] A. Das, E.D. Poliakoff, R.R. Lucchese, J. Bozek, J. Chem. Phys. 125 (2006) 164316.

[16] G.J. Rathbone, E.D. Poliakoff, J. Bozek, D. Toffoli, R.R. Lucchese, J. Chem. Phys. 123 (2005) 014307.

[17] G.J. Rathbone, E.D. Poliakoff, J. Bozek, R.R. Lucchese, J. Chem. Phys. 122 (2005) 064308.

[18] G.J. Rathbone, E.D. Poliakoff, J. Bozek, R.R. Lucchese, Phys. Rev. Lett. 92 (2004) 143002.

[19] G.J. Rathbone, E.D. Poliakoff, J.D. Bozek, R.R. Lucchese, P. Lin, J. Chem. Phys. 120 (2004) 612.

[20] G.J. Rathbone, E.D. Poliakoff, J. Bozek, R.R. Lucchese, J. Chem. Phys. 114 (2001) 8240.

[21] P. Roy, I. Nenner, M.Y. Adam, J. Delwiche, M.J. Hubin Franskin, P. Lablanquie, D. Roy, Chem. Phys. Lett. 109 (1984) 607.

[22] J.L. Dehmer, D. Dill, S. Wallace, Phys. Rev. Lett. 43 (1979) 1005.

[23] M.N. Piancastelli, J. Electron. Spectrosc. Relat. Phenom. 100 (1999) 167.

[24] R.M. Rao, E.D. Poliakoff, K. Wang, V. McKoy, Phys. Rev. Lett. 76 (1996) 2666.

[25] J.A. Lopez-Dominguez, D. Hardy, A. Das, E.D. Poliakoff, A. Aguilar, R.R. Lucchese, J. Electron. Spectrosc. Relat. Phenom. 185 (2012) 211.

[26] W. Domcke, Phys. Scr. 19 (1979) 11.

[27] W. Domcke, L.S. Cederbaum, J. Schirmer, W. Von Niessen, C.E. Brion, K.H. Tan, Chem. Phys. 40 (1979) 171.

[28] P. Roy, R.J. Bartlett, W.J. Trela, T.A. Ferrett, A.C. Parr, S.H. Southworth, J.E. Hardis, V. Schmidt, J.L. Dehmer, J. Chem. Phys. 94 (1991) 949.

[29] J.S. Miller, E.D. Poliakoff, T.F. Miller, A.P.P. Natalense, R.R. Lucchese, J. Chem. Phys. 114 (2001) 4496.

[30] G.J. Rathbone, E.D. Poliakoff, J. Bozek, R.R. Lucchese, Can. J. Chem. 82 (2004) 1043.

[31] A. Das, E.D. Poliakoff, R.R. Lucchese, J.D. Bozek, J. Chem. Phys. 130 (2009) 044302.

[32] H.D. Cohen, U. Fano, Phys. Rev. 150 (1966) 30.

[33] J.L. Dehmer, J. Chem. Phys. 56 (1972) 4496.

[34] G.R. Wight, C.E. Brion, M.J. Van der Wiel, J. Electron. Spectrosc. Relat. Phenom. 1 (1973) 457.

[35] G.R. Wight, C.E. Brion, J. Electron. Spectrosc. Relat. Phenom. 4 (1974) 313.

[36] J.L. Dehmer, in: D.G. Truhlar (Ed.), Resonances in Electron-Molecule Scattering, van der Waals Complexes, and Reactive Chemical Dynamics, American Chemical Society, Washington, D.C., 1989, p. 139.

[37] P.W. Langhoff, in: D.G. Truhlar (Ed.), Resonances in Electron-Molecule Scattering, van der Waals Complexes, and Reactive Chemical Dynamics, American Chemical Society, Washington, D.C., 1984, p. 113.

[38] G.J. Schulz, Rev. Mod. Phys. 45 (1973) 378.

[39] L.A. Kelly, L.M. Duffy, B. Space, E.D. Poliakoff, P. Roy, S.H. Southworth, M.G. White, J. Chem. Phys. 90 (1989) 1544.

[40] M.N. Piancastelli, J. Electron. Spectrosc. Relat. Phenom. 100 (1999) 167.

[41] J.A. Sheeny, T.J. Gil, C.L. Winstead, R.E. Farren, P.W. Langhoff, J. Chem. Phys. 91 (1989) 1796.

[42] R. Stockbauer, B.E. Cole, D.L. Ederer, J.B. West, A.C. Parr, J.L. Dehmer, Phys. Rev. Lett. 43 (1979) 757.

[43] J.B. West, A.C. Parr, B.E. Cole, D.L. Ederer, R. Stockbauer, J.L. Dehmer, J. Phys. B.: At. Mol. Opt. Phys. 13 (1980) L105.

[44] J.W. Cooper, Phys. Rev. 123 (1962) 681.

[45] T.A. Carlson, M.O. Krause, W.A. Svensson, P. Gerard, F.A. Grimm, T.A. Whitley, B.P. Pullen, Z. Phys. D 2 (1986) 309.

[46] C.-G. Wahlstrom, J. Larrson, A. Persson, T. Starczewski, S. Svanberg, P. Salieres, P. Balcou, A. L'Huiller, Phys. Rev. A 48 (1993) 4709.

[47] S.E. Canton, E. Plesiat, J.D. Bozek, B.S. Rude, P. Decleva, F. Martin, Proc. Nat. Acad. Sci. USA 108 (2011) 7302.

[48] S. Mukamel, Principles of nonlinear optics, Oxford University Press, New York, 1995.

[49] L.V. Keldysh, Soviet Physics JETP 20 (1965) 1307.

[50] V.S. Popov, Physics - Uspekhi 47 (2004) 855.

[51] C. Cohen-Trannoudji, D. Guery-Odelin, Advances in Atomic Physics An Overview, World Scientific, New Jersey, 2011.

[52] M. Lewenstein, A. L'Huiller, in: T. Brabec (Ed.), Strong Field Laser Physics, Springer, New York, 2009, p. 147.

[53] M. Hentschel, R. Kienberger, C. Spielmann, G.A. Reider, N. Milosevic, T. Brabec, P.B. Corkum, U. Heinzman, M. Drescher, F. Krausz, Nature 414 (2001) 509.

[54] C. Spielmann, N.H. Burnett, S. Sartania, R. Koppitsch, M. Schnurer, C. Kan, M. Lenzner, P. Wobrauschek, F. Krausz, Science 278 (1997) 661.

[55] Z. Chang, A. Rundquist, H. Wang, M.M. Murnane, H.C. Kapteyn, Phys. Rev. Lett. 79 (1997) 2967.

[56] P.M. Paul, E.S. Toma, P. Breger, G. Mullot, F. Auge, P. Balcou, H.G. Muller, P. Agostini, Science 292 (2001) 1689.

[57] A.T. Le, R.R. Lucchese, S. Tonzani, T. Morishita, C.D. Lin, Phys. Rev. A 80 (2009) 013401.

[58] Y. Mairesse, A. de Bohan, L.J. Fransinski, H. Mergji, L.C. Dinu, P. Monochicourt, P. Breger, M. Kovacev, R. Traieb, B. Carre, H.G. Muller, P. Agostini, P. Salieres, Science 302 (2003) 1540.

[59] J.L. Krause, K.J. Schafer, K.C. Kulander, Phys. Rev. Lett. 68 (1992) 3535.

[60] M.B. Gaarde, J.L. Tate, K.J. Schafer, J. Phys. B.: At. Mol. Opt. Phys. 41 (2008) 132001.

[61] S. Kazamias, D. Douillet, F. Weihe, C. Valentin, A. Rousse, S. Sebban, G. Grillon, F. Auge, D. Hulin, P. Balcou, Phys. Rev. Lett. 90 (2003) 193901.

[62] A. Rundquist, C.G. Durfee, Z. Chang, C. Herne, S. Backus, M.M. Murnane, H.C. Kapteyn, Science 280 (1998) 1412.

[63] P. Salieres, I.P. Christov, in: T. Brabec (Ed.), Strong Field Laser Physics, Springer, New York, 2009, p. 261.

[64] M. Moller, Y. Cheng, S.D. Khan, B. Zhao, K. Zhao, M. Chini, G.G. Paulus, Z. Chang, Phys. Rev. A 86 (2012) 011401.

CHAPTER 2
EXPERIMENTAL METHODS

This chapter describes the experimental methods for both the photoelectron spectroscopy and the high-order harmonic generation (HHG) experiments. Sections 2.1-2.2 present the photoelectron spectroscopy experimental details, and in Section 2.3, the photoelectron spectra analysis procedures are described. In Sections 2.4 and 2.5 are the HHG experimental details. Section 2.6 discusses the data analysis procedure for the HHG spectra.

2.1 HIGH RESOLUTION PHOTOELECTRON SPECTROSCOPY EXPERIMENTAL SETUP

Photoelectron spectroscopy is a powerful tool for studying the electronic structure of atoms and molecules. This technique can be used to study either core or valence electronic structure, depending on the photon energy used. This type of spectroscopy can also be used to study surfaces of solids or gas phase samples. Photoelectron spectroscopy has many variations, such as magic-angle, angular-dependent, time-resolved (TRPES), near threshold, X-ray absorption near-edge structure (XANES), X-ray absorption fine structure (EXAFS), etc. For the work presented in Chapters 3-6, variable energy magic-angle photoelectron spectroscopy was used to study the energy dependence of vibrational branching ratios for several gas phase polyatomic systems, as well as the valence electronic structure of the pyrimidine-type nucleobases. The experimental setup for these studies is discussed below.

The spectrometer used for the photoelectron spectroscopy experiments presented here was a Scienta SES-200 from VG Scienta, the design of which has been thoroughly described elsewhere[1,2] and will be briefly reviewed below. Figure 2.1 shows a schematic of both the source chamber and the spectrometer. The angle between the polarization of the light source and the lens stack was kept at 54.73°, which is known as the magic angle. Collecting spectra at the magic angle allows for a simplified analysis of the energy dependence of Franck-Condon factors since, as was shown in Equation 1.12, the vibrational branching ratios are simply equal to the ratio of vibrational peak intensities. The analysis will be explained in more detail in Section 2.3.

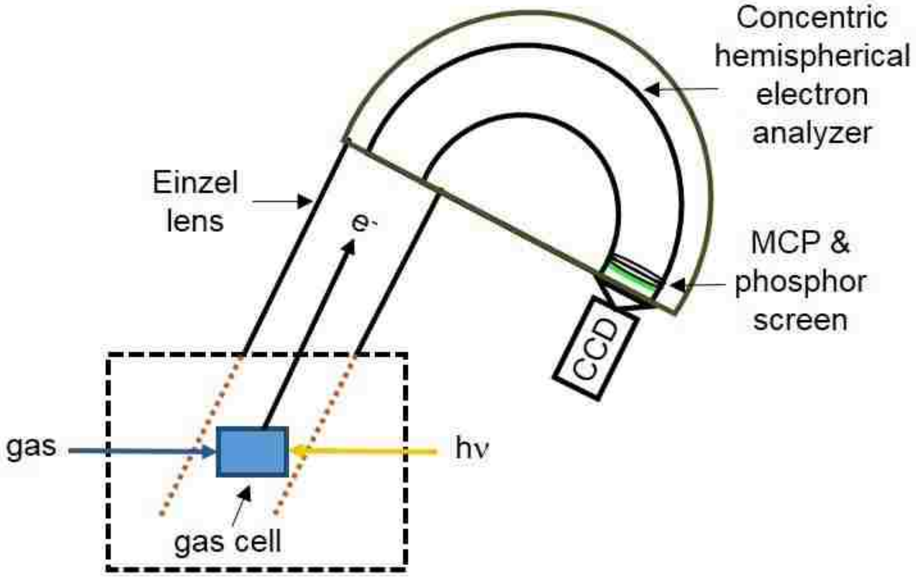

Figure 2.1. A schematic showing the chamber (shown in a black dashed line) and spectrometer for the photoelectron studies described here. The photon beam and gas phase sample interacted in a differentially pumped gas cell with a slit pointing into an einzel lens stack. The photoelectrons passed through a concentric hemispherical electron energy analyzer to a microchannel plate and phosphor screen detector. The image on the phosphor screen was then captured by a CCD camera.

The interaction region can be either a molecular jet or a gas cell within the vacuum chamber. The spectrometer was operated at a chamber pressure on the order of 10^{-6} torr. For the experiments described in this dissertation, a differentially pumped gas cell was used for the interaction region. The gas cell had a pressure of on the order of 10 mtorr. The sample gas flowed from a gas cylinder or sample holder outside of the vacuum chamber through a flange and directly into the gas cell. The gas cell was coated in colloidal graphite to prevent sample build-up and consequent charging of the gas cell.

For solid samples, a removable aluminum block oven was placed in the gas transfer line between the flange and the gas cell. A cartridge heater was located at the bottom of the block oven. When solid samples were sublimated in the block oven, the transfer line from the oven to the gas cell was heated with heat tape. During heated experiments, thermocouple readings were taken on the side of the block oven above the level where the cartridge heater sat and on the transfer line before the Mu-metal shielding which surrounds the gas cell. A schematic of the chamber setup is shown in Figure 2.2. For gas phase samples, and for high vapor pressure liquid samples, the block oven was removed and replaced with a longer transfer line.

The gas cell was contained within Mu-metal shielding. Mu-metal is a nickel-iron-molybdenum alloy which upon annealing becomes highly effective in shielding magnetic fields from both ac and dc sources.[3] The mu-metal shielding around the gas cell in the vacuum chamber absorbed stray magnetic fields, and thus prevented these fields from interfering with the pathways of the photoelectrons. The photon beam was aligned through two small holes on either end of the gas cell. Once the molecules were ionized in the gas cell, the electrons exited through the slit in the top of the gas cell. The slit in the gas cell pointed directly toward the lens stack leading to the analyzer. Since the data discussed in the following chapters was collected at the magic angle, the angle between the polarization of the photon beam and the lens stack was kept at 54.73°.

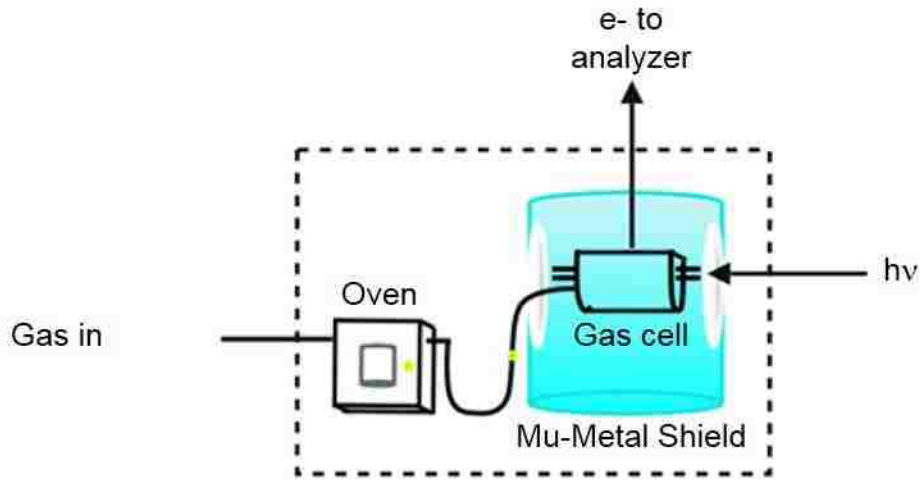

Figure 2.2. A schematic showing the inside of the photoelectron spectroscopy experimental chamber. The gas (or carrier gas for a solid sample) flowed in from an external gas manifold. The aluminum block oven, which is removable, was heated by a cartridge heater at the bottom of the oven in order to sublimate the solid sample sitting in the inner reservoir. The yellow markers indicate approximately where thermocouple readings were taken for heated experiments. The gas cell sat inside Mu-Metal shielding. The photon beam entered through the tubing on the side of the gas cell. Emitted electrons exited through a slit in the top of the gas cell toward the analyzer.

The lens stack was an einzel lens, meaning that the electrons were either accelerated or retarded so that only a certain initial electron kinetic energy was brought to the pass energy of the analyzer. A diagram of the einzel lens is shown in Figure 2.3. The lens stack was comprised of four cylindrical lens. The first voltage, V1, guided the electrons from the slit in the gas cell into the lens stack. The voltages applied to the second, V2, and last, V4, lenses were kept at equivalent and constant values, while the voltage applied to the middle lens, V3, was scanned in order to relate specific initial electron kinetic energies to the pass energy of the analyzer.[1,4]

By scanning the voltage on the V3, photoelectrons of differing initial kinetic energies were allowed to pass through the analyzer. The longest lens in the stack is V3. A fixed slit, S2, sat in V3 and was followed by a semi-cylindrical deflector, which corrected the focusing of the electrons passing though the einzel lens.

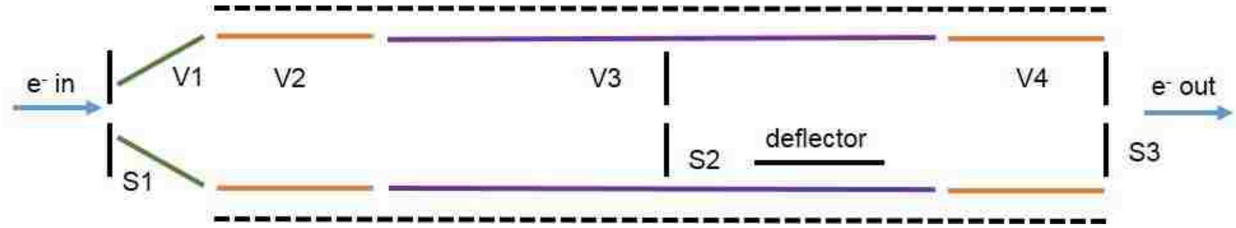

Figure 2.3. A schematic of the einzel lens stack is shown. All voltages in the einzel lens were cylindrical. Voltages 2 (V2) and 4 (V4) are shown in orange and were set to the same value, while voltage 3 (V3), shown in purple, was scanned. Slit 1, S1, was on the gas cell. Slit 2, S2, sat in V2 and was followed by a semi-cylindrical deflector. Slit 3, S3, was a variable slit, and it sat after V3, at the entrance to the analyzer.

An exchangeable slit, S3, sat after the exit of the last lens in the lens stack but prior to the entrance of the analyzer. Multiple slits with widths varying between 0.100 and 0.700 mm, whose shapes were either flat or curved, were lined up on a sliding track. The track could be moved electronically to position any of these slits into the position of S3.

The analyzer used in this setup was a concentric hemispherical electron analyzer. This style of analyzer consisted of two concentric hemispherical plates with a mean radius of 144 mm. The voltages on the inner and outer hemispheres were set such that

$$E_p = -\frac{e}{2r}(V_i r_i + V_o r_o) \qquad \text{(Equation 2.1)}$$

where E_p is the pass energy of the analyzer, V_i is the voltage applied to the inner hemisphere, V_o is the voltage applied to the outer hemisphere, r_i is the radius of the inner hemisphere, r_o is the radius of the outer hemisphere and r is the radius of the trajectory of a photoelectron with energy equal to E_p. The analyzer had a set pass energy, which is the electron kinetic energy which will pass between the two hemispherical plates and reach the detector instead of crashing into the walls. The pass energy was set for the acquisition of a single spectrum, and the einzel lens was changed systematically to bring each different initial electron kinetic energy to the pass energy individually. Thus, the electron kinetic energies were scanned to collect the spectrum.

The detector used in this setup consisted of two microchannel plates, MCPs, with a phosphor screen behind them and a charge-coupled device, CCD, camera. An MCP is an array of tiny electron multiplying channels.[5] The electrons cascaded through the MCPs and then illuminated the phosphor screen. The illuminated image on the phosphor screen was then collected with the CCD camera. Microchannel plate detectors allow for a two-dimensional position and momentum sensitive electron measurement.

2.2 SYNCHROTRON RADIATION

The photon beam used to ionize the samples discussed in Chapters 3-6 of this dissertation was a synchrotron beam. Synchrotron radiation is the radiation emitted by an accelerated electron moving along a bent or curved path.[6] Synchrotron beamlines are useful to many experiments because they are variable photon energy sources, which produce bright light from the infrared through the hard X-ray region depending on the beamline specifications. Using synchrotron radiation as the light source for these photoelectron spectroscopy experiments allowed for the study of the energy dependence of the photoelectron spectrum.

The synchrotron source used for the experiments described here was a third generation synchrotron facility, which is the highest generation synchrotron source to date. The main difference between different generations of synchrotron facilities is the incorporation of insertion devices. All synchrotron facilities include a short linear electron accelerator, which accelerates electron bunches; the electron bunches are then injected into a storage ring, which consists of straight sections separated by bending magnets. Synchrotron radiation is emitted at each bending magnet as the pathway of the accelerated electron bunch is curved. Second generation synchrotron sources were the first to incorporate insertion devices in the straight sections. The first insertion devices were wigglers. Third generation synchrotron sources also incorporated undulators in select straight sections. Wigglers and undulators will be described in further detail in Section 2.2.1.

2.2.1 Insertion Devices

The spectrum and brightness of the synchrotron radiation released depends on the energy of the electron bunch as well as the properties of either the bending magnet or insertion device at the port to a given beamline. There are two common types of insertion devices: wigglers and undulators. Both wigglers and undulators consist of a periodic array of magnets which rapidly oscillate, or “wiggle,” the electron bunch trajectory. As the pathway of the electron bunch oscillates, synchrotron radiation is released, much like from a bending magnet. Using insertion devices increases the flux, and, consequently, brilliance of the synchrotron radiation released to the beamline. Insertion devices can also change the photon energy spectrum available to the beamline.[6] A diagram of a basic wiggler is shown in Figure 2.4.

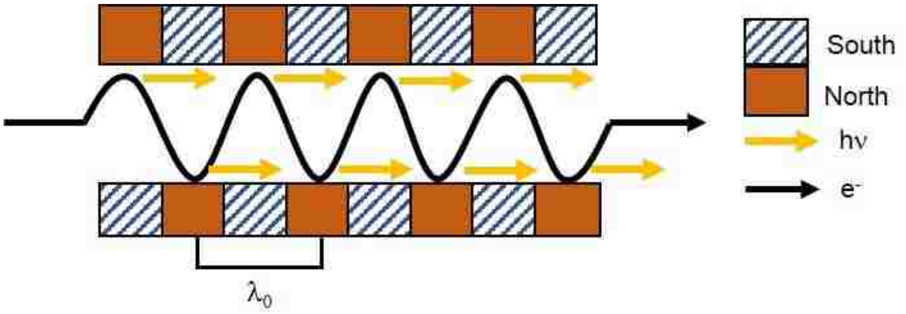

Figure 2.4. A schematic of a basic synchrotron insertion device. The electron bunch trajectory (represented by the black line) is wiggled by the periodic magnet array, releasing high energy photons (represented by the yellow arrows) in the direction of electron propagation at each turning point. The period of the wiggler/undulator is represented by λ_0.

The key difference between wigglers and undulators is the spectrum of synchrotron radiation delivered to the beamline. A wiggler produces a similar range of photon energies to the simple bending magnet but with increased brightness; however, an undulator produces very bright radiation over a much narrower energy spectrum.[6] The parameter which defines the difference between wigglers and undulators is the K-parameter, which corresponds to divergence of the beam caused by the insertion device relative to the divergence of the beam caused by synchrotron radiation emission. The K-parameter can be defined by the following equation,

$$K = \frac{eB_0\lambda_0}{2\pi m_0 c} \qquad \text{(Equation 2.2)}$$

where e is the charge of an electron, B_0 is the amplitude of the magnetic component of the field, λ_0 is the period of the magnet array, m_0 is the resting mass of an electron, and c is the speed of light.[6] Then the light emitted from the electron bunch passing through the insertion device can be defined by

$$\nu_n = n\left(\frac{2c\gamma^2}{\lambda_0}\right)\left(1 + \frac{K^2}{2} + \gamma^2\theta^2\right)^{-1}, n = 1, 2, 3, \ldots \quad \text{(Equation 2.3)}$$

where n defines the harmonic order, $\frac{1}{\gamma}$ is the divergence of a one-electron synchrotron radiation emission process, and θ is the angle of photon emission. So, for an undulator, either $K \ll 1$, or $K > 1$ and the number of periods in the magnet array is large, forcing $\theta \approx 0$.[6]

2.2.2 Advanced Light Source Beamline 10.0.1

The high-resolution photoelectron spectrometer was setup at beamline 10.0.1 at the Advanced Light Source in Berkeley, California. The setup of beamline 10.0.1 has been previously described in detail.[7] The light at beamline 10.0.1 comes from an undulator (U10) and includes photons over the energy range of 17 to 340 eV. U10 is a 43 period undulator with each period being 10 cm long. The photon beam was a horizontal linearly polarized beam. The photons from the undulator went through a spherical grating monochromator with three interchangeable gratings. For the data discussed here, only the 380 and 925 lines/mm gratings were used since the data discussed in this dissertation was collected over the energy range
$17 \leq h\nu \leq 150$ eV.

High-resolution photoelectron spectroscopy requires narrow bandwidth radiation over a broad spectral range, which corresponds to the level of brightness obtainable at undulator beamlines in third generation synchrotron sources.[7] Being an undulator beamline, beamline 10.0.1 has high photon flux of approximately
10^{13} photons/s/0.1% beamwidth at 30 eV. High flux was necessary to obtain usable

vibrationally resolved photoelectron spectra. The spot size of the beamline at the interaction region was < 600 μm.

2.3 PHOTOIONIZATION DATA ANALYSIS

According to the Franck-Condon approximation[8,9], the vibrational state population distribution during an electron transition should be photon energy independent, as was discussed in Chapter 1. Using linearly polarized light, the angular dependence of the vibrational peak intensity is[10]

$$I(\theta) = \frac{d\sigma_v}{d\Omega} = \frac{\sigma_v}{4\pi}\left[1 - \frac{\beta}{4}(3cos^2\theta - 1)\right] \qquad \text{(Equation 2.4)}$$

where σ_v is the vibrational partial photoionization cross section, β is the asymmetry parameter, and θ is the angle between the polarization of the radiation and the lens stack. The asymmetry parameter can vary between -1 and +2 and describes the direction of emission of the photoelectrons during photoionization. When $\beta = 0$, the photoelectrons show no angular dependence and are emitted isotropically. $\beta = -1$ corresponds to the photoelectrons being ejected on axis with the photon beam. Photoelectrons emitted from s-orbitals typically have $\beta = +2$, which corresponds to the photoelectrons being ejected at a right angle to the direction of photon propagation.[10] Since all the photoelectron spectra discussed here were collected at the magic angle, $\theta = 54.73°$, the angular dependent term, $3cos^2\theta$, becomes 0. Thus, the intensity of a vibrational peak becomes

$$I(\theta) = \frac{\sigma_v}{4\pi} \qquad \text{(Equation 2.5)}$$

From Equation 2.5, it follows that the vibrational branching ratio, the ratio of two vibrational cross sections from the same electronic state, becomes

$$\frac{\sigma_{\nu''}}{\sigma_{\nu'}} = \frac{I_{\nu''}}{I_{\nu'}} \qquad \text{(Equation 2.6)}$$

Thus, for spectra measured at the magic angle, the vibrational branching ratios are approximately equal to the ratio of vibrational peak intensities. Comparing Equation 2.6 with Equation 1.12, it becomes apparent that the ratio of vibrational peak intensities in magic-angle photoelectron spectra is approximately equal the Franck-Condon factor for a set of vibrational modes.

Vibrational peaks in each photoelectron spectra were fit using Igor Pro (WaveMetrics, Oswago, OR, USA), a graphing and data analysis software. The energy scale spacings between the vibrational peaks were loosely based on published infrared studies of the neutral molecules. This approximation is generally valid for at least the ground ionic state. Once a fit was established for the spectrum of a particular state, the same peak spacings were applied to all spectra of that state at various energies, allowing only the peak intensities and fwhm’s to float. The vibrational branching ratios were then calculated from the fit peak intensities. In this work, vibrational branching ratios were always calculated as the photoionization cross section of the vibrational peak of interest divided by the photoionization cross section of the ν=0 peak. These vibrational branching ratios were then plotted as a function of photon energy. Under Franck-Condon conditions, the vibrational branching ratios as a function of energy should be constant. Analyzing the energy ranges where the vibrational branching ratios were not constant gives information about the electronic and nuclear dynamics of the system. A schematic showing the analysis steps for the photoelectron spectroscopy data is shown in Figure 2.5.

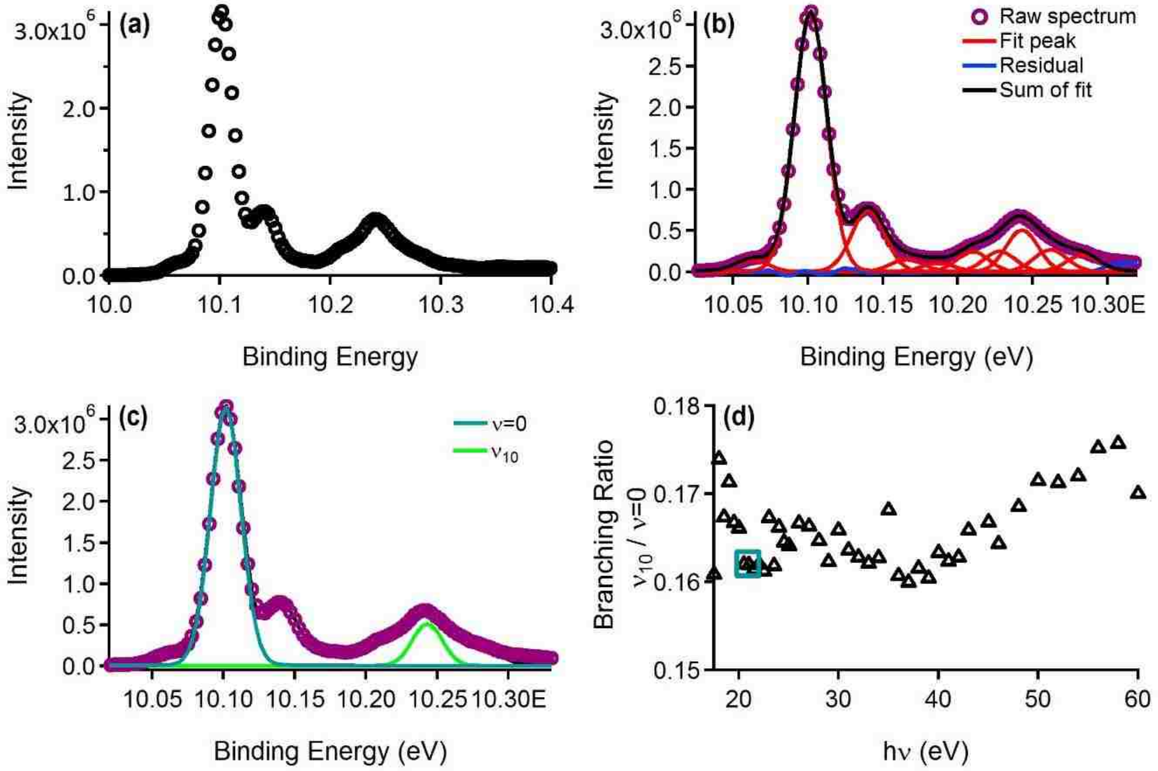

Figure 2.5. A schematic describing the analysis of the photoelectron spectroscopy data. (a) First, the raw photoelectron spectrum (black open circles) was converted from a kinetic energy scale to a binding energy scale. (b) Then, the unique fit was applied to the spectrum and allowed to optimize. In this figure, the purple open circles are the raw data; the red solid lines are the individual fit peaks; the blue solid line is the residual from the fit; and the black solid line is the sum of all the fit peaks. (c) Branching ratios were calculated by dividing the peak intensity of a specific vibrational peak by the intensity of the ground vibrational mode. Shown here are the two peaks used to calculate the vibrational branching ratio for $\nu_{10}/\nu = 0$. (d) A particular vibrational branching ratio was plotted as a function of photon energy. The ratio calculated in (c) became the data point in the blue square shown in (d).

2.4 BASIC HIGH-ORDER HARMONIC GENERATION EXPERIMENTAL SETUP

The HHG setup can easily be divided into two sections, the source chamber and the spectrometer. A schematic of the entire HHG setup is shown in Figure 2.6.

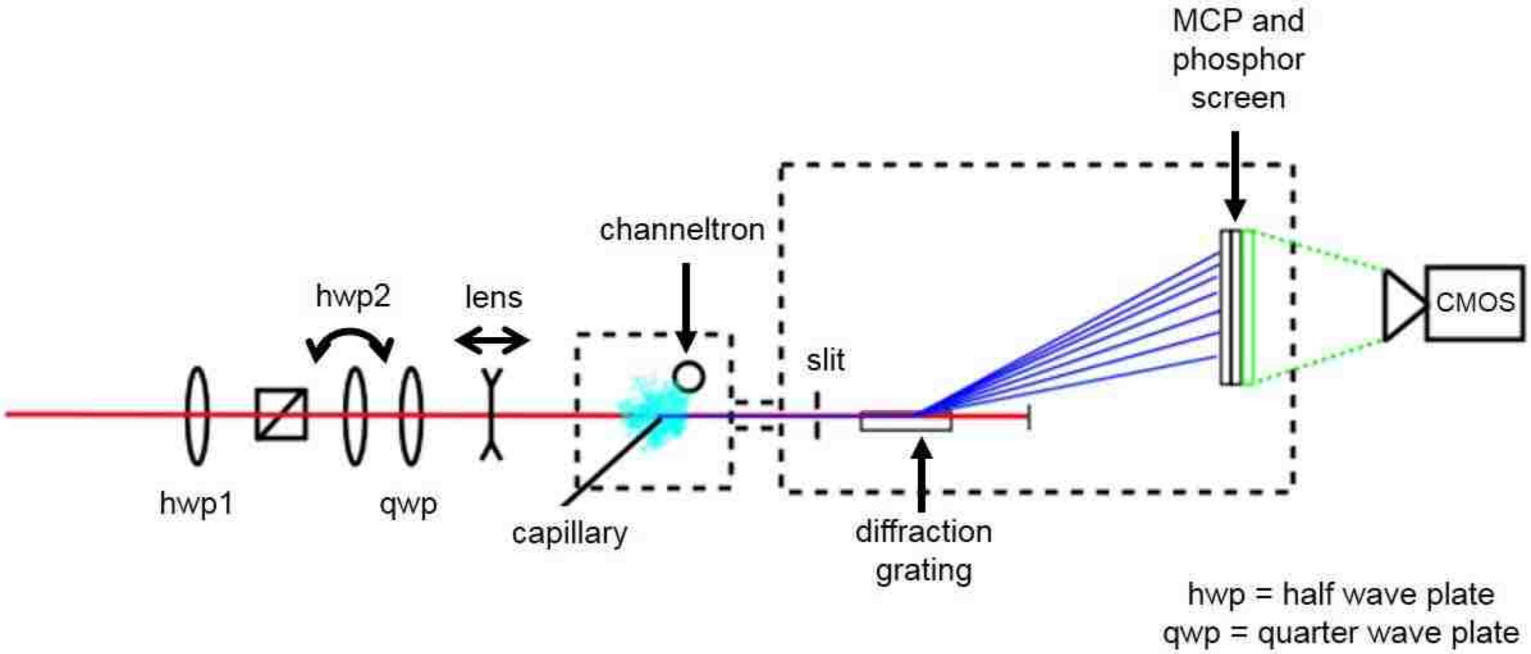

Figure 2.6. A schematic of the HHG setup. The first half-wave plate, hwp1, was used to control the laser intensity. The combination of the second half-wave plate, hwp2, and the quarter wave-plate, qwp, was used to control the polarization of the laser. Hwp2, was on an automated rotational stage, while qwp was held at a fixed value to allow linear light to pass through unaffected. The focusing lens was on an automated translational stage

High harmonics of the fundamental frequency of the laser were created in the source chamber. The source chamber had an operational pressure on the order of 10^{-5} torr. The laser was focused either within a supersonic gas jet created either by an Amsterdam Cantilever Piezo Valve[11] or an Even Lavie Valve[12,13] or within an effusive gas jet from the end of a capillary. Both valves were operated in pulsed mode with parameters optimized for each sample. The piezo pulsed valve created a relatively wide gas jet, while the jet from the Even Lavie valve was narrow.

The individual harmonics and the fundamental laser pulse must be relatively phase-matched in order to produce intense high harmonic signal. Phase matching in this instance refers to matching of the phases between the generated harmonics and the phase of the laser.[14] One way to alter the phase matching conditions is to move the focus of the laser translationally through the gas jet. It has been shown previously that the harmonics are best phase-matched when the laser focus is 1-3 mm before the center of the gas jet.[14-16] In this setup, the focusing lens was mounted on an automated translational stage, so that phase matching conditions could be scanned.

Within the source chamber, the ionization which did not lead to photorecombination was also measured using either a charged mesh or a channeltron sitting below and to the side of the interaction region. The relative position of the laser focus within the gas jet was easily observed by measuring the ion signal. When the laser focus was in the center, and most dense region, of the gas jet, a maximum amount of ionization occurred since the densest region of the gas jet was experiencing the peak intensity of the focused laser pulse.

Past the interaction region, the fundamental and various harmonic pulses passed through a differential pumping tube and slit. After the slit, a 1200 lines/mm spherical holographic (Shimadzu 30-002) diffraction grating separated off the fundamental beam and each of the high harmonic beams. The fundamental beam hit a baffle, and the separated high harmonics were projected onto a pair of z-stacked microchannel plates with a phosphor screen behind. A Hamamatsu ORCA-Flash 2.8 complimentary metal-oxide semiconductor (CMOS) camera collected the image illuminated on the phosphor screen. As was stated in Section 2.1, MCPs offer the unique advantage of being sensitive to the momentum and the position of the photons or electrons being detected. In the HHG experiments, this ability was incredibly important as it allowed for the simultaneous measurement of all of the different generated harmonics.

2.5 ULTRAFAST LASERS

As mentioned in Chapter 1, the development of ultrafast lasers aided significantly in the ability to study HHG. The development of the solid state Ti:sapphire laser centered at 800 nm was important in that it provided a relatively broadband laser source, ~ 200 nm.[17] Solid state laser media generally have a higher energy density than gas or liquid state laser media. For instance, Ti:sapphire has an average energy density of approximately 1 J/cm^2.[17] Combining solid state media lasers with chirped pulse amplifiers led to a large jump in laser intensity.

Chirped pulse amplification (CPA) is one method for significantly increasing the intensity of the laser pulse. In the CPA method, the pulse is first chirped so that the red components move to the front of the pulse, and the blue components follow. As the pulse is chirped, it is also stretched, temporally increasing the pulse duration by three to four orders of magnitude. Then, the separated components in the chirped, stretched pulse are amplified. After amplification, the pulse is compressed and simultaneously chirped in the opposite direction from the initial chirp, essentially correcting for the initial chirp. The resulting CPA pulse is on the order of 10^{11} times more intense than the original pulse.[18] The CPA method is ideal for amplifying few cycle pulses without the risk of damaging the actual amplification optics or incurring non-linear effects. CPA is the main amplification technique utilized in ultrafast lasers today.[17]

2.5.1 Kansas Light Source

The Kansas Light Source (KLS) is a homebuilt CPA Ti:sapphire laser which is centered at 790 nm with an fwhm of approximately 70 nm. The KLS is operated at a repetition rate of 2 kHz. For the experiments described in this dissertation, the KLS was operated with a pulse duration of 25 – 30 fs and a corresponding maximum pulse energy of 4 mJ. KLS is part of the James R. MacDonald Laboratory (JRM) at Kansas State University.

2.5.2 HITS (High Intensity Tunable Source)

The high intensity tunable source, HITS laser, is the KM Labs Red Dragon commercial Ti:sapphire laser system. The HITS system, which consists of three pump lasers, has a final output of approximately 18 mJ/pulse at a 1 kHz repetition rate with a pulse duration of ≤ 25 fs. The fundamental frequency of the HITS is centered at 805 nm, with an fwhm of ~74 nm.

This laser can be operated with or without a tunable optical parametric amplifier, TOPAS. The wavelength can be varied between 1000 and 2000 nm using the TOPAS. Optical parametric amplifiers (OPA) create new, longer wavelengths by mixing multiple wavelength beams together. The TOPAS system mixes ω, 2ω, and white light specifically, where $\omega = 800\ nm$ from the Ti:sapphire system.

2.6 HIGH-ORDER HARMONICS DATA ANALYSIS

The HHG data discussed here was also analyzed using WaveMetrics IgorPro software. The raw high harmonics images collected at the camera were first background subtracted and cropped as necessary to correct for any back reflections from the edge of the detector. The background subtracted images were summed vertically to create two-dimensional harmonic lineouts. Knowing the initial harmonic from calibrating the grating and detector, it was easy to label the harmonics in the lineout graph and identify the cut-off harmonic. The maximums of each harmonic peak were then selected to create a spectral envelope. It was visually easier to compare the spectral envelope of the harmonics with partial photoionization cross sections as functions of energy. For phase matching data, spectral envelopes were created for all different phase matching conditions and compared with the partial photoionization cross sections of the atom or molecule.

For data collected using elliptically polarized light, the spectral envelope was compared at one phase matching condition for many different ellipticity values. The harmonic intensities from elliptically polarized light were normalized to the harmonic intensities from linearly polarized light. This normalization allowed for easy comparison of the way in which the change in the polarization of the laser affected each individual harmonic. The normalized harmonic intensities as a function of ellipticity were also fitted to the Gaussian function to determine β, the parameter which describes the time the electron spends in the electric field of the laser using Equation 1.15, which was suggested by Moller, et al.[19]

Chapters 3 – 5 discuss the analyzed photoionization data. The HHG data is further discussed in Chapters 6 and 7.

2.7 REFERENCES

[1] P. Baltzer, B. Wannberg, M. Carlson Gothe, Rev. Sci. Instrum. 62 (1991) 643.

[2] P. Baltzer, L. Karlsson, M. Lundqvist, B. Wannberg, Rev. Sci. Instrum. 64 (1993) 2179.

[3] Mu Metal Specifications. The MuShield Company, Londonderry, NH, 2009.

[4] J.H. Moore, C.C. Davis, M.A. Coplan, Building Scientific Apparatus, Perseus Books, Cambridge, 1991.

[5] J.L. Wiza, Nuc. Instr. Meth. 162 (1979) 587.

[6] G. Margaritondo, Introduction to Synchrotron Radiation, Oxford University Press, Inc., New York, NY, 1988.

[7] G. Ohrwall, J. Bozek, P. Baltzer, J. Electron. Spectrosc. Relat. Phenom. 104 (1999) 209.

[8] J. Franck, Trans. Faraday Soc. 21 (1926) 536.

[9] E. Condon, Phys. Rev. 28 (1926) 1182.

[10] P.K. Ghosh, Introduction to Photoelectron Spectroscopy, John Wiley & Sons, New York, 1983.

[11] D. Irimia, D. Dobrikov, R. Kortekaas, H. Voet, D.A. van den Ende, W.A. Goren, M.H.M. Janssen, Rev. Sci. Instrum. 80 (2009) 113303.

[12] M. Hillenkamp, S. Keinan, U. Even, J. Chem. Phys. 118 (2003) 8699.

[13] U. Even, J. Jortner, D. Noy, N. Lavie, C. Cossart-Magos, J. Chem. Phys. 112 (2000) 8068.

[14] M.B. Gaarde, J.L. Tate, K.J. Schafer, J. Phys. B.: At. Mol. Opt. Phys. 41 (2008) 132001.

[15] S. Kazamias, D. Douillet, F. Weihe, C. Valentin, A. Rousse, S. Sebban, G. Grillon, F. Auge, D. Hulin, P. Balcou, Phys. Rev. Lett. 90 (2003) 193901.

[16] J.P. Farrell, L.S. Spector, B.K. McFarland, P.H. Bucksbaum, M. Guhr, M.B. Gaarde, K.J. Schafer, Phys. Rev. A 83 (2011) 023420.

[17] G. Cheriaux, in: T. Brabec (Ed.), Strong Field Laser Physics, Springer, New York, 2009, p. 17.

[18] C. Cohen-Trannoudji, D. Guery-Odelin, Advances in Atomic Physics An Overview, World Scientific, New Jersey, 2011.

[19] M. Moller, Y. Cheng, S.D. Khan, B. Zhao, K. Zhao, M. Chini, G.G. Paulus, Z. Chang, Phys. Rev. A 86 (2012) 011401.

CHAPTER 3

MODE-SPECIFIC NON-FRANCK-CONDON BEHAVIOR IN PHOTOIONIZATION RESULTING IN THE ACROLEIN $\tilde{X}\ ^2A'$ IONIC STATE DUE TO SHAPE RESONANCES

This chapter describes the energy dependent photoelectron spectroscopy studies of ionization leading to the $\tilde{X}\ ^2A'$ ionic state of acrolein. Magic-angle photoelectron spectroscopy, as described in Chapter 2, was performed at beamline 10.0.1 of the Advanced Light Source. Franck-Condon breakdown was observed in the vibrational branching ratios due to shape resonances. Both the experimental and theoretical results, which are presented in this chapter, were published in the Journal of Chemical Physics in 2014.[1]

3.1 ACROLEIN

Vibrational branching ratios obtained with high-resolution photoelectron spectroscopy have been used to show evidence of various electron rescattering dynamics in the photoionization of many diatomic and triatomic systems.[2-11] The previous molecules studied were relatively symmetric, in comparison to acrolein, which is of low symmetry, belonging to the C_s point group. With increasing molecular size and complexity, the electron rescattering dynamics are expected to become more complex and interesting, but also more challenging to detect with the increase in vibrational modes. In particular, shape resonances in complex molecules lead to many interesting correlations between electronic and nuclear degrees of freedom, since the shape resonance temporarily traps the outgoing photoelectron, allowing time for the nuclei to move and adjust.[12-18] Also, since shape resonances have a spatial component, much like molecular orbitals, it is interesting to study which vibrational motions are most affected by the shape resonant electron trapping. By investigating vibrational mode specificity in non-Franck-Condon behavior due to shape resonances, information about the spatial component of the resonant feature can be obtained. Furthermore, electron rescattering dynamics are of particular interest in the field of chemistry as they affect bond formation and bond breaking in chemical reactions. However, few studies have used vibrational branching ratios from valence shell photoelectron spectroscopy to further understand electron rescattering dynamics in large polyatomic systems.

Acrolein, also known as propenal, is a simple unsaturated aldehyde. The molecular structure of acrolein is shown in Figure 3.1. Acrolein can be thought of as a small fragment of many biologically relevant molecules, such as various amino acids, since it contains an aldehyde group. The two stable forms of acrolein are s-trans and s-cis. However, since the experiments discussed here were performed at room temperature, at which the s-trans form makes up approximately 96% of acrolein, only the s-trans form of acrolein was considered.

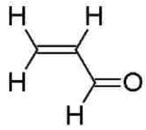

Figure 3.1. The molecular structure of s-trans-acrolein is shown above. At room temperature, 96% of acrolein exists in the s-trans form.

As described in this chapter, high resolution photoelectron spectroscopy was used to obtain vibrational branching ratios as functions of photon energy for the $\tilde{X}\ ^2A'$ ionic state of acrolein. Evidence from both experimental and calculated results is shown for low energy shape resonances in acrolein.

3.2 ADDITIONAL EXPERIMENTAL DETAILS

Acrolein is a liquid sample at room temperature, with a vapor pressure of 209.4 torr at 20 °C. All the acrolein experiments here used only the vapor pressure of room temperature acrolein attached to an external gas manifold without a carrier gas. Anhydrous acrolein with 99.0% purity was acquired from Sigma-Aldrich.

Data were collected for photon energies ranging from 17.5 to 140 eV. The pass energy was set according to photon energy; for $h\nu \leq 60$ eV, the pass energy was set to 10 eV, and for $h\nu > 60$ eV, the pass energy was set to 20 eV. The slit between the exit of the einzel lens and the entrance to the analyzer was set to 0.200 mm, resulting in a full-width at half-maximum (fwhm) of 19.0 and 23.8 meV at the lower and higher pass energies, respectively, for the Xe $^2P_{3/2}$ peak. These settings corresponded to an fwhm of approximately 20.5 and 29.3 at the lower and higher pass energies for a single vibrational mode in the $\tilde{X}\ ^2A'$ ionic state of acrolein.

3.3 COMPUTATIONAL METHODS

The experimental branching ratios for acrolein's $\tilde{X}\ ^2A'$ ionic state were compared with calculations performed by the research group of Dr. Robert Lucchese at Texas A&M University in College Station, Texas. Vibrational-state transitions were calculated at fixed nuclear positions using the Gaussian09[19] software package with the augmented correlation-consistent polarized valence triple-ζ, aug-cc-pVTZ, basis set. These calculations were used not only to verify the experimental data but also to elucidate which electron dynamics lead to the features seen in the experimental data.

Then the photoionization cross sections were calculated using the Schwinger variational method with Pade corrections.[20] The Schwinger variational method is one of several methods which can be used to calculated scattering processes; however, Schwinger variational method has some distinct advantages over other methods. When using the Schwinger variational method, the results are independent of the normalization of the trial wave function; relatively accurate results can be obtained using limited-basis set expansions, and this method does not have the singularity issues that arise when using the other algebraic methods for calculating scattering processes.[21] The Schwinger variational method has been shown to produce valid results for scattering calculations.[21-23] The partial waves of the scattering amplitude were the desired outcomes of these calculations. Further details of the application of the Schwinger variational principle for scattering processes has been described elsewhere.[21-23]

The scattering S-matrix poles were analyzed using local exchange potential and local adiabatic state-model-exchange to confirm the presence of shape resonances. The S-matrix, or scattering matrix, relates the initial and final states of a system undergoing a scattering process. An isolated pole in the S-matrix is generally evidence of a resonant feature.[24,25]

Finally, the theoretical results and the experimental vibrational branching ratios were both converted into electronic factors for easier comparison. Electronic factors have been described in great detail elsewhere and thus will be reviewed only briefly here.[11] The electronic factors, F, were calculated for the theoretical data using the following equation

$$F = \left(\frac{d}{dq}\ln\sigma(q)\right)_{q=0} \qquad \text{(Equation 3.1)}$$

where $\sigma = \sigma^{(0)} + q\sigma^{(i)}$ is the total cross section, $\sigma^{(i)}$ is the *i*th derivative of the total fixed nuclei cross section, and q is the vibrational mode coordinate. In order to convert the experimentally measured vibrational branching ratios into electronic factors, the following equation was used

$$F = \pm\left(2R^{(FC)}_{i\leftarrow 0/0\leftarrow 0}\right)^{1/2}\left[\frac{R_{i\leftarrow 0/0\leftarrow 0}}{R^{(FC)}_{i\leftarrow 0/0\leftarrow 0}} - 1\right] \qquad \text{(Equation 3.2)}$$

where $R^{(FC)}$ is the vibrational branching ratio predicted by the Franck-Condon principle, and R is the calculated or measured vibrational branching ratio for a specified vibrational transition. By presenting the data in the form of the electronic factors, breakdown of the Franck-Condon principle can be compared across systems with various frequencies and bond shifts during the ionization process, since the total cross section is dependent on the internuclear distance.[11]

3.4 RESULTS

The fitted photoelectron spectrum of acrolein's $\tilde{X}\ {}^2A'$ ionic state taken at 19 eV is shown in Figure 3.2 with select vibrational peaks labeled. For the ground ionic state, the vibrational mode energy spacings obtained from infrared studies of the neutral molecules are generally a reasonable approximation for the ionic vibrational mode energy spacings. In the fittings of the acrolein data presented here, the neutral acrolein infrared data was used to approximate the binding energy differences between the ground state vibrational mode and all other vibrational peaks.

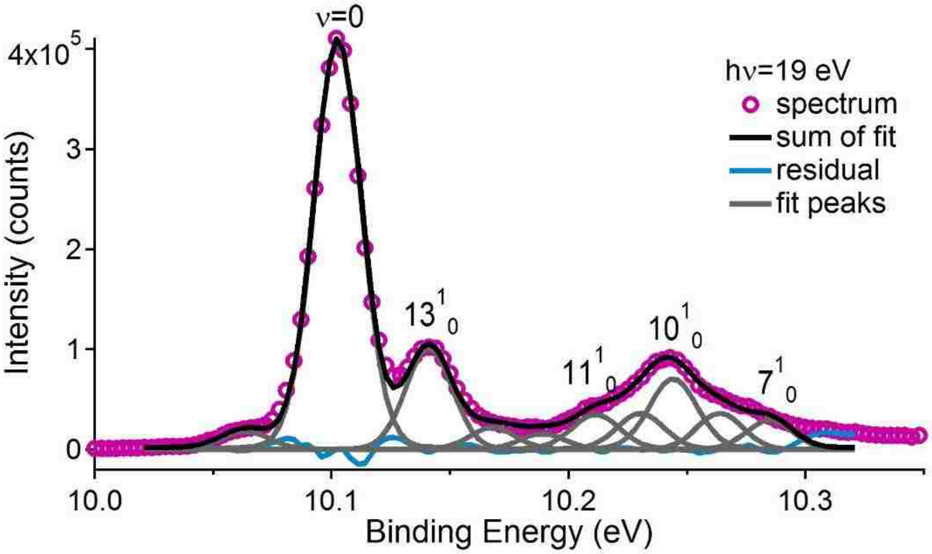

Figure 3.2. The fitted photoelectron spectrum of the $\tilde{X}\ ^2A'$ ionic state of acrolein obtained at photon energy 19 eV is shown on a binding energy scale in eV. The raw spectrum is shown in pink open circles, the fitted peaks are shown as grey solid lines, the sum of the fitted peaks is shown as a black solid line, and the residual of the fit is shown as a blue solid line.

The vibrational modes of acrolein relevant to this study, along with their binding energies in eV and descriptions, are presented in Table 3.1. All 18

Table 3.1. The vibrational peaks used in the fitting of the acrolein photoelectron spectra are shown along with their binding energies in eV and the description of their motion, when available.

Vibrational Mode	Binding Energy (eV)	Description
ν_{13}	10.14	C-C-C bending
ν_{12}	10.17	C-C-O bending
unknown	10.19	
ν_{11}	10.21	=CH2 rocking
unknown	10.23	
ν_{10}	10.24	C-C stretching
ν_9 or ν_8	10.26	CH bending
ν_7	10.29	=CH2 scissoring

vibrational modes of ground state neutral acrolein have been described in detail previously.[26-28] The vibrational modes used in the fitting of this data were all in-plane modes with A' symmetry.

From each fitted spectra, ratios between the intensities of vibrational peaks to the ground vibrational peak were plotted as functions of photon energy. Since these data were collected at the magic angle, as discussed in Chapter 2, Section 2.3, the ratio ofvibrational peak intensities is equivalent to the vibrational branching ratios. A subset of these branching ratios are shown in Figure 3.3. The baselines for the

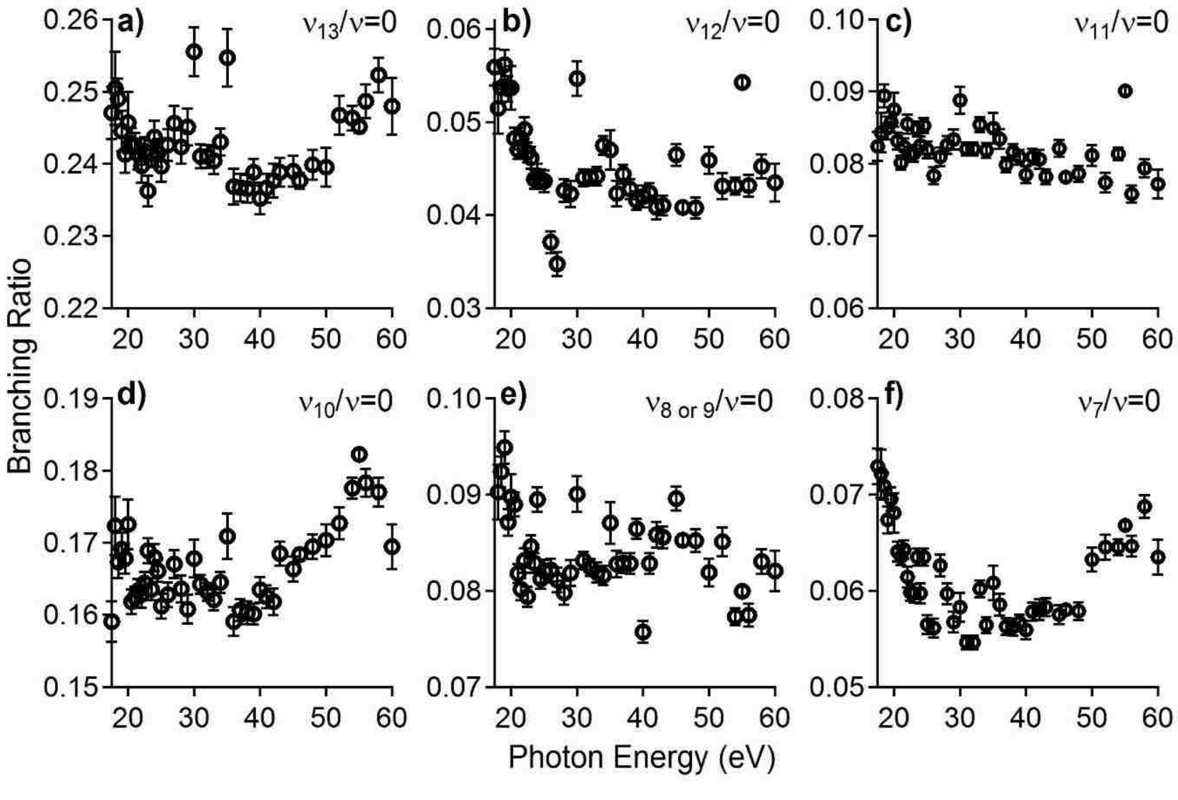

Figure 3.3. The experimentally measured vibrational branching ratios of acrolein's $\tilde{X}\ ^2A'$ ionic state for the following modes: (a) ν_{13}, (b) ν_{12}, (c) ν_{11}, (d) ν_{10}, (e) ν_8 or ν_9, and (f) ν_7 all compared to the ground vibrational state. A low energy feature occurred below 17.5 eV, the lowest photon energy at which data was collected, and a higher energy feature centered at 55 eV occurred in some vibrational branching ratio curves.

vertical axes in Figure 3.3 are offset from zero. The data shown in Figure 3.3 were truncated at 70 eV since the data became more scattered at higher photon energies.

The experimentally measured vibrational branching ratios were compared with the calculated data from Dr. Lucchese's group. These data were published previously.[1] For easier comparison, both the experimental data and the calculated data were converted to electronic factors, F, as described in Section 3.3 of this chapter. The compared electronic factors for select vibrational modes are shown in Figure 3.4.

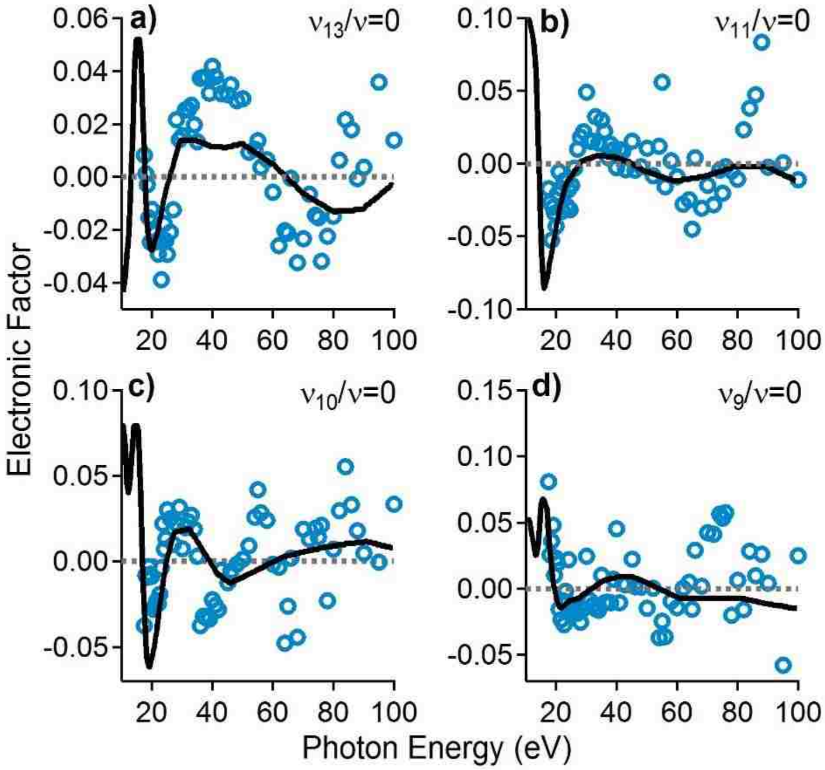

Figure 3.4. The calculated and experimental electronic factors, F, for acrolein's $\tilde{X}\ ^2A'$ ionic state as functions of photon energy (eV) are shown for the following vibrational modes, (a) ν_{13}, (b) ν_{11}, (c) ν_{10}, and (d) ν_9, all compared with the ground vibrational state. The experimental electronic factors are shown as blue open circles, the calculated electronic factors are shown as solid black lines, and the Franck-Condon factors (on an electronic factor scale) are shown as grey dashed lines. Nice agreement was found between the measured and calculated data, particularly at lower photon energies.

3.5 DISCUSSION

The experimental branching ratios shown in Figure 3.2 show evidence for both a low energy and a high energy feature. As seen in Figure 3.2, there appears to be a low energy feature starting below 17.5 eV, the lowest energy at which data was obtained. This low energy feature is likely the shape resonance, known to occur at 15.5 eV in the acrolein $\tilde{X}\ ^2A'$ ionic state. Evidence for this shape resonance occurs in all of the vibrational modes for which branching ratios are shown in Figure 3.2, ν_{13}, ν_{12}, ν_{11}, ν_{10}, ν_8 or ν_9, and ν_7. These vibrational modes correspond to a variety of nuclear motions across the acrolein molecule. Also, from Figure 3.2, there is some evidence for a higher energy feature centered around 55 eV for vibrational modes ν_{13}, ν_{10}, and ν_7. However, the fit of the experimental data in acrolein is likely not free from error. Developing a unique and meaningful fit for the acrolein data was challenging since the vibrational peaks were somewhat overlapped. Due to this issue, comparing the experimental branching ratios with calculations was essential in drawing meaningful conclusions.

In order to compare the calculated and experimental data, both data sets were put into units of electronic factor, which was described in Section 3.3 of this chapter. The electronic factors, presented in Figure 3.4, show reasonable agreement between calculation and experiment at low photon energies with a slight breakdown of this mapping at higher photon energies. Analysis of the S-matrix poles showed evidence of shape resonances at 15.5 and 23.01 eV, as well as evidence for a broad resonant feature at 83.91 eV. From Figure 3.4, the calculated electronic factors all show a sharp peak near 15 eV, which is the lowest energy shape resonance also seen in the experimental data. The evidence for the shape resonance predicted to occur at 23.01 eV is much weaker than that for the lowest energy shape resonance; however, there are weak and slightly broad peaks occurring between 20 and 40 eV for the electronic factors shown in Figure 3.4. There is little to no evidence in the electronic factors presented in Figure 3.4 for the highest energy resonant feature predicted to occur at 83.91 eV. This lack of evidence for the high energy resonant feature was not surprising. The photoionization cross section for acrolein falls off fairly quickly, which explains why the experimental data becomes scattered and unreliable at higher energies. The weak cross section made it difficult to accurately measure the vibrational branching ratios in the energy regime of the higher energy resonant feature.

3.6 SUMMARY

Evidence of two low energy shape resonances, occurring at 15.5 and 23 eV, were seen in vibrational branching ratios obtained from high resolution photoelectron spectroscopy for photoionization leading to the $\tilde{X}\ {}^2A'$ ionic state of acrolein. These data were confirmed with Schwinger variational method calculations. The experimental and calculated electronic factors for several vibrational modes showed decent agreement in the regions of the low energy shape resonances.

With increased molecular complexity, it becomes more difficult to develop the unique and meaningful spectral fits which are necessary to extract the vibrational branching ratios. However, with careful treatment of the data, obtaining information about mode-specific non-Franck-Condon behavior in polyatomic systems is possible, and this data can be further confirmed using calculations.

3.7 REFERENCES

[1] J.A. Lopez-Dominguez, R.R. Lucchese, K.D. Fulfer, D. Hardy, E.D. Poliakoff, A.A. Aguilar, J. Chem. Phys. 141 (2014) 094301.

[2] R.M. Rao, E.D. Poliakoff, K. Wang, V. McKoy, Phys. Rev. Lett. 76 (1996) 2666.

[3] J.S. Miller, E.D. Poliakoff, T.F. Miller, A.P.P. Natalense, R.R. Lucchese, J. Chem. Phys. 114 (2001) 4496.

[4] G.J. Rathbone, E.D. Poliakoff, J. Bozek, R.R. Lucchese, J. Chem. Phys. 114 (2001) 8240.

[5] G.J. Rathbone, E.D. Poliakoff, J. Bozek, R.R. Lucchese, Can. J. Chem. 82 (2004) 1043.

[6] G.J. Rathbone, E.D. Poliakoff, J. Bozek, R.R. Lucchese, Phys. Rev. Lett. 92 (2004) 143002.

[7] G.J. Rathbone, E.D. Poliakoff, J. Bozek, R.R. Lucchese, J. Chem. Phys. 122 (2005) 064308.

[8] G.J. Rathbone, E.D. Poliakoff, J. Bozek, D. Toffoli, R.R. Lucchese, J. Chem. Phys. 123 (2005) 014307.

[9] A. Das, E.D. Poliakoff, R.R. Lucchese, J.D. Bozek, J. Chem. Phys. 130 (2009) 044302.

[10] R.R. Lucchese, R. Montuoro, K. Kotsis, M. Tashiro, M. Ehara, J.D. Bozek, A. Das, A. Landry, J. Rathbone, E.D. Poliakoff, Molecular Physics 108 (2010) 1055.

[11] J.A. Lopez-Dominguez, D. Hardy, A. Das, E.D. Poliakoff, A. Aguilar, R.R. Lucchese, J. Electron. Spectrosc. Relat. Phenom. 185 (2012) 211.

[12] E.D. Poliakoff, R.R. Lucchese, Phys. Scr. 74 (2006) C71.

[13] J.L. Dehmer, J. Chem. Phys. 56 (1972) 4496.

[14] J.L. Dehmer, D. Dill, S. Wallace, Phys. Rev. Lett. 43 (1979) 1005.

[15] J.B. West, A.C. Parr, B.E. Cole, D.L. Ederer, R. Stockbauer, J.L. Dehmer, J. Phys. B.: At. Mol. Opt. Phys. 13 (1980) L105.

[16] M.N. Piancastelli, J. Electron. Spectrosc. Relat. Phenom. 100 (1999) 167.

[17] J.A. Sheeny, T.J. Gil, C.L. Winstead, R.E. Farren, P.W. Langhoff, J. Chem. Phys. 91 (1989) 1796.

[18] L.A. Kelly, L.M. Duffy, B. Space, E.D. Poliakoff, P. Roy, S.H. Southworth, M.G. White, J. Chem. Phys. 90 (1989) 1544.

[19] M.J. Frisch, G.W. Trucks, H.B. Schlegel, e. al., GAUSSIAN 09. Gaussian, Inc., Wallingfor, CT, 2009.

[20] R.R. Lucchese, V. McKoy, Phys. Rev. A 28 (1983) 1382.

[21] D.K. Watson, R.R. Lucchese, V. McKoy, T.N. Rescigno, Phys. Rev. A 21 (1980) 738.

[22] R.E. Stratmann, R.R. Lucchese, J. Chem. Phys. 102 (1995) 8493.

[23] R.E. Stratmann, R.W. Zurales, R.R. Lucchese, J. Chem. Phys. 104 (1996) 8969.

[24] G. Calucci, L. Fonda, G.C. Ghirardi, Phys. Rev. 166 (1968) 1719.

[25] J. Macek, Phys. Rev. A 2 (1970) 1101.

[26] K. Inuzuka, Bulletin of the Chemical Society of Japan 4 (1961) 729.

[27] Y. Hamada, Y. Nishimura, M. Tsuboi, Chem. Phys. 100 (1985) 365.

[28] L.-H. Xu, X. Jiang, H. Shi, R.M. Lees, A.R.W. McKellar, D.W. Tokaryk, D.R.T. Appadoo, J. Mol. Spectrosc. 268 (2011) 136.

CHAPTER 4
MODE-SPECIFIC NON-FRANCK-CONDON BEHAVIOR DURING PHOTOIONIZATION RESULTING IN THE $B\ ^2A'$ IONIC STATE OF THE HALOGENATED THIOPHENES

As discussed in Chapter 3, Mode-Specific Non-Franck-Condon Behavior in Photoionization Resulting in the Acrolein $\tilde{X}\ ^2A'$ Ionic State Due to Shape Resonances, vibrational mode-specific breakdown of the Franck-Condon principle is observable in polyatomic systems. Mode-specificity can add insight to the spatial aspects of resonant and non-resonant electron rescattering dynamics and, as such, is of high interest. This chapter discusses mode-specific breakdown of the Franck-Condon Principle due to nonresonant electron rescattering dynamics in photoionization resulting in the $B\ ^2A'$ ionic states of the 2-chlorothiophene, 2-bromothiophene, 3-chlorothiophene, and 3-bromothiophene.

4.1 HALOGENATED THIOPHENES

Photoionization of the halogen-substituted aromatic ring systems are known to be affected by Cooper minima from atomic-like orbitals.[1-5] The measured photoelectron asymmetry parameters for several electronic states of 2-chlorothiophene and 3-chlorothiophene were previously reported to show evidence of the Cooper minimum from the chlorine 3p orbital.[1] Also, the measure photoelectron asymmetry parameters for several electronic states of 2-bromothiophene and 3-bromothiophene were previously reported to show evidence of the Cooper minimum from the bromine 4p orbital and the sulfur 3p orbital.[2] The Cooper minima for the chlorine 3p orbital and the sulfur 3p orbital are too closely spaced in energy for both minima to be visible in the 2- and 3-chlorothiophene photoelectron spectroscopy data.[1]

Much like acrolein, in the previous chapter, all four of the halogenated thiophenes discussed here are of very low symmetry, belonging to the C_s point group. So, the data presented in this chapter furthers the concept of exploring vibrational mode-specific correlations between the electronic and nuclear degrees of freedom in molecules of low symmetry.

This study analyzed the photoelectron spectra of both the 2- and 3-derivatives of the chlorinated and brominated thiophenes over a broad range of photon energies. In this study, the vibrational branching ratios were measured, as opposed to the asymmetry parameters, which were previously reported by another group.[1,2]

4.2 ADDITIONAL EXPERIMENTAL DETAILS

The halogenated chlorothiophenes are all liquid samples at room temperature with relatively high vapor pressures ranging from 3.4 to 13.0 torr at 25 °C. All samples were obtained from Sigma-Aldrich. The 2-chlorothiophene used had a purity of 96%; the 3-chlorothiophene had a purity of 98%; the 2-bromothiohpene used had a purity of 98%; and the 3-bromothiophene had a purity of 97%.

Data were collected for photon energies ranging from 17 to 150 eV. The pass energy was set to 20 eV for photon energies below 60 eV. The slit between the exit of the einzel lens and the entrance to the analyzer was set to 0.100 mm, resulting in a full-width at half-maximum (fwhm) of 19.0 meV for the Xe $^2P_{3/2}$ peak. These settings corresponded to a best fwhm of approximately 14.5 meV for a single vibrational mode in the $B\ ^2A'$ ionic state of 2-bromothiophene. For photon energies above 60 eV, the pass energy was set to 20 eV. At the higher pass energy, these settings corresponded to an fwhm of 23.79 meV for the Xe $^2P_{3/2}$ peak and a best fwhm 28.3 meV for a single vibrational mode in the $B\ ^2A'$ ionic state of 2-bromothiophene.

4.3 RESULTS

The results of photoionization leading to the $B\ ^2A'$ states of ionic 2-chlorothiophene, 3-chlorothiophene, 2-bromothiophene, and 3-bromothiophene are presented in that order. The structures of these four halogenated thiophenes are shown in Figure 4.1.

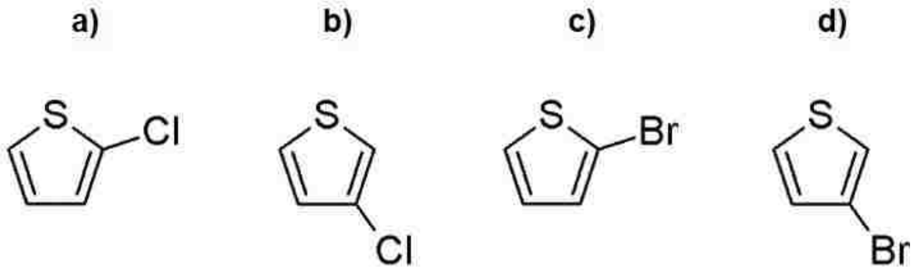

Figure 4.1. The structures of (a) 2-chlorothiophene, (b) 3-chlorothiophene, (c) 2-bromothiophene, and (d) 3-bromothiophene.

4.3.1 2-Chlorothiophene

Photoionization leading to the $B\ ^2A'$ ionic state of 2-chlorothiophene is known to be affected by the chlorine 3p Cooper minimum at approximately 40 eV.[1] High resolution photoelectron spectra of the $B\ ^2A'$ ionic state of 2-chlorothiophene were collected from 17.5 to 90 eV and fitted using the vibrational modes reported for photoelectron data by Trofimov, et al.[1] The overall energies of the vibrational peaks were allowed to vary; however, the energy spacings between neighboring peaks were fixed throughout the fitting procedure. A photoelectron spectrum of the $B\ ^2A'$ ionic state of 2-chlorothiophene at a photon energy of 25 eV is shown in Figure 4.2. Overlaid with the raw data in Figure 4.2 are the fitted peaks, the residual of the fit, and the sum of the fit. The horizontal axis of Figure 4.2 is electron binding energy in eV, while the vertical axis is electron counts.

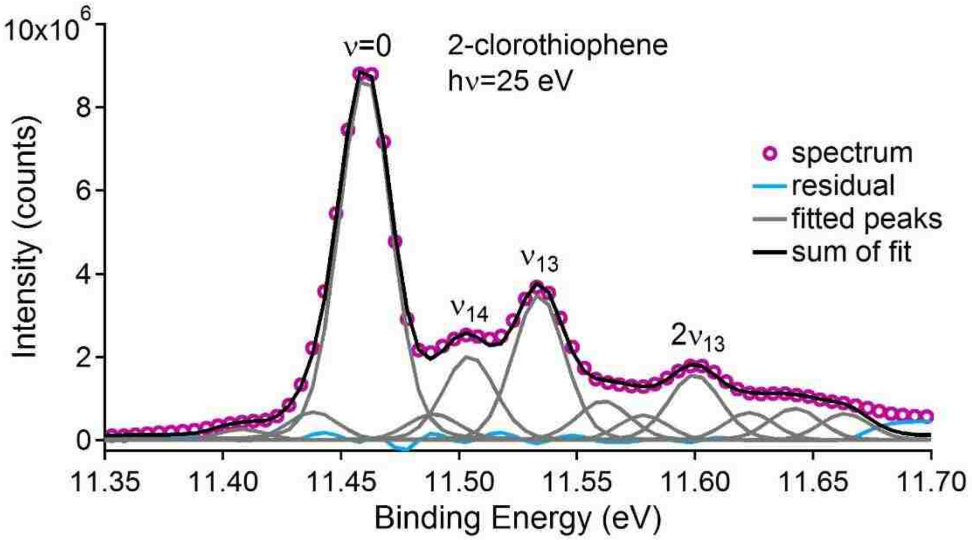

Figure 4.2. The fitted photoelectron spectrum of the $B\ ^2A'$ ionic state of 2-chlorothiophene obtained at photon energy 25 eV is shown on a binding energy scale in eV. The raw spectrum is shown in pink open circles; the fitted peaks are shown as grey solid lines; the sum of the fitted peaks is shown as a black solid line; and the residual of the fit is shown as a blue solid line.

The fit of the 2-chlorothiophene data was based on the vibrational peaks previously reported in the photoelectron data by Trofimov, et al.[1] and described by Horak, et al.[6] Table 4.1 contains a list of the vibrational peaks used in the fit, along with their energy spacing in meV and their description. Vibrational modes 13, 14, and 15, which are all ill-defined halogen sensitive modes, were used to fit the photoelectron spectrum of the $B\ ^2A'$ ionic state of 2-chlorothiophene.

Table 4.1. The vibrational peaks used in the fitting of the photoelectron spectra for the $B\ ^2A'$ ionic state of 2-chlorothiophene are shown, along with their energy spacing (in meV) and the description of their motion. The vibrational mode binding energies were based on those reported by Trofimov, et al.,[1] and the mode descriptions were described by Horak, et al.[6]

Vibrational Mode	Energy Spacing (meV)	Description
ν_{15}	29.4	Ill-described halogen-sensitive mode
ν_{14}	44.4	Ill-described halogen-sensitive mode
ν_{13}	74.3	Ill-described halogen-sensitive mode
$\nu_{13}+\nu_{15}$	100.4	
$\nu_{13}+\nu_{14}$	118	
$2\nu_{13}$	139.8	
$2\nu_{13}+\nu_{15}$	116.3	
$2\nu_{13}+2\nu_{14}$	181	
$3\nu_{13}$	204	

Vibrational branching ratios were calculated from the fitted photoelectron spectra by taking the ratio of the intensities of each vibrational peak to the intensity of the ground vibrational peak. The 2-chlorothiophene data were truncated at a photon energy of 50 eV due to a high amount of scatter in the higher energy data. The following vibrational branching ratios for the $B\ ^2A'$ ionic state of 2-chlorothiophene are shown in Figure 4.3, (a) $\nu_{13}/\nu = 0$, (b) $2\nu_{13}/\nu = 0$, and (c) $2\nu_{13} + \nu_{15}/\nu = 0$. The horizontal axes in Figure 4.3 is photon energy in eV, while the vertical axes are vibrational branching ratios. The baselines for the vertical axes in Figure 4.3 to emphasize small changes in the vibrational branching ratios.

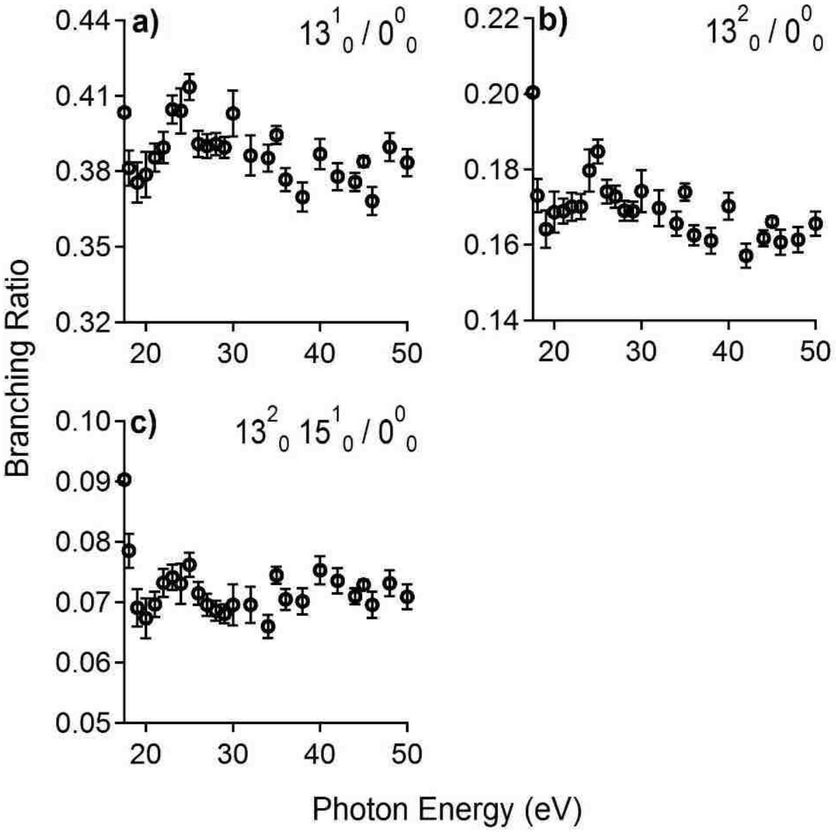

Figure 4.3. The experimentally measured vibrational branching ratios for the following modes of the $B\ ^2A'$ ionic state of 2-chlorothiophene, (a) ν_{13}, (b) $2\nu_{13}$, and (c) $2\nu_{13} + \nu_{15}$ are shown. There appears to be a low energy feature and a weak, broad feature centered around 25 eV occurring in all frames.

4.3.2 3-Chlorothiophene

Similar to 2-chlorothophene, photoionization leading to the $B\ ^2A'$ ionic state of 3-chlorothiophene is also known to be affected by the chlorine 3p Cooper minimum around 40 eV.[1] High resolution photoelectron spectra of the $B\ ^2A'$ ionic state of 3-chlorothiophene were collected from 21 to 120 eV and fitted using the vibrational modes for photoelectron data Trofimov, et al. reported.[1] A photoelectron spectrum of the $B\ ^2A'$ ionic state of 3-chlorothiophene at a photon energy of 23 eV is shown in Figure 4.4. Overlaid with the raw data in Figure 4.4 are the fitted peaks, the residual of the fit, and the sum of the fit. The horizontal axis of Figure 4.4 is electron binding energy in eV, while the vertical axis is electron counts.

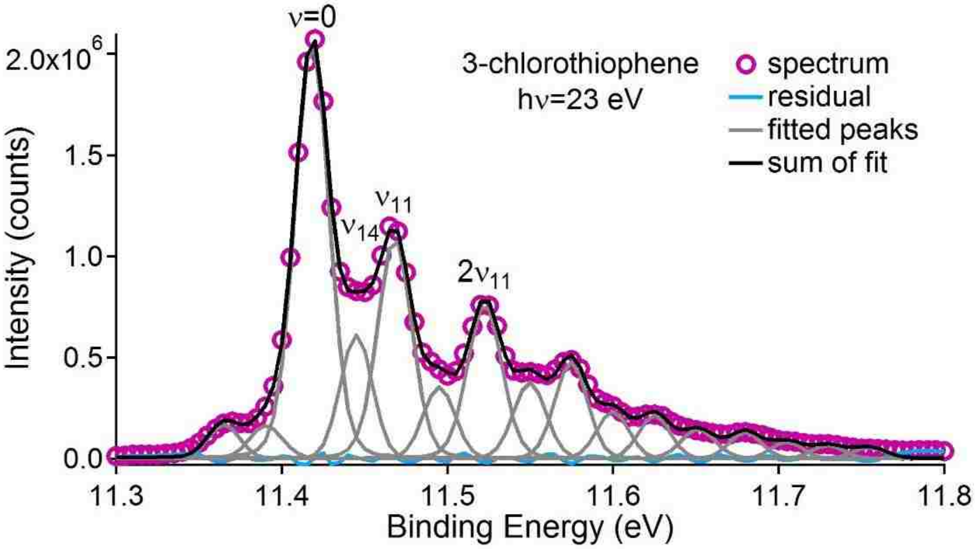

Figure 4.4. The fitted photoelectron spectrum of the $B\ ^2A'$ ionic state of 3-chlorothiophene obtained at photon energy 23 eV is shown on a binding energy scale in eV. The raw spectrum is shown in pink open circles; the fitted peaks are shown as grey solid lines; the sum of the fitted peaks is shown as a black solid line; and the residual of the fit is shown as a blue solid line.

The fitting parameters for the 3-chlorothiophene data were based on the vibrational peaks previously reported in the photoelectron data by Trofimov, et al.[1] and described by Horak, et al.[6] The vibrational modes descriptions came from the work of Paliani, et al.[7] Table 4.2 contains a list of the vibrational peaks used in the fit, with their energy spacing in meV and the description of their motion. Vibrational modes 11 and 14 were used to fit the photoelectron spectrum of the $B\ ^2A'$ ionic state of 3-chlorothiophene. Vibrational mode 11 is a stretching mode along the C-Cl bond, while mode 14 is described as a combined ring stretching and deformation mode.

Table 4.2. The vibrational peaks used in the fitting of the photoelectron spectra for the $B\ ^2A'$ ionic state of 3-chlorothiophene are shown along with their binding energies in eV and the description of their motion. The vibrational modes were described by Paliani, et al.[7]

Vibrational Mode	Energy Spacing (meV)	Description
ν_{14}	27.1	C-Cl stretching
ν_{11}	50	Ring stretching + deformation
$\nu_{14}+\nu_{11}$	76	
$2\nu_{11}$	104	
$2\nu_{11}+\nu_{14}$	131.2	
$3\nu_{11}$	155.8	
$3\nu_{11}+\nu_{14}$	181.4	
$4\nu_{11}$	208.8	
$4\nu_{11}+\nu_{14}$	235.1	
$5\nu_{11}$	261	

Vibrational branching ratios were calculated from the fitted photoelectron spectra as described above in Section 4.3.1. The following vibrational branching ratios for the $B\ ^2A'$ ionic state of 3-chlorothiophene are shown in Figure 4.5, (a) $\nu_{14}/\nu = 0$, (b) $\nu_{11}/\nu = 0$, (c) $\nu_{11} + \nu_{14}/\nu = 0$, (d) $2\nu_{11}/\nu = 0$, (e) $2\nu_{11} + \nu_{14}/\nu = 0$, and (f) $3\nu_{11}/\nu = 0$. The horizontal axes in Figure 4.5 are photon energy in eV, while the vertical axes are vibrational branching ratios. The baselines for the vertical axes in Figure 4.5 are offset from zero in order to further emphasize small changes in the vibrational branching ratios.

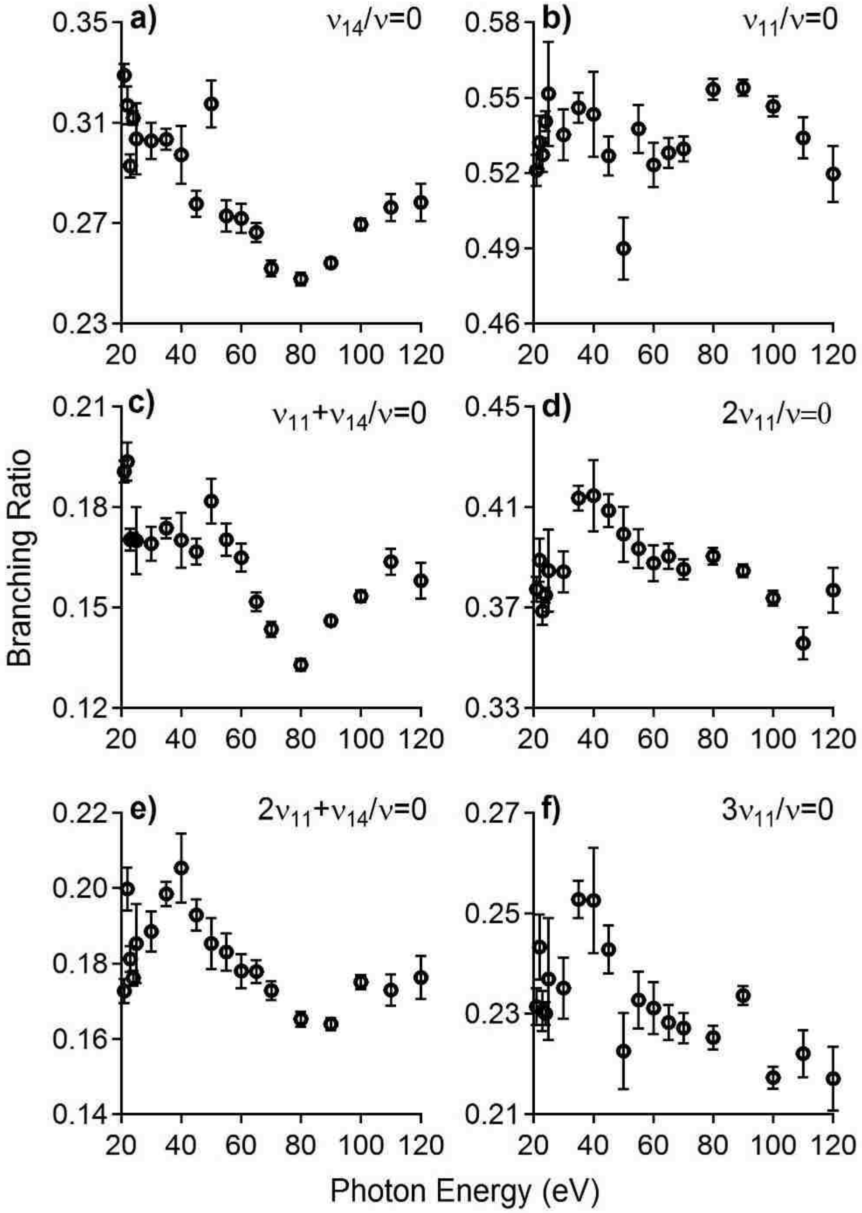

Figure 4.5. The experimentally measured vibrational branching ratios for the following modes of the $B\ ^2A'$ ionic state of 3-chlorothiophene, (a) ν_{14}, (b) ν_{11}, (c) $\nu_{11} + \nu_{14}$, (d) $2\nu_{11}$, (e) $2\nu_{11} + \nu_{14}$, and (f) $3\nu_{13}$. There appears to be a broad feature around 40 eV occurring in frames (c), (d), (e), and (f). There is also a broad negative feature around 80 eV occurring in frames (a), (b), and (c).

4.3.3 2-Bromothiophene

In photoionization leading to the $B\ ^2A'$ ionic state of 2-bromothiophene, the asymmetry parameter is known to be affected not only by the bromine 4p Cooper minimum at approximately 70 eV, but also by the sulphur 3p Cooper minimum.[2] High resolution photoelectron spectra of the $B\ ^2A'$ ionic state of 2-bromothiophene were collected from 17 to 150 eV and fitted using the vibrational modes reported for photoelectron data by Potts, et al.[2] A photoelectron spectrum of the $B\ ^2A'$ ionic state of 2-bromothiophene at a photon energy of 20 eV is shown in Figure 4.6. Overlaid with the raw data in Figure 4.6 are the fitted peaks, the residual of the fit, and the sum of the fit. The horizontal axis of Figure 4.6 is electron binding energy in eV, while the vertical axis is electron counts.

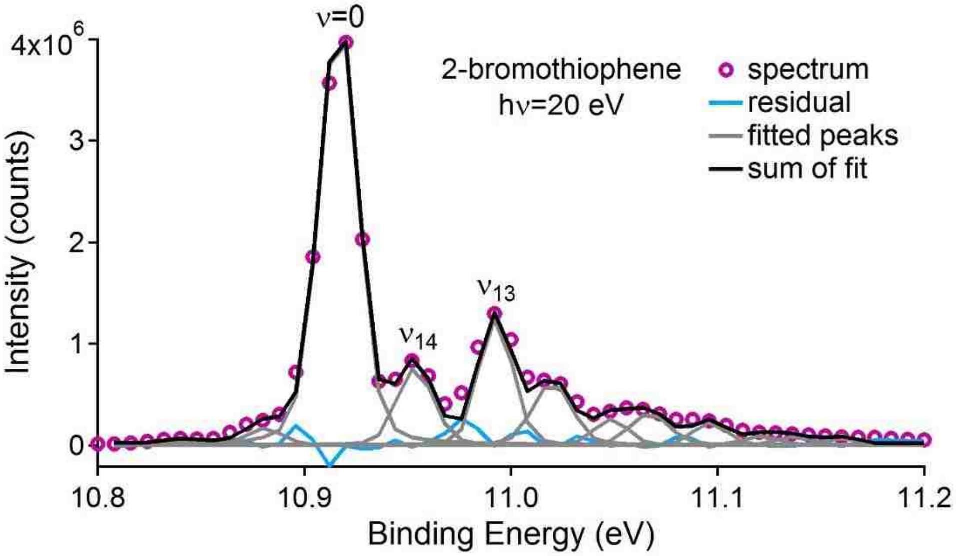

Figure 4.6. The fitted photoelectron spectrum of the $B\ ^2A'$ ionic state of 2-bromothiophene obtained at photon energy 20 eV is shown on a binding energy scale in eV. The raw spectrum is shown in pink open circles; the fitted peaks are shown as grey solid lines; the sum of the fitted peaks is shown as a black solid line; and the residual of the fit is shown as a blue solid line.

The fitting parameters for the 2-bromothiophene data were based on the vibrational peaks previously reported in the photoelectron data by Potts, et al.[2] and by Rabalais, et al.[8] and described by Horak, et al.[6] Table 4.3 contains a list of the vibrational peaks used in the fit, along with their energy spacing in meV and their description. Vibrational modes 13 and 14, which are both complex halogen sensitive modes, were used to fit the photoelectron spectrum of the $B\ ^2A'$ ionic state of 2-bromothiophene.

Table 4.3. The vibrational peaks used in the fitting of the photoelectron spectra for the $B\ ^2A'$ ionic state of 2-bromothiophene are shown along with their energy spacing in meV and the description of their motion. The vibrational mode binding energies were based on those reported by Rabalais, et al.[8] The modes were described by Horak, et al.[6]

Vibrational Mode	Energy Spacing (meV)	Description
ν_{14}	37.7	Ill-described halogen-sensitive mode
$2\nu_{14}$	63.8	Ill-described halogen-sensitive mode
ν_{13}	79.3	
$\nu_{13}+\nu_{14}$	106	
$\nu_{13}+2\nu_{14}$	132.7	
$2\nu_{13}$	160	
$2\nu_{13}+\nu_{14}$	185	
$2\nu_{13}+2\nu_{14}$	219	
$3\nu_{13}$	240	
$3\nu_{13}+\nu_{14}$	270	

The following vibrational branching ratios for the $B\ ^2A'$ ionic state of 2-bromothiophene are shown in Figure 4.7, (a) $\nu_{14}/\nu = 0$, (b) $2\,\nu_{14}/\nu = 0$, (c) $\nu_{13}/\nu = 0$, (d) $\nu_{13} + \nu_{14}/\nu = 0$, (e) $2\nu_{13}/\nu = 0$, and (f) $2\nu_{13} + \nu_{14}/\nu = 0$. The horizontal axes in Figure 4.7 are photon energy in eV, while the vertical axes are vibrational branching ratios. The baselines for the vertical axes in Figure 4.7 are offset from zero in order to emphasize small changes in the vibrational branching ratios.

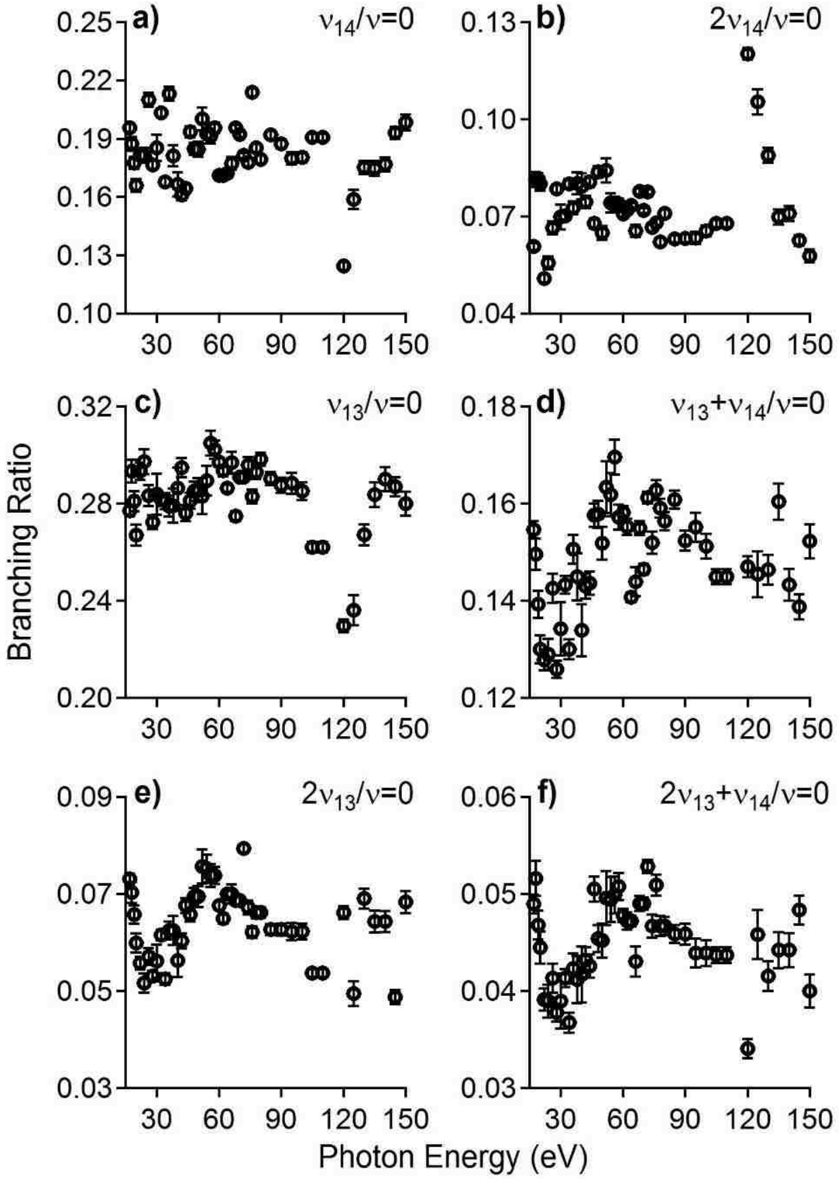

Figure 4.7. The experimentally measured vibrational branching ratios for the following modes of the $B\ ^2A'$ ionic state of 2-bromothiophene, (a) ν_{14}, (b) ν_{13}, (c) $\nu_{13}+\nu_{14}$, (d) $2\nu_{14}$, (e) $2\nu_{13}$, and (f) $2\nu_{13}+\nu_{14}$. There appears to be a low energy feature and a broad feature around 55 eV occurring in frames (c), (e), and (f). There is a sharp, strong feature occurring at 120 eV in frames (a), (b), and (d).

4.3.4 3-Bromothiophene

Photoionization leading to the $B\ ^2A'$ ionic state of 3-bromothiophene is known to be affected by the bromine 4p Cooper minimum at approximately 70 eV.[2] High resolution photoelectron spectra of the $B\ ^2A'$ ionic state of 3-bromothiophene were collected from 17 to 110 eV and fitted using the vibrational modes reported for photoelectron data by Rabalais, et al.[8] A photoelectron spectrum of the $B\ ^2A'$ ionic state of 3-bromothiophene at a photon energy of 20 eV is shown in Figure 4.8. Overlaid with the raw data in Figure 4.8 are the fitted peaks, the residual of the fit, and the sum of the fit. The horizontal axis in Figure 4.8 is electron binding energy in eV, while the vertical axis is electron counts.

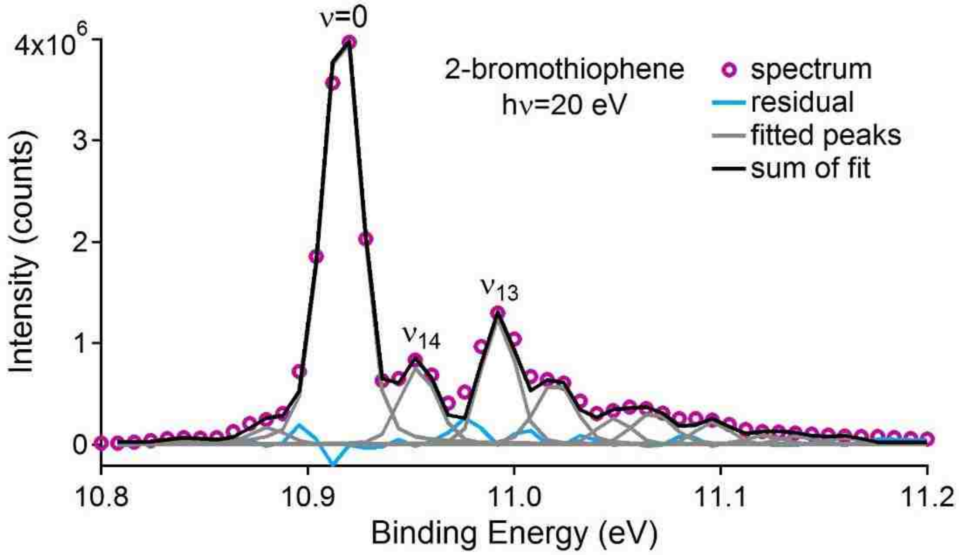

Figure 4.8. The fitted photoelectron spectrum of the $B\ ^2A'$ ionic state of 3-bromothiophene obtained at photon energy 20 eV is shown on a binding energy scale in eV. The raw spectrum is shown in pink open circles; the fitted peaks are shown as grey solid lines; the sum of the fitted peaks is shown as a black solid line; and the residual of the fit is shown as a blue solid line.

The fit of the 3-bromothiophene data was based on the vibrational peaks previously reported in the photoelectron data by Rabalais, et al.[8] and described by Paliani, et al.[7] Table 4.4 contains a list of the vibrational peaks used in the fit, with their energy spacing in meV and their description. Vibrational modes 11 and 13 were used to fit the photoelectron spectrum of the $B\ ^2A'$ ionic state of 2-chlorothiophene.

Table 4.4. The vibrational peaks used in the fitting of the photoelectron spectra for the $B\ ^2A'$ ionic state of 3-bromothiophene are shown along with their energy spacing in meV and the description of their motion. The vibrational mode binding energies were based on those reported by Rabalais, et al.[8] The modes were described by Paliani, et al.[7]

Vibrational Mode	Energy Spacing (meV)	Description
ν_{14}	36.1	C-Br stretching
$2\nu_{14}$	78.0	
ν_{11}	101.7	Ring stretching + deformation
$\nu_{11}+\nu_{14}$	138.5	
$\nu_{11}+2\nu_{14}$	174.8	
$2\nu_{11}$	203.7	
$2\nu_{11}+\nu_{14}$	241	
$2\nu_{11}+2\nu_{14}$	278	
$3\nu_{11}$	306	
$3\nu_{11}+\nu_{14}$	343	
$3\nu_{11}+2\nu_{14}$	380	
$4\nu_{11}$	408	

The following vibrational branching ratios for the $B\ ^2A'$ ionic state of 3-bromothiophene are shown in Figure 4.9, (a) $\nu_{14}/\nu = 0$, $\nu_{11}/\nu = 0$, (b) $\nu_{11} + \nu_{14}/\nu = 0$, (c) $2\nu_{11}/\nu = 0$, (d) $2\nu_{11} + \nu_{14}/\nu = 0$, and (e) $3\nu_{11}/\nu = 0$. A red line was added to frame (e) of Figure 4.9 as a visual guide drawing attention to the trends occurring in the vibrational branching ratios. The horizontal axes in Figure 4.9 are photon energy in eV, while the vertical axes are vibrational branching ratios. The baselines for the vertical axes in Figure 4.9 are offset from zero in order to emphasize small changes in the vibrational branching ratios.

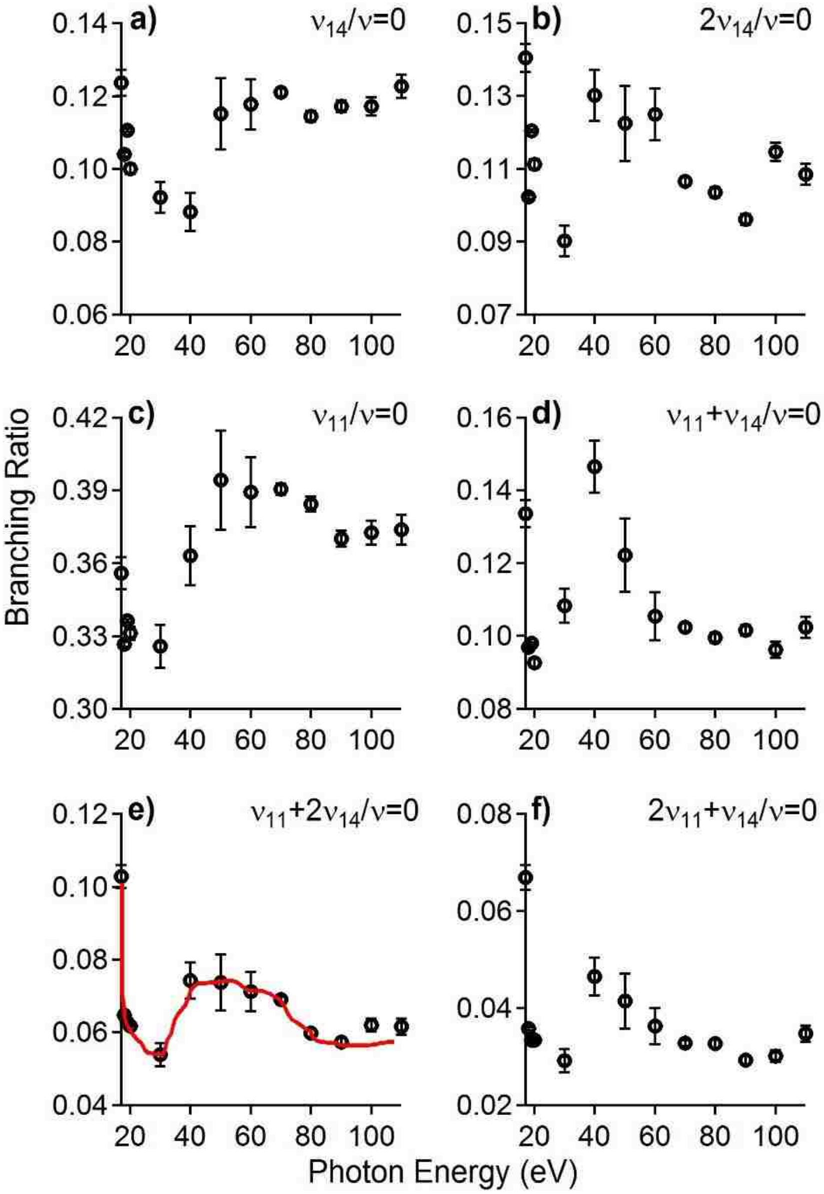

Figure 4.9. The experimentally measured vibrational branching ratios for the following modes of the $B\ ^2A'$ ionic state of 3-bromothiophene, (a) ν_{14}, (b) $2\nu_{14}$, (c) ν_{11}, (d) $\nu_{11}+\nu_{14}$, (e) $\nu_{11}+2\nu_{14}$, and (f) $2\nu_{11}+\nu_{14}$ are shown. The red solid line in (e) is meant to highlight the trends in the branching ratio curves. There appears to be a low energy feature occurring below 17 eV and a broad feature around 50 eV occurring in all frames.

4.4 DISCUSSION

Photoionization leading to the $B\ ^2A'$ ionic state of these halogenated thiophenes is already known to be affected by the chlorine 3p and bromine 4p

Cooper minima. Our vibrational branching ratio data showed further evidence of these effects, as well as other features, which have not been previously reported or explained. The results for each molecule will be discussed separately.

4.4.1 2-Chlorothiophene

The vibrational branching ratios for the $B\ ^2A'$ ionic state of 2-chlorothiophene, as were shown in Figure 4.3, displayed both a near ionization threshold feature and a second, weaker feature centered around 25 eV. The only 2-chlorothiohpene vibrational branching ratios which displayed clear trends contained at least one quanta of ν_{13}. The sharp decrease in the vibrational branching ratios shown in Figure 4.3 at the lowest photon energies is likely the second half of a shape resonant feature, since shape resonances tend to cause sharp features near the ionization threshold energy in the vibrational branching ratios. The feature occurring around 25 eV is quite low in energy to be the chlorine 3p Cooper minimum, which is reported to occur at 40 eV.

4.4.2 3-Chlorothiophene

The vibrational branching ratios for the $B\ ^2A'$ ionic state of 3-chlorothiophene, as were shown in Figure 4.5, present convincing evidence for non-Franck-Condon behavior due to the chlorine 3p Cooper minimum in all ratios containing at least one quanta of ν_{14}. There is some hint of a feature near 40 eV in the vibrational branching ratios containing only ν_{11}; however, it is much less pronounced than in the branching ratios containing ν_{14}. This preferential effect of the Cooper minimum on ν_{14} is expected since ν_{14} is a C-Cl stretching mode, while ν_{11} is a ring stretching mode.

The chlorine 3p Cooper minimum is located nearest to the chlorine atom, which is not in the ring, so modes directly relating to the chlorine atom should be affected.

There are two other features which occur in the vibrational branching ratios containing at least one quanta of ν_{14} for the $B\ ^2A'$ ionic state of 3-chlorothiophene. One is a relatively sharp decrease at the lowest photon energies; this low energy decrease is generally evidence of a shape resonance. This signature of a low energy shape resonance, however, does not occur in the vibrational ratios containing contributions only from ν_{11}. The second feature in the vibrational branching ratios containing ν_{14} is a broad, negative feature occurring around 80 eV. This negative feature has not been previously predicted. For a full understanding of the origins of this higher energy feature, calculated data are required.

4.4.3 2-Bromothiophene

Similar to those of 2-chlorothiophene, the vibrational branching ratios of the $B\ ^2A'$ ionic state of 2-bromothiophene show only weak evidence of the halogen Cooper minimum. The bromine 4p Cooper minimum has been reported to affect photoionization around 70 eV. As seen in Figure 4.7, there is a weak, relatively broad feature centered around 60 eV for the combination bands containing quanta of both ν_{13} and ν_{14}. While it is slightly shifted to lower energy, this feature may be due to the bromine 4p Cooper minimum. Consequently, these combination bands are also the only vibrational branching ratios which show evidence of a low energy shape resonance, with the lowest photon energy data point showing a sharp decrease.

However, a prominent, sharp feature centered around 120 eV occurred in several of the vibrational branching ratio curves for 2-bromothiophene. In some vibrational branching ratio curves, this feature is positive while in others, it is negative. No electron rescattering dynamics have been previously reported at energies this high above the ionization threshold for 2-bromothiophene.

4.4.4 3-Bromothiophene

In photoionization leading to the $B\ ^2A'$ ionic state of 3-bromothiophene, there is evidence of both a low energy shape resonance and effects of the bromine 4p Cooper minimum. The vibrational branching ratios for 3-bromothiophene, as shown in Figure 4.9, display a sharp decrease at the lowest photon energies and a broad peak centered at 40 or 45 eV. This low energy feature, much like in the other halogenated thiophene data, is convincing evidence of a near ionization threshold shape resonance. The broader peak around 40 eV is a bit lower in energy than expected, but this peak is likely due to the bromine 4p Cooper minimum. It is worth noting that, unlike in the 3-chlorothiophene data, the Cooper minimum appears to affect the vibrational branching ratio curves for both ν_{14} and ν_{11} in 3-bromothiohpene.

4.5 SUMMARY

Vibrational branching ratios for the $B\ ^2A'$ ionic states of these halogenated thiophenes showed further evidence of effects by the halogen Cooper minima, which were previously shown. However, these data also presented evidence for mode-specific low-energy shape resonances, as well as some mode-specific higher energy features, which led to non-Franck-Condon behavior. To date there is no clear explanation of the electron rescattering dynamics leading to the higher energy breakdown of the Franck-Condon Principle in these systems; this explanation requires a comparison with calculations. To continue the theme which Chapter 3 began, electron rescattering dynamics, which lead to non-Franck-Condon responses, are visible in larger polyatomic systems. These larger molecules also have rich electronic structure to be explored, which may even be mode-specific in many cases.

4.6 REFERENCES

[1] A.B. Trofimov, J. Schirmer, D.M.P. Holland, L. Karlsson, R. Maripuu, K. Siegbahn, A.W. Potts, Chem. Phys. 263 (2001) 167.

[2] A.W. Potts, A.B. Trofimov, J. Schirmer, D.M.P. Holland, L. Karlsson, Chem. Phys. 271 (2001) 337.

[3] D.M.P. Holland, D. Edvardsson, L. Karlsson, R. Maripuu, K. Siegbahn, A.W. Potts, W. Von Niessen, Chem. Phys. 253 (2000) 133.

[4] A.W. Potts, D. Edvardsson, L. Karlsson, D.M.P. Holland, M.A. MacDonald, M.A. Hayes, R. Maripuu, K. Siegbahn, W. Von Niessen, Chem. Phys. 254 (2000) 385.

[5] D.M.P. Holland, D. Edvardsson, L. Karlsson, R. Maripuu, K. Siegbahn, A.W. Potts, W. Von Niessen, Chem. Phys. 252 (2000) 257.

[6] M. Horak, I.J. Hyams, E.R. Lippincott, Spectrochimica Acta 22 (1966) 1355.

[7] G. Paliani, R. Cataliotti, Spectrochimica Acta 38A (1982) 751.

[8] J.W. Rabalais, L.O. Werme, T. Bergmark, L. Karlsson, K. Siegbahn, Int. J. Mass Spectrom. Ion Phys. 9 (1972) 185.

CHAPTER 5
PHOTOELECTRON SPECTRA OF THE PYRIMIDINE-TYPE NUCLEOBASES

Continuing the trend of building in molecular complexity, this chapter presents a study of the electronic structure of gas phase pyrimidine-type nucleobase monomers using high-resolution photoelectron spectroscopy. Using a combination of high resolution and photon energy-dependent results over a relatively broad energy range, this study shows that photoelectron spectroscopy can provide new insights into the electronic structure of these nucleobases.

5.1 INTRODUCTION TO THE NUCLOEBASES

Since the nucleobases are the fundamental building blocks of DNA and RNA,[1,2] and are essential to all life, they have been the focus of many studies. The electronic structures of the nucleobases have been of particular interest since these molecules are largely involved in biological charge transfer processes.[3] Studying the nucleobases in the gas phase allows for one to isolate monomers and study the properties of individual nucleobases without dimerization or solvation effects.

The first photoelectron spectrum of uracil was published in 1974 by Padva, et al.[4] Shortly after, in 1975, the first photoelectron spectra of cytosine and thymine, were published by Lauer, et al.[5] Since these initial reports, several groups have used photoelectron spectroscopy to study the nucleobases.[6-11] Their photoelectron spectra contain close-lying and overlapping valence electronic bands. To further complicate the interpretation of these photoelectron spectra, some of the nucleobases, namely cytosine, have multiple stable tautomers in the gas phase, as opposed to the one stable conformation in the solid phase.[12] Based on the complexity of these systems – and in particular, the various possible states – it is important to develop additional experimental results which can serve as guideposts in disentangling the electronic structure of these systems. To this end, more highly resolved electron spectroscopic data and, in particular, such data as a function of photon energy have been acquired.

In this chapter, photoelectron spectra with partial vibrational resolution are presented for the pyrimidine-type nucleobases: thymine, uracil and cytosine. Improved resolution has allowed for the electronic origins of the outermost valence electronic states to be identified. Higher resolution photoelectron data may also serve as a guidepost for answering the question as to the σ or π nature of each of the valence states, which has been a point of contention among those studying the electronic structure of the nucleobases.[8,10,13,14] In the case of cytosine, there has also been much disagreement over which tautomers exist in the gas phase.[12,15-24] Better resolution, combined with recently published calculated spectra of cytosine tautomers, gives insight into which cytosine tautomers exist in the gas phase as well as the locations of electronic states arising from these various tautomers. The electronic structural information obtained from the thymine and uracil data will be discussed first, followed by the electronic and tautomeric information extracted from the cytosine data.

5.2 ADDITIONAL EXPERIMENTAL DETAILS

The experimental setup was described in detail in Section 2.1. Since the nucleobase samples are solids, an in-vacuum oven was used to sublimate the sample. This sublimation setup up used was modeled after that used by Trofimov, et al. and Holland, et al. previously to study the nucleobases in the gas phase,[8,10] (and was described in detail in Section 2.1). Touboul, et al. reported that oven vaporization of the nucleobases produces better vibronic resolution at the cost of a lower signal-to-noise ratio compared with aerosol vaporization of these systems.[22]

The pass energy of the analyzer was set at 10 eV for uracil and 20 eV for thymine and cytosine with the slit width set to 0.300 mm between the einzel lens and the analyzer. Using the 0.300 mm slit width and a pass energy of 10 eV resulted in an fwhm of 11.5 meV for the Xe ${}^2P_{1/2}$ peak. At the higher pass energy, the Xe ${}^2P_{1/2}$ peak had an fwhm of 17 meV. The best resolution achieved in the nucleobases spectra was an fwhm of approximately 50 meV for thymine and uracil and an fwhm of 70 eV for cytosine. These widths for the nucleobase samples were likely due to a combination of Doppler broadening and unresolved vibrational and rotational structure. It should be noted that the data presented here were not corrected for the transmission function of the analyzer; this omission should not affect the results of this study since spectral intensity comparisons were made only over a small energy region.

Cytosine data were collected without a carrier gas. Thymine and uracil data were collected using Xe and Ar as carrier gases in order to increase the amount of sample reaching the gas cell. It should be noted that while the Ar appeared to have no significant effects on the spectra, the presence of Xe did introduce additional peaks into the spectra of both thymine and uracil. These additional peaks, caused by interactions between Xe and the sample, were accounted for by comparing the data with Xe carrier to data taken using no carrier gas or Ar as a carrier. In other words, any contributions introduced by the Xe carrier gas were omitted from the analysis and had no significant effects on the data reported here. Powder samples of cytosine, thymine, and uracil were obtained from Sigma-Aldrich with ≥99% purity.

Cytosine data were collected over the oven temperature range 410 K to 534 K without a carrier gas, thymine over the oven temperature range 414 K to 423 K, and uracil over the oven temperature range 419 K to 520 K. For uracil, a temperature dependent study on the overall shape of the photoelectron spectrum was performed to ensure no significant sample degradation occurred over the temperature ranges at which data was collected. For the temperature dependent study, all of the uracil data was collected at photon energy 40 eV over the oven temperature range 439 to 520 K.

5.3 RESULTS

As mentioned previously, a goal of this study was to generate spectra of the nucleobases with higher resolution than had been obtained previously; the cytosine, thymine, and uracil spectra presented here achieve this goal, even showing emerging vibrational structure for the first time. The increase in resolution for the cytosine data was particularly significant. Comparisons of present experimental photoelectron spectra for cytosine, thymine, and uracil with previously published spectra are shown in Figure 5.1.

Due to the relatively high resolution of this data, strong similarities are observable in the individual features of the spectral envelopes for all three molecules. The photoelectron spectra for cytosine, uracil, and thymine are shown in

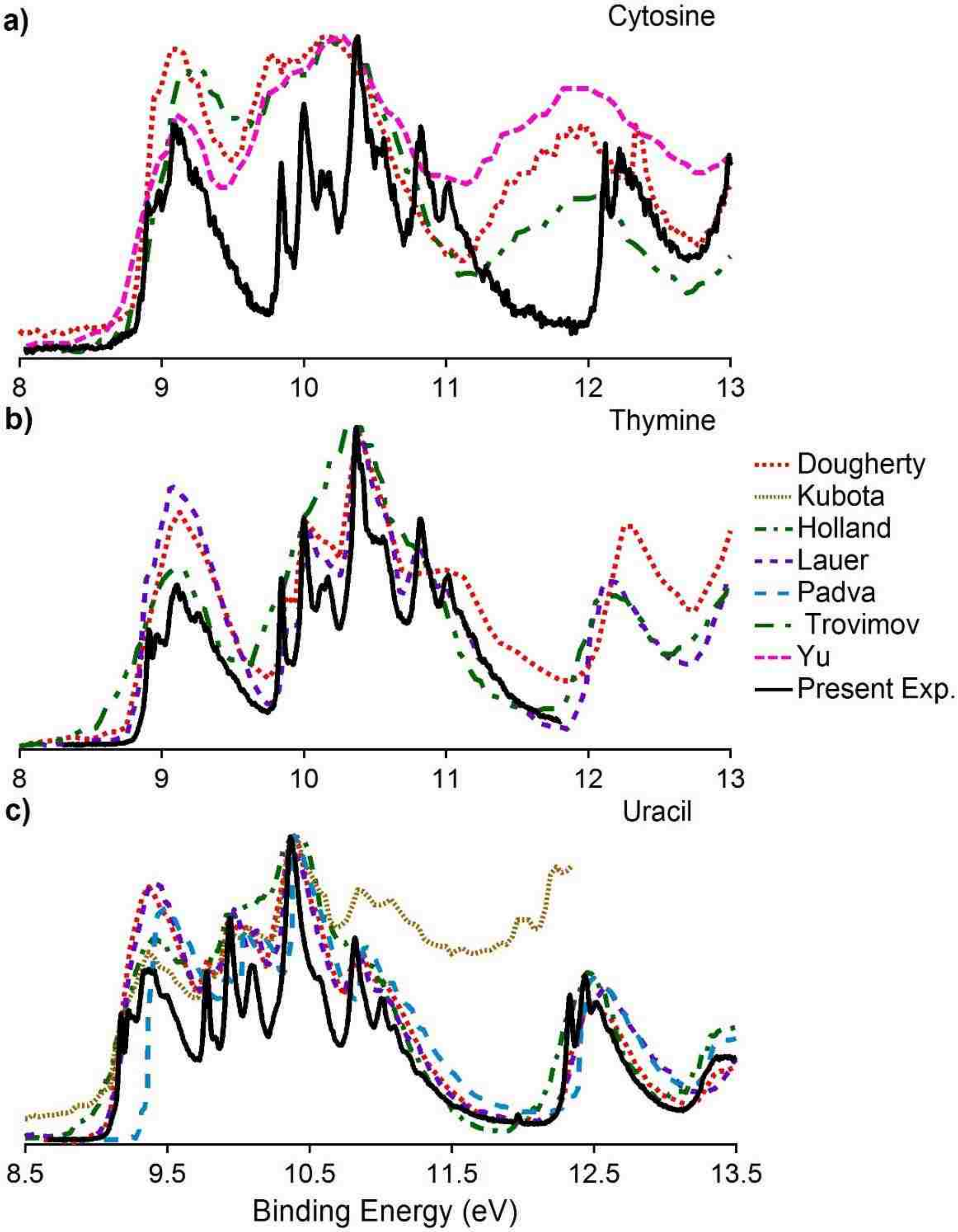

Figure 5.1. Photoelectron spectra from the present experiment are compared with previously published spectra for (a) cytosine (compared with data from Dougherty, et al.;[7] Trofimov, et al.;[8] and Yu, et al.[9]), (b) thymine (compared with data from Dougherty, et al.;[6] Lauer, et al.;[5] and Trofimov, et al.[8]), and (c) uracil (compared with data from Dougherty, et al.;[6] Holland, et al.;[10] Kubota, et al.;[25] Lauer, et al.;[5,17-24] and Padva, et al.[4,15]). All the spectra in this figure are shown on an electron binding energy scale.

Figure 5.2. The binding energy scales for the spectra shown in Figure 5.2 were shifted and scaled to highlight the similarities in the spectral envelopes. These

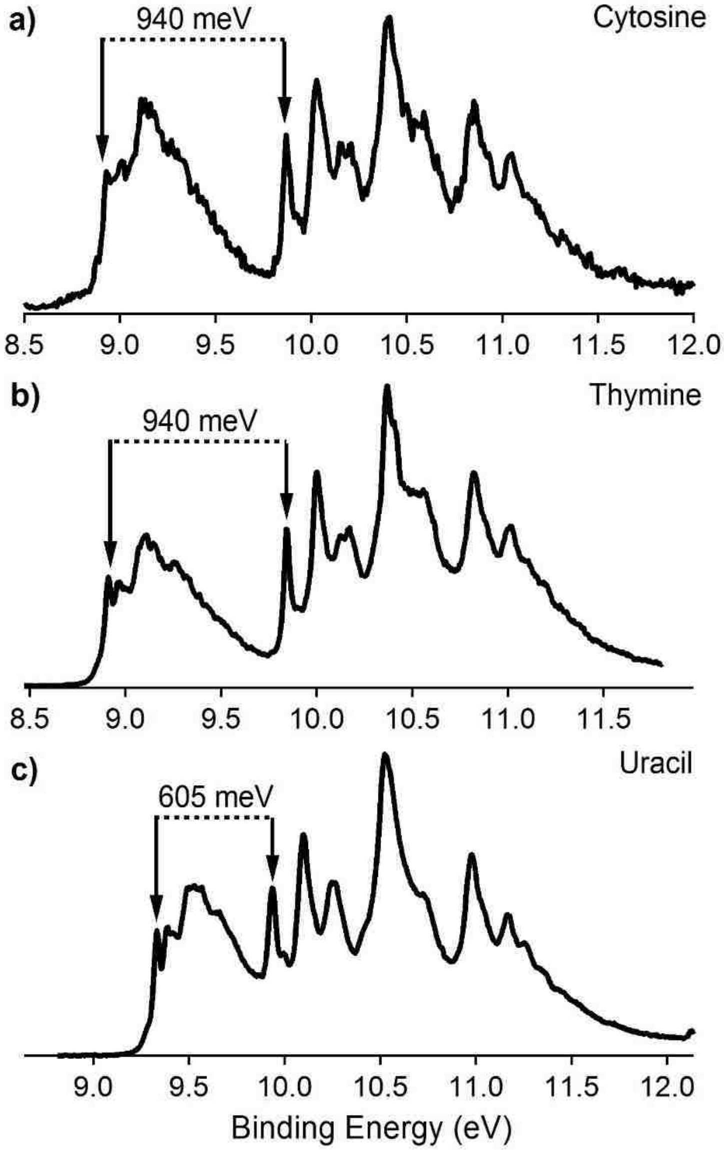

Figure 5.2. The experimental photoelectron spectra of (a) cytosine, (b) thymine, and (c) uracil are shown over 3.5 eV energy windows. The intensity scales are arbitrary. Note the energy scales are different for all three spectra. The energy scales have been adjusted to illustrate the strong similarities among all three spectra. Arrows mark the beginnings of the first two features in each of the spectra. The spacing between the ground and first excited states for cytosine and thymine are the same, but this energy difference is smaller for uracil.

similarities in the spectra for the pyrimidine-type nucleobases will be discussed in more detail in the discussion section.

One issue with studying the nucleobases in the gas phase was the relatively low temperature at which thermal degradation begins to occur, with total thermal decomposition thought to occur around 600 K.[24] Sublimating the nucleobases and obtaining adequate vapor pressure for experimental measurements required relatively high temperatures, 400 to >500 K. The lack of change in appearances of the samples remaining in the block oven after data collection was an indication that no significant thermal degradation occurred. All nucleobase samples were a bright white powder when loaded into the block oven. Upon removing the remaining sample after data collection, the sample would have been light brown if decomposition had begun to occur due to overheating. However, for the data presented here, the remaining samples appeared relatively unchanged from their initial appearance. Furthermore, the photoelectron spectra did not shift significantly over time, nor did the overall spectral envelope change as the data was acquired, suggesting the sample did not decompose.

Figure 5.3 compares seven photoelectron spectra of uracil, all taken at a photon energy of 40 eV, over the following oven (transfer line) temperature ranges: spectrum 1 – 439 to 450 K (456 to 457 K), spectrum 2 – 450 to 455 K (457 to 483 K), spectrum 3 – 456 to 464 K (483 to 495 K), spectrum 4 – 464 to 478 K (496 to 499 K), spectrum 5 – 491 to 506 K (528 to 575 K), and spectrum 6 – 506 to 520 K (575 to 591 K). Each spectrum is characterized by a range of temperatures rather than a single temperature because the data were acquired while the oven was

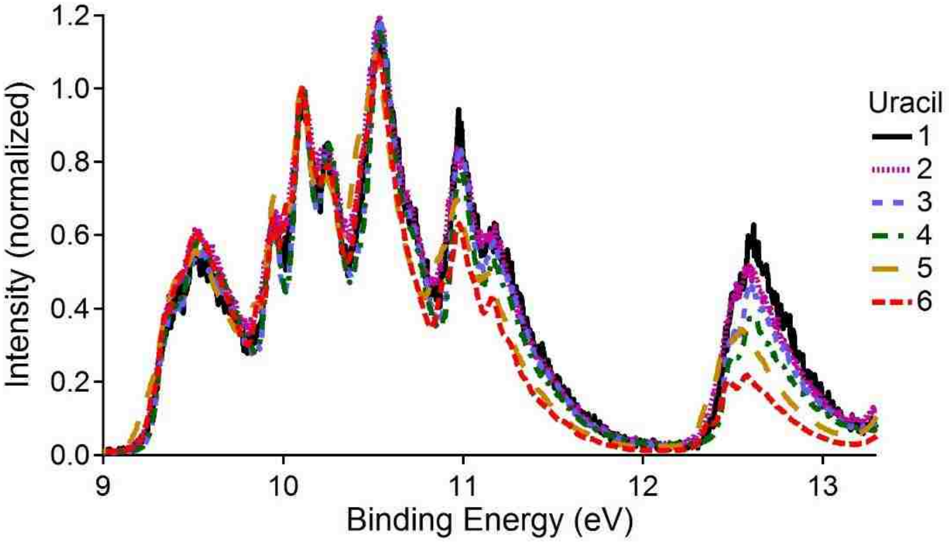

Figure 5.3. Photoelectron spectra of uracil at photon energy 40 eV over the oven temperature range 432 to 520 K are shown. Each spectrum was taken over the oven (transfer line) temperature range: 1 - 439 to 450 K (456 to 457 K), 2 - 450 to 455 K (457 to 483 K), 3 - 456 to 464 K (483 to 495 K), 4 - 464 to 478 K (495 to 499 K), 5 - 491 to 506 K (528 to 575 K) and 6 - 506 to 520 K (575 to 591 K). For easier comparison, all spectra in this figure were normalized at the peak centered at binding energy 10.105 eV.

heating. The overall profile was relatively unchanged with increasing temperature. However, the two electronic states highest in energy, beginning at binding energies 10.95 and 12.4 eV approximately, appear to have increased with increasing temperature, though the overall profiles remained constant. These variations in relative intensity in the highest binding energy features with increasing temperature may be due to vibronic effects. As the temperature of the monomers was increased, the vibrational populations may have changed, causing the relative intensities of the electronic states to appear increased. These variations were not further investigated in this study. Over the temperature range of 432 to 520 K, there were no significant signs of thermal degradation of the uracil sample. Due to the structural similarities between the pyrimidine-type nucleobases, this temperature range was assumed to be appropriate for collecting the thymine and cytosine data as well.

Some signs of thermal degradation of the nucleobases, which are readily apparent in the binding energy range of interest for the nucleobases data, are the production of CO_2, H_2O, and NH_3. Photoionization for the $\tilde{X}\ ^2\Pi_g$ state of CO_2 produces a very sharp peak at binding energy 13.776 eV,[26] from the $\tilde{X}\ ^2A_1$ state of H_2O at binding energy 12.61 eV,[27] and from the $\tilde{X}\ ^1A_1$ state of NH_3 at binding energy 10.073 eV.[28] None of these peaks appeared in any of the data depicted in Figure 5.3.

5.3.1 Thymine Results

Due to the multiple tautomers which contribute to the cytosine photoelectron spectrum, it is difficult to distinguish between the spectra of multiple tautomers overlapping and any vibrational structure from one electronic state. However, for thymine and uracil, this is not an issue since both thymine and uracil each exist only in the diketo form in the temperature range over which data was collected.[29,30] The structures of diketo thymine and uracil are shown in Figure 5.4.

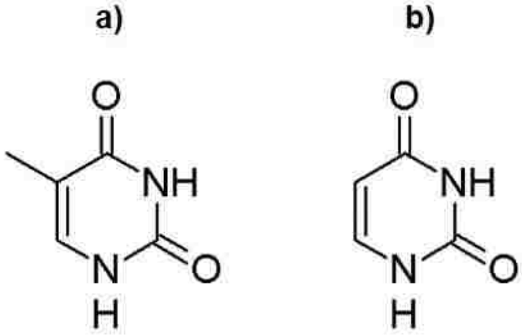

Figure 5.4. The diketo forms of (a) thymine and (b) uracil are shown.

Analyzing the thymine data within the Franck-Condon approximation allowed us to distinguish between vibrational and electronic contributions to the spectrum and separate the various electronic states. While the resolution of the thymine data was much improved over previous results, there was insufficient vibrational resolution to perform a unique and meaningful fit of the spectrum. With that said, an underlying structure is clear for each of the spectra shown, indicating the presence of vibrational substructure. To take advantage of this underlying structure, the thymine spectrum was divided into windows of first 50 meV, then 100 meV. Each window of the spectrum was integrated. By examining the ratios between different integration windows, the electronic states were separated. If the two windows contained only contributions from the same electronic state, the Franck-Condon approximation dictates that the ratio of the integrated values should remain constant with increasing photon energy. However, if the two windows contain contributions from different electronic states, the ratio of the integrated values would not be expected to be independent of photon energy. The window sizes were selected based on the sharpest partially resolved vibrational peak, which averaged a full width at half maximum (fwhm) of 53 meV. Both the 50 meV and 100 meV integrated windows produced the same results, so only the 50 meV data are shown. The thymine photoelectron spectrum taken at a photon energy of 25 eV is displayed in Figure 5.5(a), with selected 50 meV integration windows highlighted in grey. Figure 5.5 also shows the ratios of selected 50 meV integration windows. The ratios of integration windows shown in Figure 5.5(b)-(e) were scaled to emphasize the difference between the ratios which plateau to a constant value and those which do

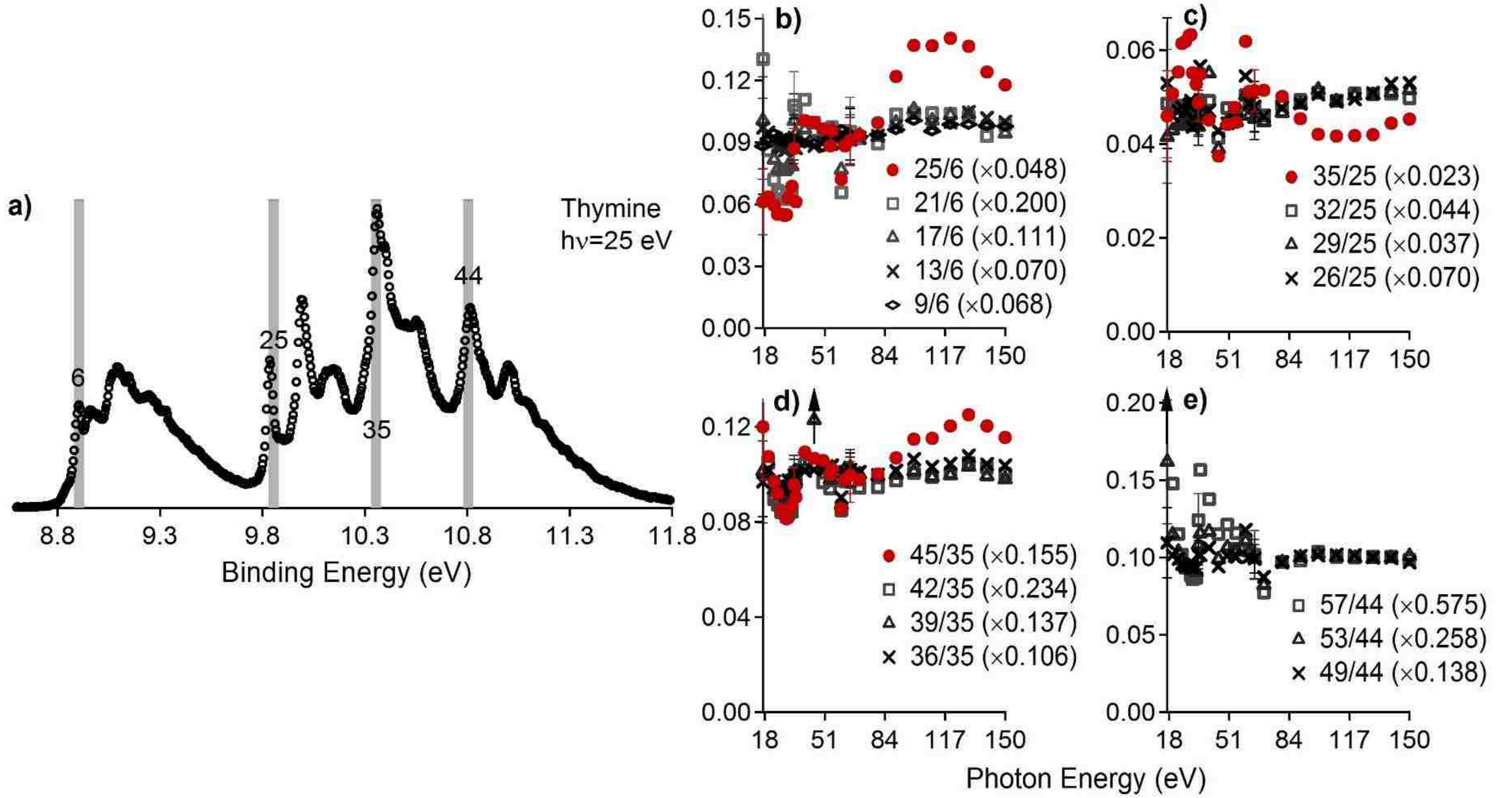

Figure 5.5. (a) The photoelectron spectrum of thymine taken at photon energy 25 eV is shown with the following 50 meV integration regions highlighted - regions 6, 25, 35, and 44. In frames (b)-(e) ratios of integrated 50 meV regions are compared versus photon energy (eV) with a few representative error bars shown. The scaling amounts for each curve are shown parenthetically in the graph legends. The red closed circles in each frame (b)-(d) do not plateau to a constant as a function of energy, indicating that the integration windows compared contain contributions from different electronic states. The electronic origins were determined by analyzing the integration ratios which did not plateau at higher photon energies. In frame (e), all of the ratios exhibited Franck-Condon behavior at high energy. The arrows in frames (d)-(e) indicate a data point lies above the region shown.

not. The value by which each ratio was multiplied is shown in parenthesis next to the legend entry.

Bravaya, et al. also calculated the photoelectron spectrum for the first electronic state of thymine.[13] The vibrational contributions in the calculated spectrum are based on the vibrational progressions determined from VUV-MATI experiments.[31] The largest peak in the calculated spectrum comes from ν_8 and ν_{14}, which are combination bending stretching modes described by Bravaya, et al.[13] The bandshape in the calculated spectrum was determined using Lorentzian peaks with half widths at half maximums of 0.05 eV and maximum intensities set to the calculated Franck-Condon factors for each vibrational peak. Figure 5.6 shows a comparison of the experimental thymine photoelectron spectrum taken at photon energy 25 eV with the calculated photoelectron spectrum from Bravaya, et al.[13]

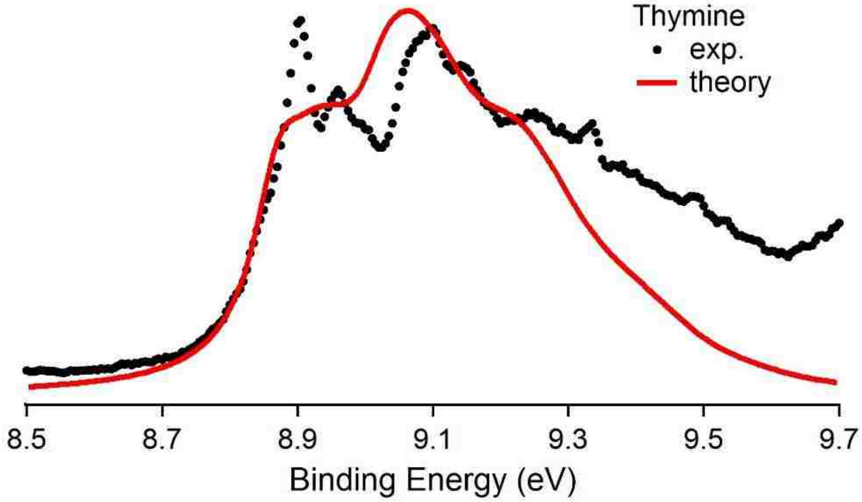

Figure 5.6. The calculated photoelectron spectrum for the first electronic state of thymine from Bravaya, et al. is compared with the present experimental thymine spectrum taken at photon energy 25 eV.[13]

The present experimental photoelectron spectrum of thymine agrees qualitatively with the calculated spectrum.

5.3.2. Uracil Results

Much like thymine, uracil exists in only the diketo form in the gas phase under the experimental conditions used; therefore, the pseudo-Franck-Condon analysis described above is also appropriate for the determining the electronic structure of uracil. The sharpest partially-resolved vibrational structure in the uracil data had an average fwhm of 49 meV. For the analysis, the uracil spectrum was divided into 50 meV integration windows, and the ratios of these windows were used to determine the binding energies of each of the four outermost valence electronic states. The uracil photoelectron spectrum taken at a photon energy of 19 eV is shown in Figure 5.7(a), with the following 50 meV integration windows highlighted in grey: 2, 14, 26, and 36. Figure 5.7 also shows the ratios of selected 50 meV integration windows. The ratios of integration windows shown in Figure 5.7(b)-(e) were scaled to emphasize the difference between the ratios which plateau to a constant value and those which do not. The value by which each ratio was multiplied is shown in parenthesis next to the legend entry.

5.3.3. Cytosine Results

It is known that in the temperature range over which cytosine data was collected, five tautomers/rotamers may be populated in the gas phase: keto-amino (denoted C1), enol-amino *cis* (C2a), enol-amino *trans* (C2b), keto-imino *cis* (C3a) and keto-imino *trans* (C3b), as shown in Figure 5.8.[12,17]

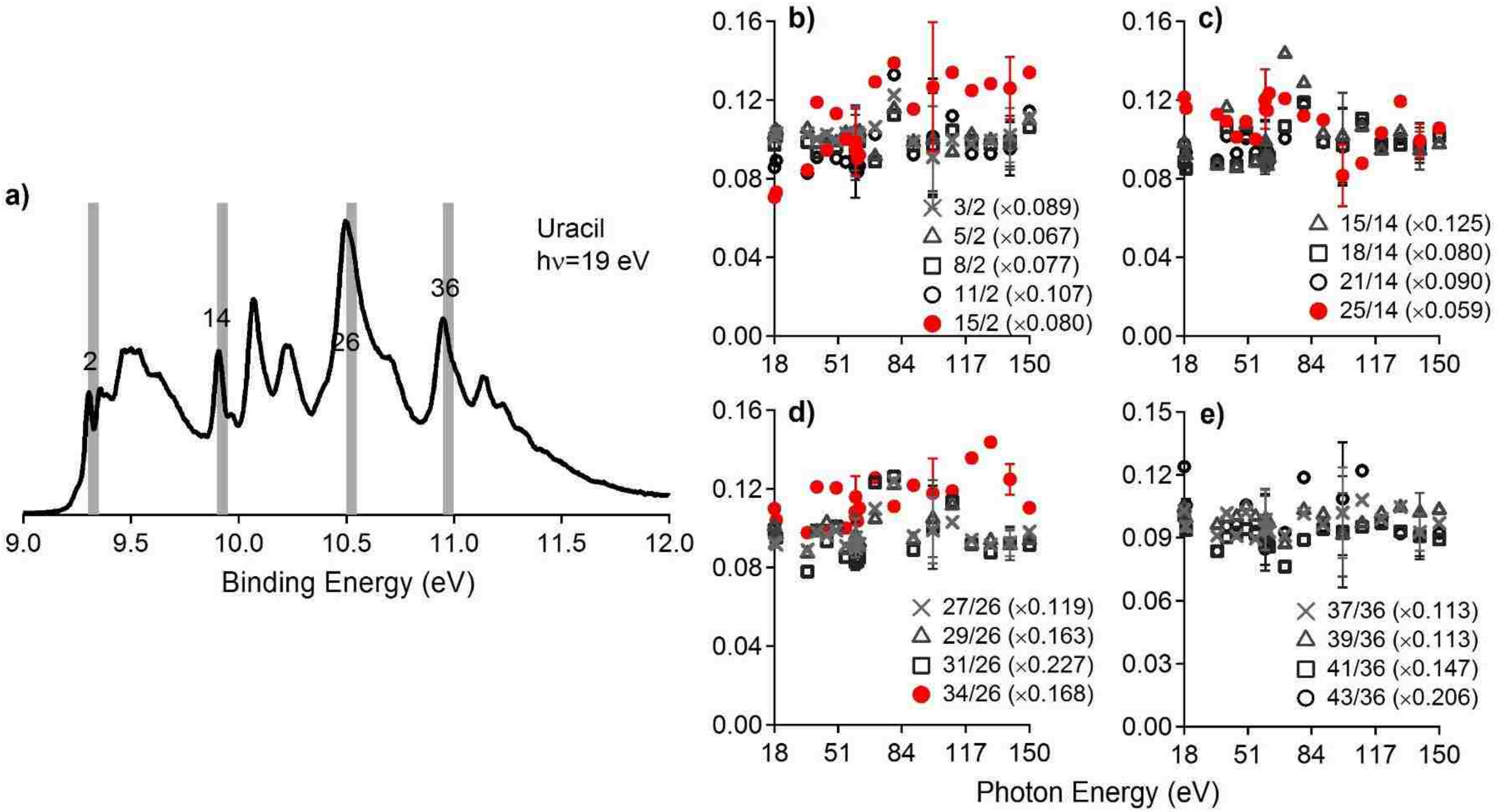

Figure 5.7. (a) The photoelectron spectrum of uracil taken at photon energy 19 eV is shown with the following 50 meV integration regions highlighted - regions 2, 14, 26 and 36. In frames (b)-(e) ratios of integrated 50 meV regions are compared versus photon energy (eV) with a few representative error bars shown. The scaling amounts for each curve are shown parenthetically in the graph legends. The red closed circles in each frame (b)-(d) do not plateau to a constant as a function of energy. In frame (e), all of the ratios exhibited Franck-Condon behavior at high energy.

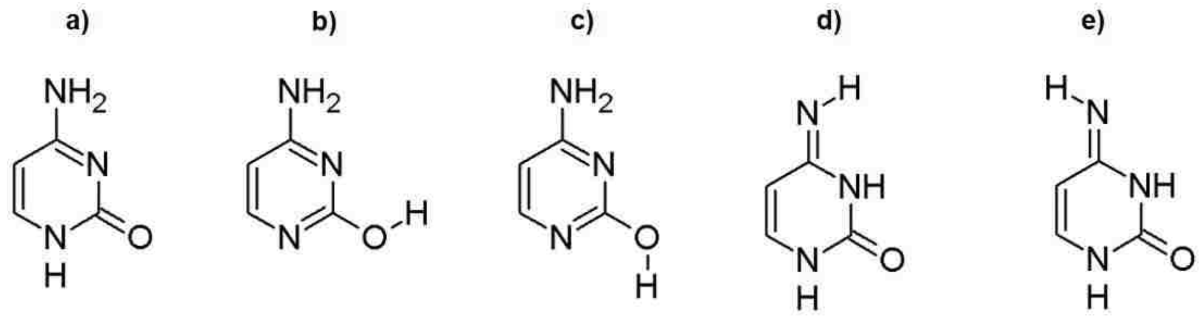

Figure 5.8. The structures of the following cytosine tautomers are shown: (a) keto-amino (C1), (b) enol-amino *cis* (C2a), (c) enol-amino *trans* (C2b), (d) keto-imino *cis* (C3a), and (e) keto-imino *trans* (C3b).

Recently, Farrokhpour, et al. calculated the photoelectron spectra of the first five valence electronic states of the cytosine tautomers C1, C2b and C3a/b.[32] Much like in the calculations from Trofimov, et al., Farrokphour, et al. did not distinguish between the two cytosine C3 rotamers in their calculations.[8,32] The rotamers C2a and C2b, as well as C3a and C3b, have energy differences less than 20 meV; thus, several papers have been published outlining calculations for only the lower energy rotamer in each pair, C2b and C3a.[18] In Figure 5.9, the calculated photoelectron spectra for C1, C2b and C3a/b from Farrokhpour, et al. are shown overlaid with the present experimental spectrum of cytosine collected at photon energy 23 eV.[32] The theoretical spectra are presented both as stick spectra as well as the sums of equally weighted Gaussians with full widths at half maximums of 250 meV. The implications of the comparison shown in Figure 5.9 will be further explored in Section 5.4.3.

In 2010, Bravaya, et al. calculated the photoelectron spectra over the binding energy range of the first electronic state for each low energy cytosine tautomer by using the equation of motion coupled cluster method in combination with the

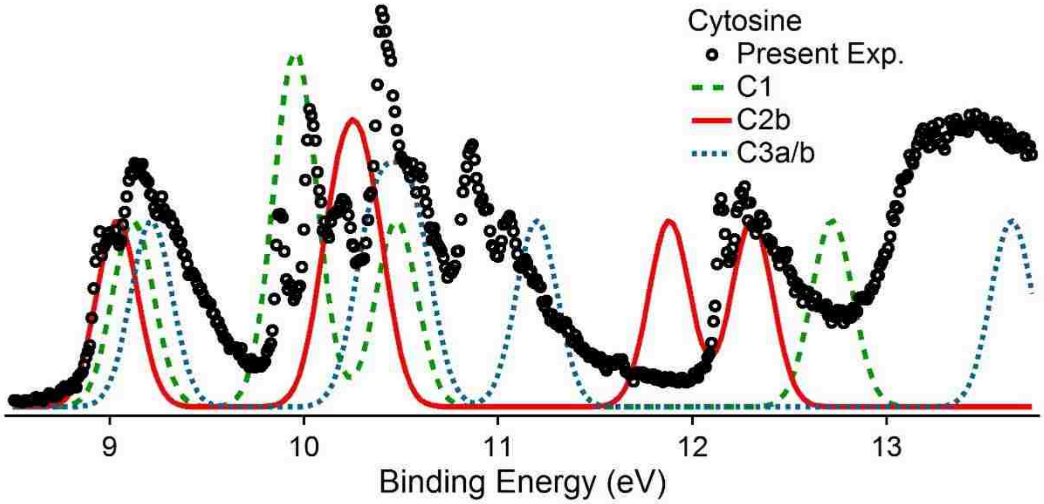

Figure 5.9. The experimental cytosine spectrum from the present work taken at photon energy 23 eV (black circles) was compared with calculated spectra for C1 (green dashed line), C2b (red solid line), and C3a/b (blue dotted line) from Farrokhpour, et al.[32] All calculated data are shifted 550 meV toward lower binding energy. No single calculated spectra matches to the present experimental data.

ezSpectrum software package.[13,33] The present experimental photoelectron spectrum collected at photon energy 23 eV is shown overlaid with the calculated photoelectron spectra for the first electronic states of C1, C2a, C2b, C3a and C3b from Bravaya, et al. in Figure 5.10.[13] The calculated spectra are shifted in binding energy approximately 30 meV; therefore, the binding energy scale for the experimental data is shown on the top axis, while the binding energy scale for the calculated spectra is shown on the bottom axis. The implications of this comparison will be examined in the Section 5.4.3.

Due to the stark similarities in the partially resolved structure of the cytosine, uracil, and thymine photoelectron spectra, it is likely that only one dominant cytosine tautomer contributes to the spectrum (this observation will be discussed further in Section 5.4). Under this assumption, a pseudo-Franck-Condon analysis was also

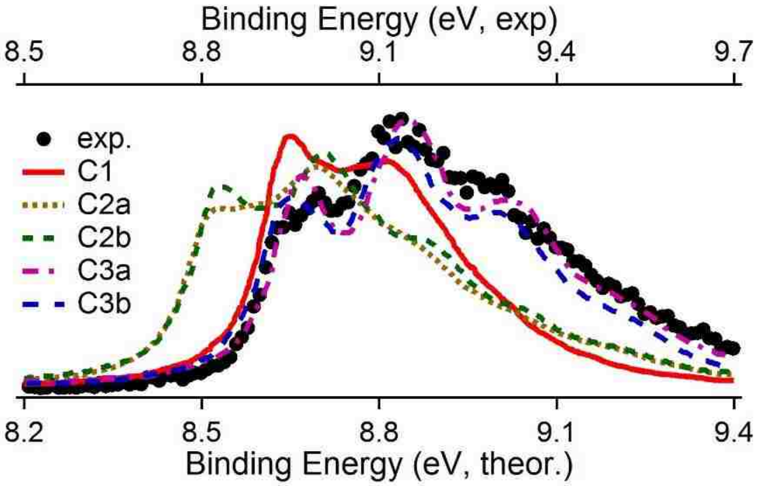

Figure 5.10. The experimental photoelectron spectrum of cytosine (black circles) taken with photon energy 35 eV is compared with the calculated spectra of the first electronic states of each low energy tautomer of cytosine from Bravaya, et al.:[13] C1 (red solid line), C2a (gold dotted line), C2b (green dashed line), C3a (purple dash-dotted line), and C3b (blue wide dashed line). The binding energy scale for the experimental data is shown along the top axis, and the binding energy scale for the calculated spectra is shown along the bottom axis. The intensities of the theoretical and experimental spectra have been scaled for comparison. There is qualitative agreement in particular between the calculated spectral envelope for C3a and C3b with the experimental spectral envelope.

performed on cytosine to determine the origins of the electronic states. Since the sharpest partially resolved vibrational structure in the cytosine data had an average fwhm of 76 meV, the spectrum was divided into 50 meV integration windows. The ratios of these integration windows are shown in Figure 5.11(b)-(e). The integration ratios were scaled for better comparison; the scaling factors are shown parenthetically in the legends of the individual frames. Figure 5.11(a) also shows the photoelectron spectrum of cytosine taken at a photon energy of 25 eV with the following integration windows highlighted in grey: 1, 20, 31, and 40.

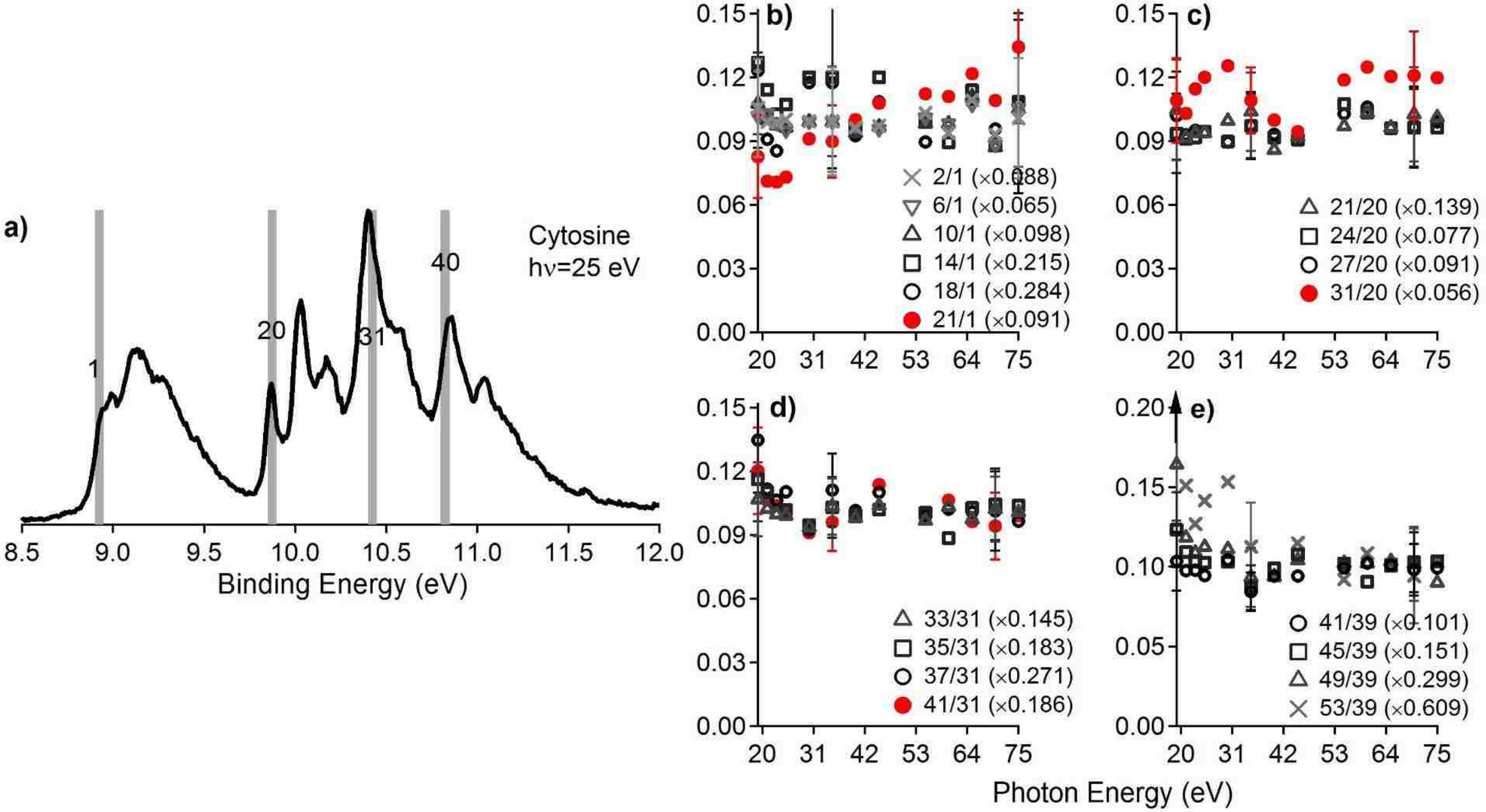

Figure 5.11. (a) The photoelectron spectrum of cytosine taken at photon energy 25 eV is shown with the following 50 meV integration regions highlighted - regions 1, 20, 31 and 40. In frames (b)-(e) ratios of integrated 50 meV regions are compared versus photon energy (eV) with a few representative error bars shown. The scaling amounts for each curve are shown parenthetically in the graph legends. The red closed circles in each frame (b)-(d) do not plateau to a constant as a function of energy. In frame (e), all of the ratios exhibited Franck-Condon behavior at high energy. The arrow in frames (e) indicates a data point lies above the region shown.

5.4 DISCUSSION

The resolution improvement in the photoelectron spectra presented in this dissertation compared to those obtained previously allowed for better comparison between experimental results and theory in order to draw important conclusions about the electronic structure of each of the nucleobases, thymine, uracil, and cytosine, as well as the tautomerism of cytosine. As shown in Figure 5.2, the spectral envelopes from the three pyrimidine-type nucleobases are strikingly similar. The almost identical features in the spectra indicate that these features arise from unresolved vibrational progressions and, therefore, are not contributions from various tautomers in the case of cytosine. Similarities in the shapes of all features in the spectral envelopes also indicate that the dominant vibrational progressions are coming from the pyrimidine backbone in each of these molecules, since all three systems share these vibrational modes.

5.4.1. Discussion of Thymine Results

Information about the locations of electronic states in the photoelectron spectra of thymine can be obtained by analyzing the ratios of integrated windows because only one conformer is present under the experimental conditions. The thymine spectra were integrated using 50 meV and 100 meV integrations windows. The highlighted 50 meV integration windows for thymine in Figure 5.5(a) mark the four different electronic regions visible in the thymine spectrum. If two channels belong to the same electronic state, then the ratio of their peak intensities should be independent of photon energy, even over a broad range. Thus, by analyzing the ratio of integrated windows with respect to the photon energy, the origins of the various electronic states can be roughly determined. As indicated previously, this observation is important because the electronic states are close-lying and even overlapping; therefore, the unambiguous identification and origin determinations have not been reported previously.

By comparing the integration windows of the thymine photoelectron spectra shown in Figure 5.5, conclusions can be drawn based on the photon energy dependence of the ratios. These integration windows are compared starting with the integration window containing the first peak of an electronic state compared with the first integration window of the region until the ratios no longer appear constant with photon energy. At that point, all the remaining integration windows are compared with the first integration window, which did not have a constant ratio with the integration window containing the start of the previous electronic region. The integration window ratios shown in Figure 5.5 were scaled to emphasize the difference between integrations window from the same electronic states and from different electronic states. As seen in Figure 5.5(b), integration window 6 marks the start of the first electronic region. The ratios of integration windows 21, 17, 13, and 9 to window 6 are constant with energy; however, the ratio of integration window 25 to window 6 is far from constant, even at very high photon energies, where resonance effects are expected to be absent. The ratio of these two windows not reaching a constant value indicates that region 25 is the onset of a new electronic state. This observation is not surprising, as inspection of Figure 5.5(a) shows that integration windows 6 and 25 are clearly from different electronic states of thymine. However, in the region of the thymine spectrum from binding energy 9.8 to 11.8 eV, it is much less clear where each new electronic state should begin. According to theoretical results by Trofimov, et al. using the ADC(3) method and the outer valence green’s function method, the region between binding energy 9.8 to 11.8 eV of the thymine spectrum should contain three electronic states:$\sigma_{LP\ O}$, π_5 and $\sigma_{LP\ O}$.[8] Shown in Figure 5.5(c) are the ratios between 50 meV integration windows 35 and 25, windows 32 and 25, windows 29 and 25, and windows 26 and 25. The ratios between integration windows 32, 29, and 26 with window 25 are relatively constant with photon energy. On the contrary, the ratio of integration windows 35 and 25 is far from being constant with photon energy, indicating these regions contain contributions from different electronic states. In Figure 5.5(d), the ratios of integration windows 45, 41, 29, and 36 with window 35 are compared. All of the ratios shown in Figure 5.5 (d) vary at low photon energies, and, with the exception of the ratio between windows 45 and 35, all the ratios seem to plateau to a constant ratio as the photon energy is increased. However, the ratio between integration regions 45 and 35 is not constant at higher photon energies, indicating that region 45 has contributions from a new electronic state. The ratios of windows 57, 53, and 49 to window 44 are compared in Figure 5.5(e). All three of these ratios display low energy oscillations and then plateau to a constant value at higher photon energies.

The variations in branching ratios observed near threshold are likely due to shape resonances. These variations will be discussed in more detail in Chapter 6: Low-Energy Shape Resonances in the Pyrimidine-Type Nucleobases.

For thymine, integration windows 6, 25, 35, and 44 seem to mark the start of the four electronic states in the region of interest. These integration windows correspond to binding energies of approximately 8.9, 9.8, 10.3, and 10.8 eV, respectively. Table 5.1 summarizes the thymine valence electronic state binding energies from the analysis.

Table 5.1. The results of the thymine pseudo Franck-Condon analysis. The integration window number from the pseudo Franck-Condon analysis, the binding energy in eV, and the molecular orbital assignment determined using angle-resolved photoelectron spectroscopy and calculations by Trofimov, et al.[8] are shown for each of the first four valence electronic states of thymine.

Integration Windows	Binding energy (eV)	Molecular Obital[8]
6-24	8.8	π_6
25-34	9.8	$\sigma_{LP\ O}$
35-44	10.3	π_5
44-63	10.8	$\sigma_{LP\ O}$

5.4.2. Discussion of Uracil Results

Uracil differs from thymine structurally by only a methyl group, as is seen in Figure 5.4. Consequently, the photoelectron spectra for uracil and thymine are notably similar, differing mostly in the first ionization energy and the spacing between the first and second electronic regions, as shown in Figure 5.2. It is, therefore, logical to assume the electronic structure of uracil is similar to that of thymine and that uracil’s valence electronic states in the region studied here can be defined from knowing the thymine valence electronic states. In thymine, integration windows 30, 20, 15 and 10 seem to mark the start of the four electronic states in the region of interest; these integration windows correspond to binding energies of approximately 8.8, 9.8, 10.3 and 10.8 eV, respectively. By comparing the shapes of the electronic states in thymine with the uracil spectrum, the four most outer valence electronic states of uracil would appear to begin at approximately 9.3, 9.9 10.5 and 10.95 eV.

From the pseudo-Franck-Condon analysis performed on uracil, which is shown in Figure 5.7, similar conclusions can be drawn. In Figure 5.7(b), the ratios of integration windows 3, 5, 8, 11, and 15 with window 2 are all relatively constant as a function of photon energy, while the ratio of integration window 15 to window 2 is not constant but increasing as a function of photon energy. Therefore, it can be concluded that integration windows 15 and 2 have contributions from different electronic states. Figure 5.7(c) shows the comparison of integration windows 15, 18, 21, and 25, each divided by integration window 14. The ratios of integration windows 15, 18, and 21 with window 14 all show a peak centered around 70 eV and then seem to flatten out to a constant value. However, the ratio of integrations windows 25 to 14 appear to oscillate over the entire photon energy range studied, never reaching a plateau. It is then reasonable to conclude that integration regions 14 and 25 likely contain contributions from different electronic states. In Figure 5.7(d), much like in (c) the ratios of regions 27, 29, and 31, as compared with region 26, all show some structure around 70 eV and then plateau to constant values. The ratio of integration windows 34 and 26, however, continues to have structure even at very high photon energies, indicating that windows 34 and 26 include contributions from different electronic states. Figure 5.8(e) shows the ratios of windows 37, 39, 41, and 43 with window 36; all of these ratios are relatively constant as functions of photon energy, indicating they are all from the same electronic state. Based on both the analysis of the integration windows and comparison of the uracil spectrum with that of thymine, it appears that integrations windows 2, 14, 26, and 36 mark the beginnings of the four outermost valence electronic states. The uracil results are summarized in Table 5.2, with molecular orbital assignments from angle-resolved photoelectron spectroscopy studies paired with calculations all from the work of Holland, et al.[10]

Table 5.2. The results of the uracil pseudo Franck-Condon analysis. The integration window number from this analysis, the binding energy in eV, and the molecular orbital assignment determined using angle-resolved photoelectron spectroscopy and calculations by Holland, et al.[10] are shown for each of the first four valence electronic states of uracil.

Integration Windows	Binding energy (eV)	Molecular Obital[8]
2-13	9.3	π_5
14-24	9.9	$\sigma_{LP\ O}$
26-34	10.5	π_4
36-63	10.95	$\sigma_{LP\ O}$

5.4.3. Discussion of Cytosine Results

The photoelectron spectra of the three pyrimidine-type nucleobases show strong similarities in their spectral features with the main difference being the spacing between these features. A comparison of the three spectra was shown in Figure 5.2. Since the spectral envelope of cytosine shows such a strong resemblance to those of thymine and uracil, this likely means that a single dominant form of cytosine contributes to the spectra. In this case, any contributions from other tautomers would be weak and mostly masked by the spectrum of the dominant tautomer. Comparing the present experimental data with the theoretical calculations from Bravaya, et al.[13] and Farrokhpour, et al.,[32] under the assumptions that only one tautomeric form is contributing to the spectrum, there is no clear answer as to which of the cytosine tautomers is the dominant contributor. From Farrokhpour's calculations, shown in Figure 5.9, the only two tautomers which have three electronic states calculated to be within the binding energy range 9.9 to 10.85 eV are actually C1 and C3a/b, not C2b, which is generally predicted to be the most stable form of cytosine over the temperature range used in data acquisition.

While some theories have suggested that the C3a/b tautomer is present in this temperature range,[15,18,20] all theories suggest C2b is the most prevalent tautomer over this temperature range, and that C2b should have the largest contribution to the photoelectron spectrum. Some predicted cytosine tautomer ratios at temperatures within the range of temperatures used in this experiment are shown in Table 5.3. However, various experiments using cytosine have suggested conflicting results regarding the tautomers present in the gas phase. That is, the microwave spectrum published by Brown, et al, showed evidence of C1, C2b and C3a in the gas phase, with C2b being the dominant tautomer and C1 and C3a being similarly populated, at 568 K.[16] A 1988 Ar-matrix IR spectroscopy experiment suggested only the C1 and C2a/b tautomers exist in the gas phase.[21] However, a more recent Ar-matrix IR spectroscopy experiment reported contributions from the C1, C2a, C2b and C3a tautomers of cytosine.[15] Also, the threshold photoelectron photoion coincidence spectrum for cytosine contained contributions from all five low energy cytosine tautomers.[22] Laser ablation molecular beam Fourier transform microwave spectroscopy has recently shown that all five tautomers of cytosine are present in the gas phase, and the C2a/b rotamers are the most abundant.[12]

Additionally, a core photoemission study showed that C2b, C1, C3a/b all existed in the gas phase.[17]

Table 5.3. A summary of the previously reported gas-phase tautomeric ratios for C1, C2a, C2b, C3a, and C3b which have been previously reported. These cytosine tautomeric ratios come from various calculations, as well as an IR experiment.

Study:	C1	C2a	C2b	C3a	C3b
Bazso, et al.[15] (CCSD) @ 450 K	0.29	0.17	0.37	0.17	…
Bazso, et al.[15] (IR, Ar-matrix)	0.22	0.26	0.44	0.08	…
Wolken, et al.[23] (CCSD) @ 473 K	0.24	0.22	0.47	0.01	0.06
Yang & Rodgers[24] (MP2) @ 490 K	0.20	0.24	0.51	0.05	0.01
Kosenkov, et al.[19] (CCSD) @ 490 K	0.42	…	0.57	0.01	…
Kostko, et al.[20] (CCSD) @ 582 K	0.24	0.20	0.35	0.16	0.05
Fogarasi[18] (CCSD/MP2) @ 470 K	0.22	0.17	0.37	0.24	…

Most theory has predicted 3a and 3b to be the least prevalent of the five lowest energy cytosine tautomers in the temperature range over which this data was collected.[15,18-20,23,24] Solid state cytosine exists only in the keto-amino form; however tautomerization occurs during the phase transition from the solid state to the gas state. Recently, several researchers have suggested cytosine initially forms dimers either upon or just before sublimation due to the amount of initial hydrogen bonding in the solid sample. This initial formation of dimers lowers the energy required for tautomerization.[19,24] Yang and Rodgers suggest this larger than predicted population of the C3b tautomer may be due to the formation of dimers in the solid state, which undergo bimolecular tautomerization prior to sublimation.

Then, upon sublimation the dimers may break apart into their respective tautomers.[24] This mechanism, suggested by Yang and Rodgers, eliminates the necessity of the ratios of tautomers populated in the gas phase to always reflect the relative stabilities of individual tautomers. The present data indicates that while only one cytosine tautomer contributes significantly to the photoelectron spectrum, it may be one of the C3 rotamers. Thus, the data presented here appears to indirectly support the above mentioned mechanism in which the cytosine forms dimers before forming gas-phase monomers.

Even without knowing which tautomer is the dominant contributor to the cytosine photoelectron spectrum, the pseudo-Franck-Condon analysis is still valid since it is convincing that only one tautomer contributes to the spectrum. The results of this analysis were shown in Figure 5.11. From Figure 5.11(b), integration window 1 marks the start of the first electronic region. The ratios of integration windows 2, 6, 10, 14, and 18 to window 1 are constant with energy; however, the ratio of integration window 21 to window 1 appears to have positive linear behavior with photon energy, never reaching a constant value. The behavior of window 20 to 1 with photon energy is very similar to that of window 21 to 1. This similar behavior indicates that region 20 is the onset of a new electronic state. Shown in Figure 5.11(c) are the ratios between 50 meV integration windows 21, 24, 27, and 31 with window 20. The ratios between integration windows 21, 24, and 27 with window 20 are relatively constant with photon energy. On the contrary, the ratio of integration windows 31 and 20 is far from being constant with photon energy, indicating these regions contain contributions from different electronic states. In

Figure 5.11(d), the ratios of integrations windows 33, 35, 37, and 41 with window 31 are compared. All of the ratios shown in Figure 5.5 (d) vary at low photon energies, and all of the ratios seem to plateau to a constant ratio as the photon energy is increased. However, by comparing the spectral features of the three nucleobases, it is apparent that window 40 should mark the start of the fourth electronic state. The ratios of windows 41, 45, 49, and 53 to window 40 are compared in Figure 5.5(e). All four of these ratios display some low energy feature and then plateau to a constant value at higher photon energies. The results of the pseudo-Franck-Condon analysis combined with the comparison of the spectral similarities between thymine and cytosine were used to determine the electronic origins of the outermost valence electronic states of cytosine. A summary of these results is shown in Table 5.4.

Table 5.4. The results of the cytosine pseudo Franck-Condon analysis. The integration window number from the present analysis and the binding energy in eV are shown for each of the first four valence electronic states of cytosine. There is no molecular orbital assignment shown for these electronic states since there is still some ambiguity about which tautomer of cytosine dominates the experimental spectrum.

Integration Windows	Binding energy (eV)
1-19	8.9
20-30	9.9
31-39	10.4
40-63	10.85

5.5. SUMMARY

Using photon energy-dependent photoelectron spectroscopy with improved photoelectron energy resolution, the binding energies of the four outermost valence electronic states for pyrimidine-type nucleobases were found. For thymine, the binding energies are 8.8, 9.8, 10.3, and 10.8 eV. For uracil, the outermost valence electronic states begin at binding energies 9.3, 9.9, 10.5, and 10.95 eV. For cytosine, the binding energies are 8.9, 9.9, 10.4, and 10.85 eV. Also, upon heating the uracil sample, the relative intensities of the electronic states beginning at 10.85 and 12.4 eV appear to increase as well. These increases in intensity of the two higher electronic states are likely due to vibronic effects from heating the uracil sample.

Stark similarities in the spectral features of all three pyrimdine-type nucleobases led to the conclusions that the features in the cytosine photoelectron spectrum are not due to contributions from multiple tautomers but instead from unresolved vibrational progressions. Since these features are practically the same in the spectra for all three molecules, it is further concluded that the dominant vibrational progressions must be due to the pyrimidine back-bone, which all three molecules have in common.

From the pseudo-Franck-Condon analyses performed on the pyrimidine-type nucleobases data, there is evidence for low-energy shape resonances, particularly in the third and fourth excited electronic states of the thymine and cytosine data. These shape resonances will be discussed in further detail in Chapter 6: Low-Energy Shape Resonances in the Pyrimidine-Type Nucleobases.

5.6 REFERENCES

[1] J.D. Watson, F.H.C. Crick, Nature 171 (1953) 964.

[2] J.D. Watson, F.H. Crick, Nature 171 (1953) 737.

[3] R.E. Holmlin, P.J. Dandliker, J.K. Barton, Angew. Chem. Int. Ed. 36 (1997) 2714.

[4] A. Padva, P.R. LeBreton, R.J. Dinerstein, J.N.A. Ridyard, Biochem. Biophys. Res. Commun. 60 (1974) 1262.

[5] G. Lauer, W. Schafer, A. Schweig, Tetrahedron Lett. 16 (1975) 3939.

[6] D. Dougherty, K. Wittel, J. Meeks, S.P. McGlynn, J. Am. Chem. Soc. 98 (1976) 3815.

[7] D. Dougherty, E.S. Younathan, R. Voll, S. Abdulnur, S.P. McGlynn, J. Electron. Spectrosc. Relat. Phenom. 13 (1978) 379.

[8] A.B. Trofimov, J. Schirmer, V.B. Kobychev, A.W. Potts, D.M.P. Holland, L. Karlsson, J. Phys. B.: At. Mol. Opt. Phys. 39 (2006) 305.

[9] C. Yu, S. Peng, I. Akiyama, J. Lin, P.R. LeBreton, J. Am. Chem. Soc. 100 (1978) 2303.

[10] D.M.P. Holland, A.W. Potts, L. Karlsson, I.L. Zaytseva, A.B. Trofimov, J. Schirmer, Chem. Phys. 353 (2008) 47.

[11] W. Pong, C.S. Inouye, J. Appl. Phys. 47 (1976) 3444.

[12] J.L. Alonso, V. Vaquero, I. Pena, J.C. Lopez, S. Mata, W. Caminati, Angew. Chem. Int. Ed. 52 (2013) 2331.

[13] K. Bravaya, O. Kostko, S. Dolgikh, A. Landau, M. Ahmed, A. Krylov, J. Phys. Chem. A 114 (2010) 12305.

[14] H. Satzger, D. Townsend, A. Stolow, Chem. Phys. Lett. 430 (2006) 144.

[15] G. Bazso, G. Tarczay, G. Fogarasi, P. Szalay, Phys. Chem. Chem. Phys. 13 (2011) 6799.

[16] R.D. Brown, P.D. Godfrey, D. McNaughton, A.P. Pierlot, J. Am. Chem. Soc. 111 (1989) 2308.

[17] V. Feyer, O. Plekan, R. Richter, M. Coreno, G. Vall-llosera, K.C. Prince, A.B. Trofimov, I.L. Zaytseva, T.E. Moskovskaya, E.V. Gromov, J. Schirmer, J. Phys. Chem. A 113 (2009) 5736.

[18] G. Fogarasi, J. Phys. Chem. A 106 (2002) 1381.

[19] D. Kosenkov, Y. Kholod, L. Gorb, O. Shishkin, D.M. Hovorun, M. Mons, J. Leszczynski, J. Phys. Chem. B 113 (2009) 6140.

[20] O. Kostko, K. Bravaya, A. Krylov, M. Ahmed, Phys. Chem. Chem. Phys. 12 (2010) 2860.

[21] M. Szczesniak, K. Szczesniak, J.S. Kwiatkowski, K. KuBulat, W.B. Person, J. Am. Chem. Soc. 110 (1988) 8319.

[22] D. Touboul, F. Gaie-Levrel, G.A. Garcia, L. Nahon, L. Poisson, M. Schwell, M. Hochlaf, J. Chem. Phys. 138 (2013) 094203.

[23] J.K. Wolken, C. Yao, F. Turecek, M.J. Polce, C. Wesdemiotis, Int. J. Mass Spectrom. 267 (2007) 30.

[24] Z. Yang, M.T. Rodgers, Phys. Chem. Chem. Phys. 6 (2004) 2749.

[25] M. Kubota, T. Kobayashi, J. Electron. Spectrosc. Relat. Phenom. 82 (1996) 61.

[26] C.R. Brundle, D.W. Turner, Int. J. Mass Spectrom. Ion Phys. 2 (1969) 195.

[27] C.R. Brundle, D.W. Turner, Proc. R. Soc. London, Ser. A 307 (1968) 27.

[28] J.W. Rabalais, L. Karlsson, L.O. Werme, T. Bergmard, K. Siegbahn, J. Chem. Phys. 58 (1973) 3370.

[29] J.C. Lopez, M.I. Pena, M.E. Sanz, J.L. Alonso, J. Chem. Phys. 126 (2007) 191103.

[30] V. Vaquero, M.E. Sanz, J.C. Lopez, J.L. Alonso, J. Phys. Chem. A 111 (2007) 3443.

[31] K.-W. Choi, J.-H. Lee, K.K. Kim, J. Am. Chem. Soc. 127 (2005) 15674.

[32] H. Farrokhpour, M. Ghandehari, J. Phys. Chem. B 117 (2013) 6027.

[33] V.A. Mozhayskiy, A.I. Krylov, ezSpectrum, http://iopenshell.usc.edu/downloads/.

CHAPTER 6

LOW ENERGY SHAPE RESONANCES IN THE PYRIMIDINE-TYPE NUCLEOBASES

This chapter further discusses the results from Chapter 5, Photoelectron Spectra of the Pyrimidine-Type Nucleobases. From the pseudo-Franck-Condon analyses performed on thymine, uracil, and cytosine, which were shown in Chapter 5, the low-energy oscillations occurring in a few of the electronic states are further explored.

6.1 INTRODUCTION

As discussed in Chapter 5, the nucleobases are the fundamental building blocks of DNA and RNA.[1,2] DNA damage via UV radiation is a cause of mutagenesis and carcinogensis. Radiation damage to DNA often occurs via secondary electron processes, as opposed to from the initial radiation directly.[3] Secondary electrons, which are ejected due to photoionization by the initial radiation, can then travel down the strand through π-stacking[4,5] and become temporarily trapped by shape resonances of nearby nucleobases.[6] While the secondary electron is trapped in the quasibound state of a nucleobases molecule, a temporary anion is created, which can then lead to fragmentation of the nucleobases via dissociative electron attachment.[3,7] By this method of DNA damage, the most probably bond to break is the C-O bond between the sugar and the phosphate group, effectively cutting the backbone of the DNA strand.[8-10]

Several theory papers, which predict these low energy shape resonance in the nucleobases, have been published.[11-14] Also, low-energy electron transmission spectroscopy experiments have provided evidence for these low energy shape resonances in the nucleobases.[3,6] Three resonances, one of which is very wide, have been found for uracil; three resonances, one of which is very sharp, have been found for cytosine; and three resonances, one of which is very wide, have been found for thymine.[6,12] In another publication, uracil was calculated to have five shape resonances.[11] Thymine's and uracil's broad shape resonances are found at slightly higher energies, approximately 10 eV above the ionization energies.[12]

This chapter presents further evidence of these low-energy shape resonance in the pyrimidine-type nucleobases. The high-resolution photoelectron spectra, as shown in Chapter 5, are revisited and further analyzed here.

6.2 RESULTS

The photoelectron spectra for each pyrimidine-type nucleobases, thymine, uracil, and cytosine, were sliced into 50 meV wide windows, as described in Chapter 5. These 50 meV windows of the spectra were integrated, and the ratios of these integration regions were used to determine the location of the electronic bands. A detailed discussion of the methods and results of this analysis can be found in Chapter 5. This chapter takes another look at only the lower energy regions of these integration window branching ratios as functions of photon energy in eV. The thymine results will be shown first, followed by those of uracil and then the cytosine results.

6.2.1. Thymine Results

The thymine spectrum taken at a photon energy of 25 eV is shown in Figure 6.1(a) with the following integration windows highlighted, 6, 25, 35, and 44.

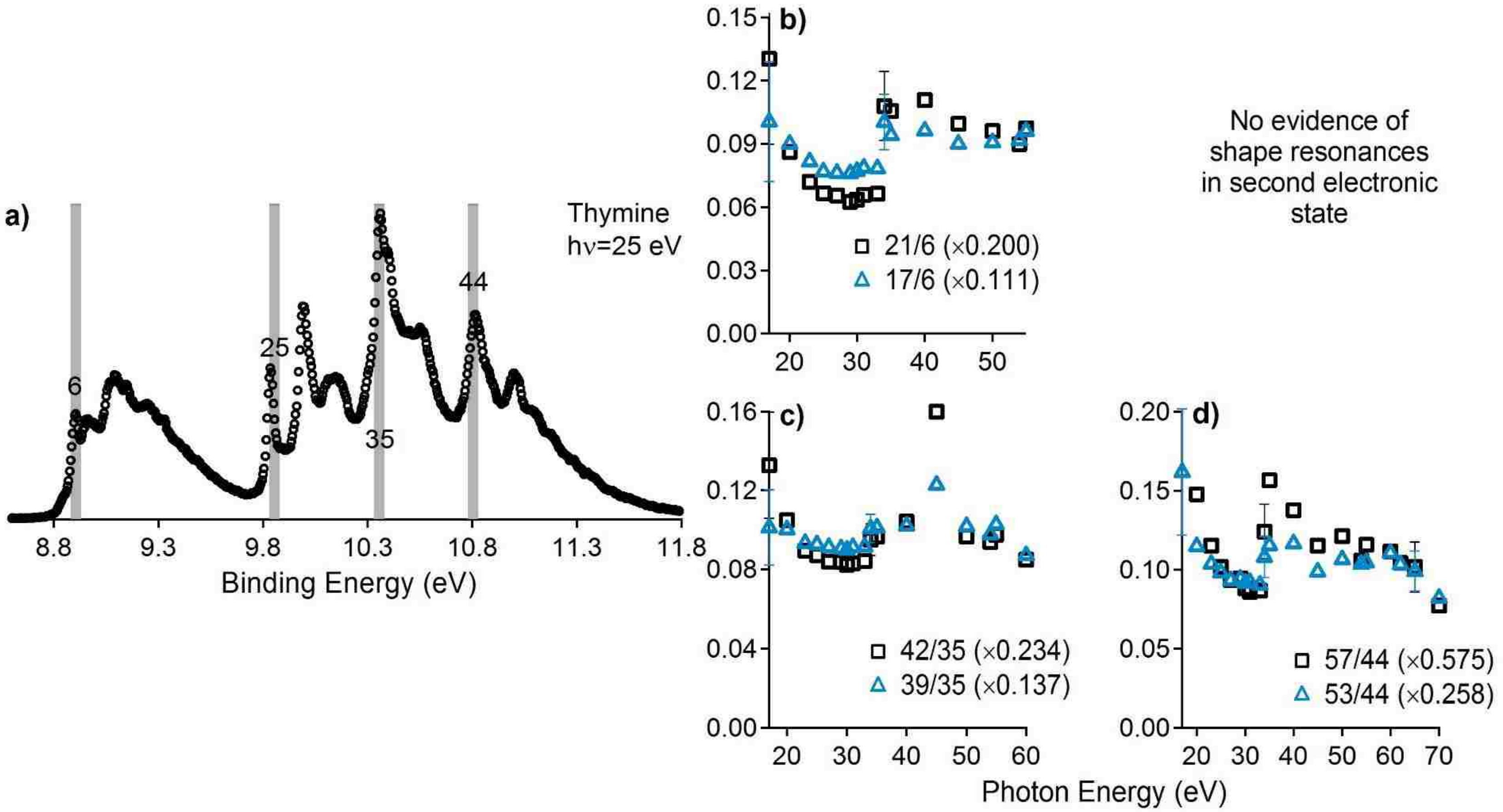

Figure 6.1. (a) The photoelectron spectrum of thymine taken at photon energy 25 eV is shown with the following 50 meV integration regions highlighted – regions 6, 25, 35, and 44. In frames (b)-(d) ratios of integrated 50 meV regions are compared as functions of photon energy (eV) with a few representative error bars shown. The scaling amounts for each curve are shown parenthetically in the graph legends. Features appeared just below 17 eV and around 40 eV for the first, third, and fourth electronic bands.

These selected integration regions represent the start of each electronic band in the spectrum, as was discussed in Chapter 5, Section 5.4.1. In Figure 6.1(b)-(d), select integration window branching ratios are shown for photoionization from the first, third, and fourth electronic states of thymine. The integration window branching ratios for the photoionization from the second electronic state of thymine did not show evidence for shape resonances. As such, the branching ratios resulting from photoionization from the second electronic state of thymine are neither shown nor discussed in this chapter. Representative branching ratios were selected to be shown in Figure 6.1(b)-(d) to reduce clutter in the graphs and allow for easier viewing. The ratios shown in Figure 6.1(b)-(d) are scaled for better comparison and shown over only a subset of the photon energy range at which data was collected.

6.2.2. Uracil Results

The uracil photoelectron spectrum taken at a photon energy of 19 eV is shown in Figure 6.2(a), with the following integration windows highlighted, 2, 14, 26, and 36. These selected integration regions represent the start of each electronic band in the spectrum, as was discussed in Chapter 5, Section 5.4.2. In Figure 6.2(b)-(c), select integration window branching ratios are shown for photoionization from the first and third electronic states of uracil. The integration window branching ratios for the photoionization from the second and fourth electronic states of uracil did not show evidence of shape resonances. As such, the branching ratios resulting from photoionization from the second and fourth electronic states of uracil are neither shown nor discussed in this chapter. Representative branching ratios were selected to be shown in Figure 6.2(b)-(c) to reduce clutter in the graphs and allow for easier viewing. The ratios presented in Figure 6.2(b)-(c) are scaled for better comparison and shown over only a subset of the photon energy range at which data was collected.

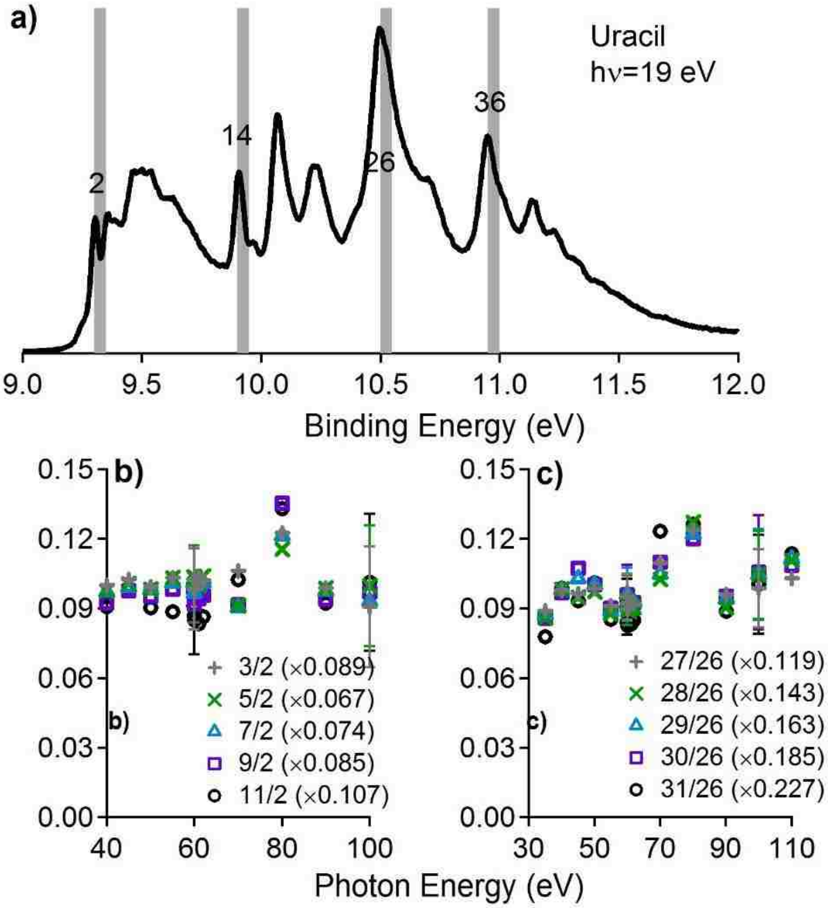

Figure 6.2. (a) The photoelectron spectrum of uracil taken at photon energy 19 eV is shown with the following 50 meV integration regions highlighted – regions 2, 14, 26, and 36. In frames (b)-(c) ratios of integrated 50 meV regions are compared as functions of photon energy (eV) with a few representative error bars shown. The scaling amounts for each curve are shown parenthetically in the graph legends. A feature appeared around 80 eV for photoionization from the first and third electronic states.

6.2.3. Cytosine Results

The cytosine spectrum taken at a photon energy of 25 eV is shown in Figure 6.3(a), with the following integration windows highlighted, 1, 20, 31, and 40.

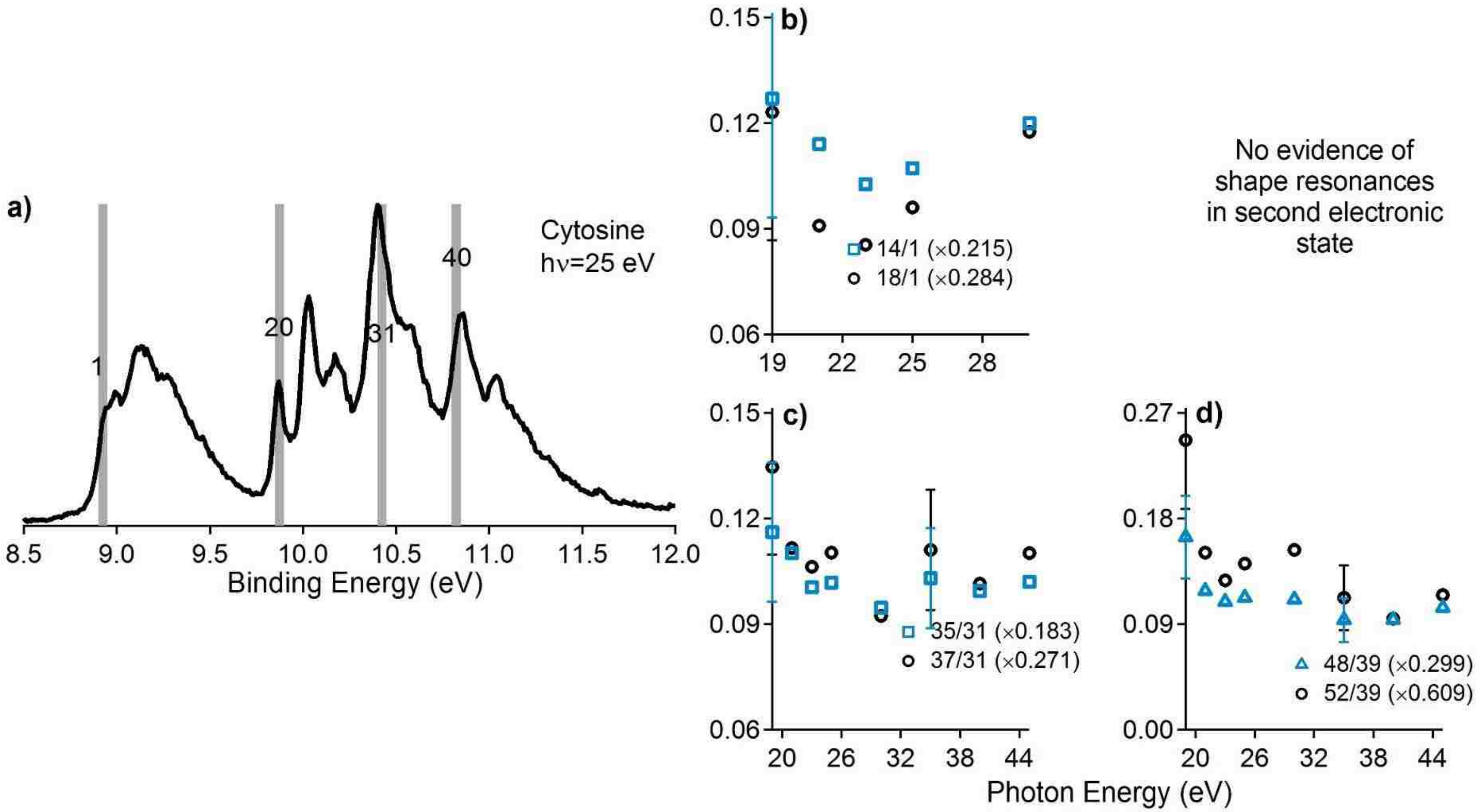

No evidence of shape resonances in second electronic state

Figure 6.3. (a) The photoelectron spectrum of cytosine taken at photon energy 25 eV is shown with the following 50 meV integration regions highlighted – regions 1, 20, 31, and 40. In frames (b)-(d) ratios of integrated 50 meV regions are compared as functions of photon energy (eV) with a few representative error bars shown. The scaling amounts for each curve are shown parenthetically in the graph legends. A feature appeared just below 19 eV for photoionization from the first, third, and fourth electronic states.

These selected integration regions represent the start of each electronic band in the spectrum, as was discussed in Chapter 5, Section 5.4.3. In Figure 6.3(b)-(d), select integration window branching ratios are shown for photoionization from the first, third, and fourth electronic states of cytosine. The integration window branching ratios for the photoionization from the second electronic state of cytosine did not show evidence for shape resonances. As such, the branching ratios resulting from photoionization from the second electronic state of thymine are neither shown nor discussed in this chapter. Representative branching ratios were selected to be shown in Figure 6.3(b)-(d) to reduce clutter in the graphs and allow for easier viewing. The ratios shown in Figure 6.3(b)-(d) are scaled for better comparison and shown over only a subset of the photon energy range at which data was collected.

6.3 DISCUSSION

As mentioned in Chapter 5, Section 5.3.1, using this pseudo-Franck-Condon analysis method on the nucleobases, it is expected that if the ratio for two integrations windows are overall constant valued then the two integrations windows belong to the same electronic state. The electronic bands were separated using this method, and this separation was explained in Chapter 5. However, even if the branching ratio between the two integration windows is relatively constant valued at high photon energies, the ratio may show oscillations at lower photon energies. These lower energy oscillations are evidence of non-Franck-Condon behaviors.

Shape resonances are a well-known cause of non-Franck-Condon behavior in molecules,[15-17] as was discussed in Chapter 1, Section 1.4.1. In actual vibrational branching ratios, shape resonances usually are reflected by peaks which span a few eV. As was mentioned in Section 6.1, there are already experimental and calculated evidences for the occurrence of shape resonances in thymine, uracil, and cytosine. In the following three Sections, the results of the present experiments will be discussed.

6.3.1. Discussion of Thymine Results

From Figure 6.1(b)-(d), ionization from the first, third, and fourth outermost valence electronic states of thymine appeared to have been affected by shape resonances, or some electron rescattering dynamics, in two photon energy regimes. The integration window branching ratios sloped down from photon energy 17 eV to somewhere around 25 eV; this slope was likely the second half or end of a low energy feature. Also, there was a broader peak occurring between photon energies 35 and 55 eV in the integrations window branching ratios shown in Figure 6.1(b)-(d). Currently, the only electron rescattering dynamics known to affect photoionization from the outermost valence electronic states of thymine are the shape resonancs predicted by theory and shown in electron transmission experiments. The thymine shape resonances detected by Aflatooni, et al. using electron transmission spectroscopy showed up between 0.29 and 4.05 eV of the ionization threshold,[6] while the resonances predicted by Tonzani, et al. occurred between 2.4 and 7.9 eV of the ionization threshold.[12] Based on the ionization energies of the four outermost valence electronic states of thymine, which were discussed in Chapter 5, the partial feature affecting the lowest energies of the integration window branching ratios for the first, third, and fourth electronic bands is likely a result of a shape resonance between the 4.05 and 7.9 eV predicted by experiment and theory. The broader feature, which occurred at a higher photon energy for all three electronic states, may be another shape resonance, or it may be due to some interference effects. No electron rescattering dynamics have been previously shown or predicted at this high of a photon energy range.

6.3.2. Discussion of Uracil Results

As depicted in Figure 6.2(b)-(c), photoionization from the second and fourth outermost valence electronic states of uracil may have been affected by electron rescattering dynamics around 80 eV. The only feature in the uracil data occurred at a much higher photon energy than the dynamics seen in thymine or in cytosine. The lack of a truly low energy feature in the uracil data is somewhat surprising due to the stark similarities in the electronic and physical structures of all the pyrimidine-type nucleobases. However, less data were collected for uracil and cytosine than were collected for thymine, so there were fewer data points in the uracil and cytosine integration window branching ratios than there were for thymine. The lower density of data points may make some features in the branching ratios less obvious. The shape resonances seen experimentally and predicted by theory occur much closer to the ionization threshold; therefore, this feature is not due to these known uracil shape resonances. The weak feature, which occurred near 80 eV in the integration window ratios for ionization from the second and fourth outermost valence electronic states of uracil, may have resulted from some other unknown resonant or nonresonant electron rescattering dynamics.

6.3.3. Discussion of Cytosine Results

Similar to the uracil results, as evident in Figure 6.3(b)-(d), ionization from the first, third, and fourth outermost valence electronic states of cytosine appeared to have been affected by some electron rescattering dynamics in only one photon energy regime. Unlike the uracil results, the photoionization from the first, third, and fourth outermost electronic states of cytosine showed evidence of a low-energy feature, which appeared to begin much below 19 eV and end around 25 eV. For cytosine 19 eV was the lowest photon energy at which a photoelectron spectrum was collected, as opposed to 17 eV for thymine and uracil. The downward slope from 19 to 25 eV in the cytosine integration window branching ratios shown in Figure 6.3(b)-(d) is convincingly real. The cytosine shape resonances detected by Aflatooni, et al. using electron transmission spectroscopy appeared between 0.32 and 4.50 eV of the ionization threshold,[6] while the resonances predicted by Tonzani, et al. occurred between 1.7 and 8.1 eV of the ionization threshold.[12] Based on the ionization energies of the four outermost valence electronic states of uracil, which were discussed in Chapter 5, the partial feature affecting the lowest energies of the integration window branching ratios for the first, third, and fourth electronic bands is likely a result of a shape resonance between the 4.5 and 8.1 eV predicted by experiment and theory.

6.4 SUMMARY

The first evidences of low energy shape resonances in the pyrimidine-type nucleobases, thymine and cytosine, from photoelectron spectroscopy have been presented. These high resolution photoelectron spectroscopy experiments also provided evidence of unknown electron rescattering dynamics, which led to non-Franck-Condon behavior at higher photon energies for thymine and uracil. Photoionization from the first, third, and fourth outermost valence electronic states of thymine showed a breakdown of the Franck-Condon principle below 17 eV, which is likely due to the previously reported shape resonances. The pseudo branching ratios for photoionization from the first, third, and fourth outermost valence electronic states of thymine also showed non-Franck-Condon behavior between 35 and 50 eV, an energy range at which no electron rescattering dynamics were previously known for these system. In uracil, photoionization from only the first and third outermost valence electronic states showed a weak feature centered around 80 eV and no evidence of any low energy shape resonances. Photoionization from the first, third, and fourth outermost valence electronic states of cytosine presented evidence of the previously reported shape resonances in a feature occurring below 19 eV. The thymine and cytosine results presented here are the first evidences of low energy shape resonances in the pyrimidine-type nucleobases shown using photoelectron spectroscopy.

6.5 REFERENCES

[1] J.D. Watson, F.H. Crick, Nature 171 (1953) 737.

[2] J.D. Watson, F.H.C. Crick, Nature 171 (1953) 964.

[3] B. Boudaiffa, P. Cloutier, D. Hunting, M.A. Huels, L. Sanche, Science 287 (2000) 1658.

[4] S.O. Kelley, J.K. Barton, Science 283 (1999) 375.

[5] R.E. Holmlin, P.J. Dandliker, J.K. Barton, Angew. Chem. Int. Ed. 36 (1997) 2714.

[6] K. Aflatooni, G.A. Gallup, P.D. Burrow, J. Phys. Chem. A 102 (1998) 6205.

[7] F. Martin, P.D. Burrow, Z. Cai, P. Cloutier, D. Hunting, L. Sanche, Phys. Rev. Lett. 92 (2004) 068101.

[8] A.M. Scheer, K. Aflatooni, G.A. Gallup, P.D. Burrow, Phys. Rev. Lett. 92 (2004) 068102.

[9] J. Simons, Acc. Chem. Res. 36 (2006) 772.

[10] R. Barrios, P. Skurski, J. Simons, J. Phys. Chem. B 106 (2002) 7991.

[11] F.A. Gianturco, R.R. Lucchese, J. Chem. Phys. 120 (2004) 7446.

[12] S. Tonzani, C.H. Greene, J. Chem. Phys. 124 (2006) 054312.

[13] C. Winstead, V. McKoy, S.d.A. Sanchez, J. Phys. Chem. A 127 (2007) 085105.

[14] C. Winstead, V. McKoy, J. Chem. Phys. 125 (2006) 244302.

[15] J.L. Dehmer, D. Dill, S. Wallace, Phys. Rev. Lett. 43 (1979) 1005.

[16] R. Stockbauer, B.E. Cole, D.L. Ederer, J.B. West, A.C. Parr, J.L. Dehmer, Phys. Rev. Lett. 43 (1979) 757.

[17] J.B. West, A.C. Parr, B.E. Cole, D.L. Ederer, R. Stockbauer, J.L. Dehmer, J. Phys. B.: At. Mol. Opt. Phys. 13 (1980) L105.

CHAPTER 7

HARMONICS NEAR ARGON COOPER MINIMUM RESIST DECAY WITH ADDED LASER ELLIPTICITY: A POTENTIAL HHG PROBE

This chapter presents evidence for using the ellipticity of the driving laser as a probe for electron rescattering events in the photorecombination step of high-order harmonic generation (HHG). Specifically, this chapter shows that the harmonics nearest to the argon (Ar) Cooper minimum behaved differently than the other harmonics generated in Ar with increasing laser ellipticity. Furthermore, the chapter will show that the harmonics generated in krypton (Kr), which is void of any resonances or Cooper minima over the energy range at which harmonics were generated, all behaved relatively the same, with increasing laser ellipticity. The Kr data further supports the idea that the anomalous behavior near the energy of the Cooper minimum in the Ar harmonics is indeed due to the presence of the Cooper minimum.

7.1 INTRODUCTION

Photoionization and photorecombination are essentially inverse processes. During photoionization a high energy photon enters the target, and an electron is ejected; similarly, during photorecombination, an electron enters the target, and a high energy photon is ejected.[1,2] Electron rescattering dynamics are known to affect both of these processes.[3,4] There are many well-known experimental probes of photoionization, such as photoelectron asymmetry, spin-polarization, branching ratios, etc.;[5] however, there are currently no well-established probes for this process. This chapter presents evidence for using the polarization of the driving laser as a probe for electron rescattering dynamics during HHG. Specifically, this chapter discusses HHG experiments, during which the driving laser polarization was varied, on the atomic targets Ar and Kr.

A photoelectron has a significant probability of recombining with its parent ion upon interaction with slightly elliptically polarized light, unlike with circularly polarized light. So, high-order harmonics can still be generated with elliptically polarized light. Typically in HHG studies, the electron is described as taking one of two possible pathways, either the long trajectory or the short trajectory,[6] leading to the same final kinetic energy of the returning electron. However, the long and short trajectories are defined for linearly polarized light. When ellipticity is added to the laser pulse, the two pathways that the electron can take within the laser pulse change slightly; this means that the electron will recombine with the parent ion at a different angle from the one at which the electron initially left the system. These new pathways may be ideal for probing electron rescattering dynamics occurring during photorecombination since shape resonances and Cooper minima have spatial properties within atoms and molecules. It has been previously reported that the short trajectory contributions to the harmonics are affected quite significantly by the ellipticity of the driving laser; however, the long trajectory contributions are hardly phased by the change in laser polarization.[7]

The Cooper minimum of Ar – a well-known effect in photoionization – has been shown to be manifested in several HHG experiments.[3,8,9] From photoionization experiments, the photon energy at which the Cooper minimum occurs is approximately 47.5 eV.[10-12] However, it has been reported in both experimental and theoretical HHG papers that this Cooper minimum can shift by a few eV in either direction in the HHG spectrum due to a number of parameters, including laser intensity, laser focus position within the gas jet, gas jet density, laser spot size, and fundamental laser wavelength.[9,13] In fact, the Ar Cooper minimum has been seen as high as 55 eV in HHG experiments.[8,9] The visibility of the Ar Cooper minimum in the high-order harmonic spectrum is also closely linked to the phase-matching.[14,15]Several other electron rescattering dynamics have been seen in high-order harmonic spectra, such as the Cooper minimum for Kr,[16,17] the Cooper minima for select chlorinated molecules[13], and the giant resonance in Xe.[17-19]

The idea of studying the effects of driving laser ellipticity on the HHG process is not novel; in fact, studies have already been published showing a decrease in HHG efficiency with increasing laser ellipticity.[7,20-26] The harmonic intensities, as a general rule, have been shown to decrease as a Gaussian with increasing laser ellipticity.[21,26] The Gaussian function suggested to model this harmonic behavior, which was shown in Chapter 1 as Equation 1.15, only depends on laser parameters and the ionization potential of the medium. Thus, the current model for high-order harmonic generation as a function of laser ellipticity does not account for any dependence on electron rescattering dynamics. Even though the current model does not account for any electron rescattering dynamics, another published study has shown that the effect of the Cooper minimum in Ar on the resulting generated harmonic is broadened by adding ellipticity to the driving laser. It has also been shown that harmonics generated from molecules are much less sensitive than harmonics generated from atoms.[22] This observation is evidence that the HHG processes differs slightly between atoms and molecules. Since molecules are likely to have more complex electron dynamics, such as resonant features, it is possible that these electron rescattering dynamics help to overcome the dependence on the laser polarization. Furthermore, two different studies concluded that the ellipticity dependence of molecular harmonics is also sensitive to the shape and symmetry of the valence orbitals.[25,26] These studies all provided evidence that the electron dynamics of the atomic or molecular medium are important to the HHG process, and that the ellipticity dependence of the harmonic intensities further depend on the electron dynamics of the atom or molecule.

This study showed that the harmonics nearest in energy to the Ar Cooper minimum did not behave exactly the same as the harmonics further from the Ar Cooper minimum. More specifically, the harmonics around the energy of the Ar Cooper minimum required more laser ellipticity to decay than did the other harmonics. As a control, the same study was performed with Kr, which does not contain a Cooper minimum or any other known electron rescattering “structure” in the energy range studied.

7.2 ADDITIONAL EXPERIMENTAL DETAILS

The data presented in this chapter were taken using both the HITS and KLS laser systems, which were described in Chapter 2, Sections 2.5.1 and 2.5.2. The HITS data presented for both Ar and Kr were taken using a continuously flowing effusive jet from the end of a capillary. For all of the KLS data presented here, a pulsed supersonic jet was used to introduce the gas-phase medium. The Ar data collected with the KLS system were taken using a piezo pulsed valve operating a

250 Hz. The Kr data collected with the KLS system were taken using an Even-Lavie pulsed valve operating at 500 Hz. The shapes of the supersonic jets created by the piezo valve and the Even-Lavie valves were quite different. The piezo valve created a gas jet with a broad upside-down ‘V’ shape near the nozzle, while the Even-Lavie valve created a gas jet with a sharp upside-down ‘U’ shape near the nozzle. Thus, with the piezo valve, harmonics were generated over a much broader range of focal positions than with the Even-Lavie valve. This means the focal positions of data taken with each of the pulsed valves corresponded to different phase-matching conditions. Also, the KLS and HITS lasers most likely have different Rayleigh ranges. The Rayleigh range of a laser describes how the beam diverges after being focused;[27] this characteristic is closely related to the beam profile. When the radius of the focused beam at its narrowest point, the beam waist, increases by the square root of two, this broadened point marks the end of the Rayleigh range with the beginning being marked by the beam waist. Thus, the same laser focus position may have corresponded to different phase-matching conditions using different laser systems.

7.3 ADDITIONAL DATA ANALYSIS DETAILS

The spectrometer used with the HITS laser system uses a diffraction grating optimized for higher energy harmonics since it is meant to also be used with the TOPAS for longer wavelength HHG. However, it was noticed when collecting data generated with a fundamental frequency of 800 nm that there is some additional signal appearing on the detector with the HITS spectrometer. This additional signal may be the result of some scattering process on the diffraction grating. The scattering signal affected the region of the detector where harmonics 17 through 31 appeared. In order to correct for this additional signal, which does not decay with added laser ellipticity, additional pretreatment of the data was necessary. A schematic describing this pretreatment can be found in Figure 7.1. The additional pretreatment of the data was performed slice-wise on each image, with each horizontal slice being 20 pixels high. Correction slices were created based on the image taken at the highest laser ellipticity, 0.4, at which point all of the highest order harmonics had already decayed to zero. From the top and bottom slices of the image taken at a laser ellipticity of 0.4, the bounds of the region affected by the scattering signal were obtained. Then the correction slices were set to be zero outside of the region affected by the scatter and set to equal the signal in the highest ellipticity image for the scattering region. These correction slices were then subtracted slice-wise from every image taken at the same focusing condition and for the same atomic medium, so that only the harmonic signal remained in the corrected images. After correction, the HITS data was analyzed identically to the KLS data.

7.3 RESULTS

The argon results are shown first, followed by the krypton results. The contrasting behavior of the Kr data corroborate our interpretation of the Ar results; thus, both results are presented below.

7.3.1 Argon Results

Phase-matching is a complicated topic in high-order harmonic generation; however, it is understood that various phase-matching conditions can lead to a plethora of different high-order harmonic spectral envelopes.[28-30] Even with the

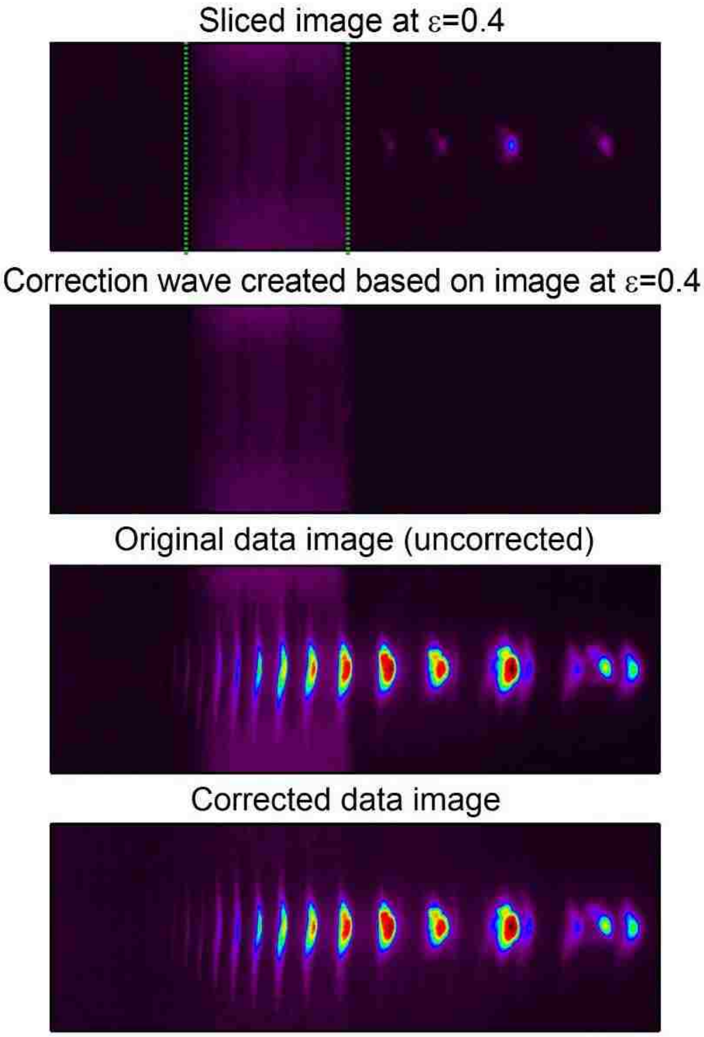

Sliced image at ε=0.4

Correction wave created based on image at ε=0.4

Original data image (uncorrected)

Corrected data image

Figure 7.1. A schematic showing the pretreatment of the data collected with the HITS spectrometer. The correction slices were created from the highest ellipticity data image collected since this image should have only a few of the lower order harmonics present. The correction area was identified, and for each slice of the correction wave every pixel outside of this area was set to zero. The correction wave was then subtracted from the original image to create the corrected image.

complex nature of phase-matching, when the harmonics are relatively phase-matched, it becomes possible to extract information about the atomic, or molecular, medium which was used to generate the harmonics. Since, as previously stated, photoionization and photorecombination (the final step of the HHG process) are inversely related, the harmonics should contain information about how the electron interacts with the molecule during photorecombination.

One evidence of the harmonics containing information about the electron rescattering dynamics was the visibility of the Ar Cooper minimum. It has also been previously noted that, while phase-matching is important for the overall shape of the spectral envelope and for the maximum harmonic visible, known as the cut-off harmonic, these electron rescattering features are actually visible over a fairly broad range of phase-matching conditions.[14,31] Thus, it is generally assumed that features in the harmonic spectrum, which occur over a broad range of phase-matching conditions, are due to the medium. A straight forward way to experimentally alter the phase-matching is to change the location of the laser focus within the gas jet. From data taken at a variety of laser focusing positions, the optimum phase-matching conditions can be approximated by overlaying the harmonic spectral envelopes with the photoionization cross sections and looking for both the best overall match, allowing for some shifting to occur, and for the most visible harmonics. Many groups have reported that for optimum phase-matching, the focus of the laser should be at the front end of the gas jet, so that the majority of the gas jet experiences a diverging beam.[28,32] Optimum phase-matching is typically defined, from an experimentalist perspective, as the conditions at which the largest number of harmonics are visible and the short trajectory contributions dominate the spectrum.[32] Figure 7.2 shows overlays of harmonic spectral envelopes at different laser focusing conditions with the absolute photoionization cross section for Ar measured by Marr and West in Mb.[12] These overlays are shown for data collected

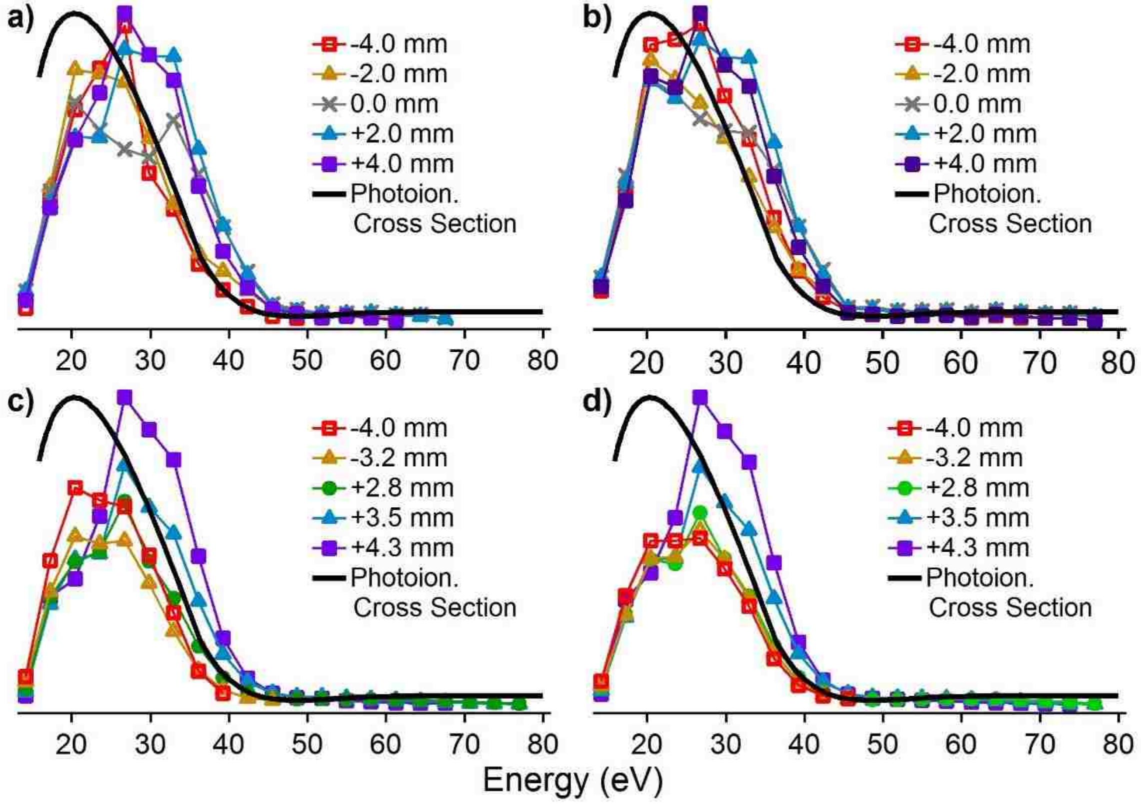

Figure 7.2. Comparison of the absolute photoionization cross section from Marr and West[12] for Ar with HHG spectral envelopes spanning several focusing conditions. The photoionization cross section is a function of photon energy, and the HHG spectral envelopes are functions of harmonic energy, both in eV. The intensity units here are arbitrary since all graphs were plotted for best comparison. In (a)-(b) HHG data were taken with the HITS laser system using a capillary for a sample inlet. The peak laser intensities were (a) 2.86x10^{14} W/cm^2 and (b) 3.95x10^{14} W/cm^2. In (c)-(d) HHG data were taken with the KLS laser system using a piezo pulsed valve operating at 250 Hz. The peak laser intensities were (c) 3.97x10^{14} W/cm^2 and (d) 5.10x10^{14} W/cm^2. For the data shown in (a)-(b), the best focusing positions were +2 and +4 mm, since these positions showed both the most harmonics and the best qualitative agreement with the photoionization cross section. Similarly, for the data shown in (c)-(d), the best focusing condition was +2.8 mm.

at two different laser intensities with the HITS laser, Figure 7.2 (a) and (b), and at two different laser intensities with the KLS laser, Figure 7.2 (c) and (d). Positive focus positions mean the laser was focused in front of the center of the gas jet; negative focus positions correspond to the laser having been focused behind the center of the gas jet. As seen in Figure 7.2, the laser focus positions corresponding to the best phase-matching conditions, under which data were collected, were taken to be +2 mm for the HITS laser and +2.8 mm for the KLS. These results will be discussed further in Section 7.4.1.

To analyze the effect of laser ellipticity on the individual harmonics, the spectral envelopes were all normalized to the spectral envelopes generated with linear light and all other parameters the same (i.e., the laser intensity and laser focusing conditions were kept constant). The normalized data for two different HITS laser intensities and three different focusing conditions, -2, 0 and +2 mm, are shown as contour plots in Figure 7.3. Harmonics 9 and 11 are below or at the Ar ionization threshold, where different physical behavior of the harmonics was expected. As such, harmonics 9 and 11 are not displayed in the contour plots of Figure 7.3. Below and at ionization threshold harmonics have been observed to increase initially with small amounts of added ellipticity previously.[33,34] The behavior of lower order harmonics will not be further discussed here as they were not the interest of this study. The harmonic contours shown are representative of the data taken at the other laser focus positions. With the color scale used in Figure 7.3, blue is a normalized intensity of one, and red is a normalized intensity of zero.

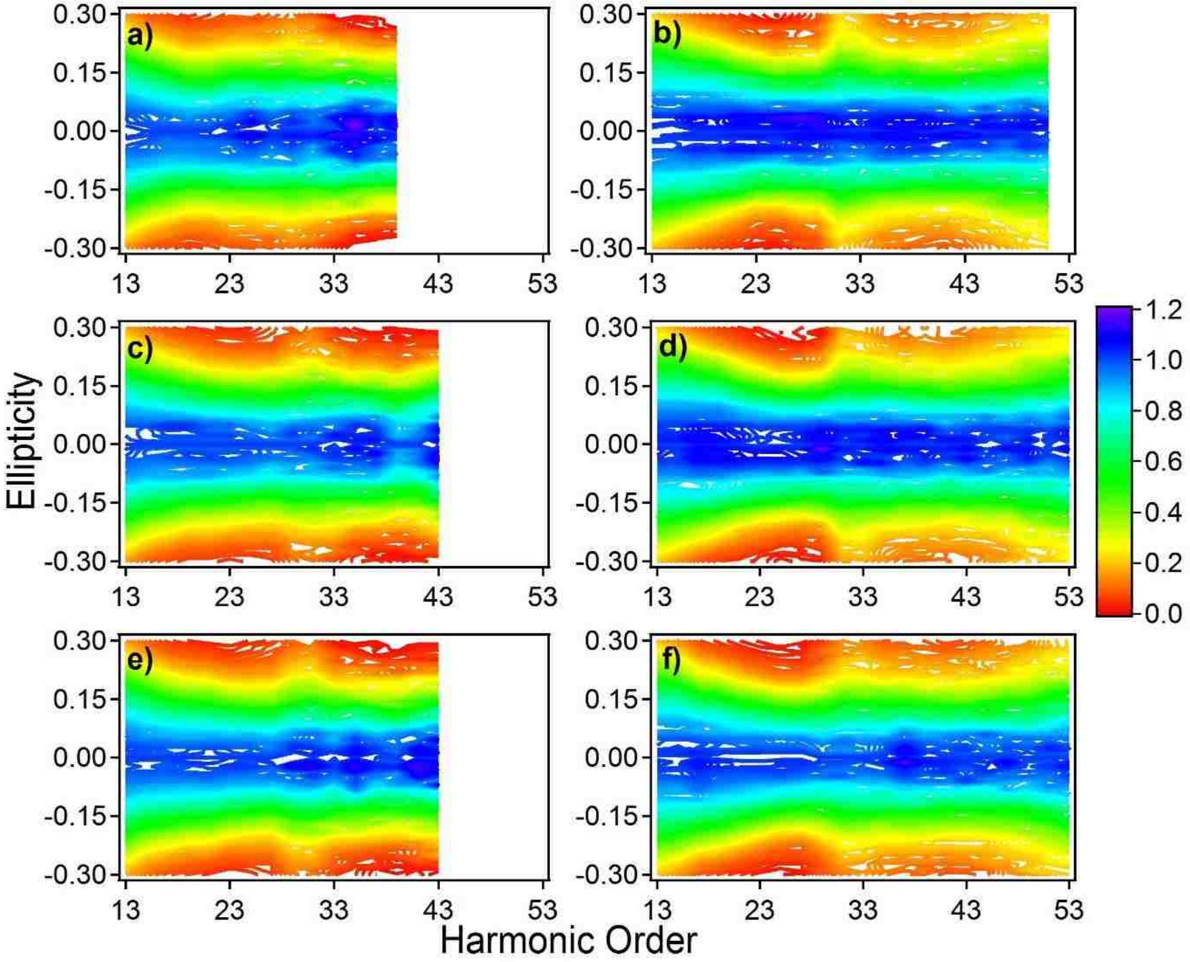

Figure 7.3. Contour plots of normalized Ar harmonic intensity as a function of laser ellipticity taken with the HITS laser system. The peak laser intensities were (a), (c), and (e) 2.86x10^{14} W/cm^2 and (b), (d), and (f) 3.95x10^{14} W/cm^2. The laser was focused (a)-(b) 2 mm behind the center of the gas jet, (c)-(d) at the center of the gas jet, and (e)-(f) 2 mm in front of the center of the gas jet. A feature occurred centered at the 29th – 31st harmonics at both intensities and multiple focusing conditions.

Figure 7.4 also shows the normalized contour plots of Ar harmonic intensity decaying with added ellipticity for data taken with the KLS system. Only one direction of laser ellipticity was studied with the KLS laser. However, there was a feature occurring centered at the 31st harmonic. This feature is similar to that in the contour plots from the HITS data, except that the KLS data feature was broader, and not as intense, meaning that the harmonics in the feature decayed to essentially zero at a lower ellipticity value than did the harmonics in the feature found in the HITS data.

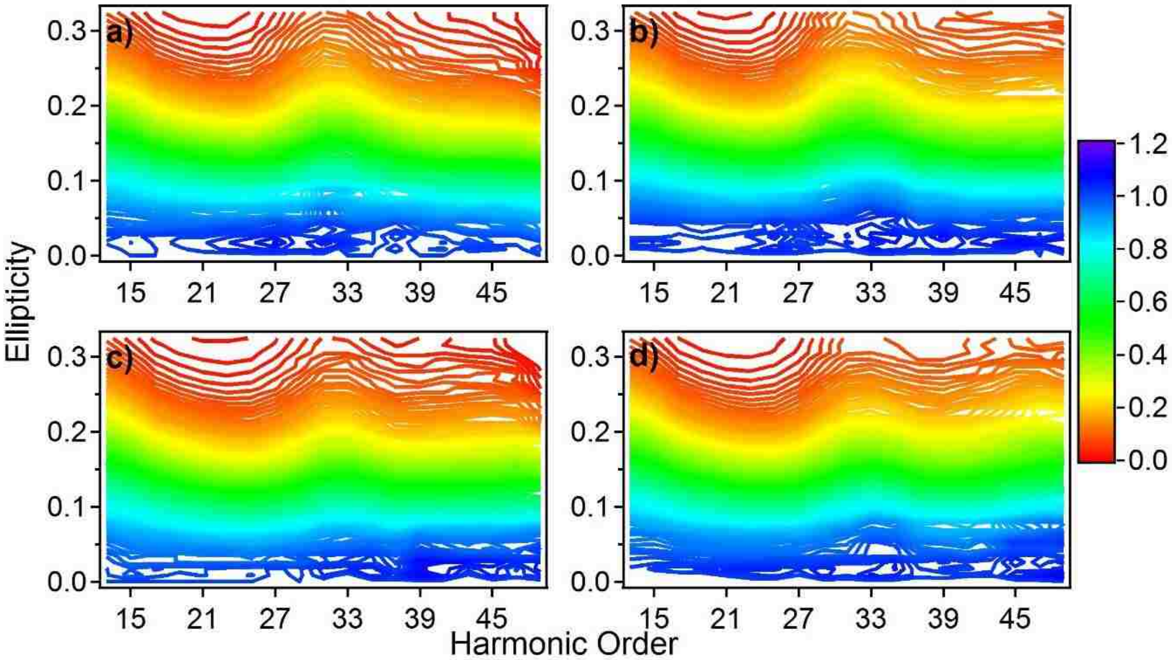

Figure 7.4. Contour plots of normalized Ar harmonic intensity as a function of laser ellipticity taken with the KLS laser system. The peak laser intensities were (a) and (c) 3.97x10^{14} W/cm^2 and (b) and (d) 5.10x10^{14} W/cm^2. The laser was focused (a)-(b) 2.79 mm in front of the center of the gas jet and (c)-(d) 3.54 mm in front of the center of the gas jet. A feature occurred centered at the 31st or 33rd harmonic at both intensities and multiple focusing conditions.

Figure 7.5 shows the harmonic intensity curves versus ellipticity for various harmonics taken with the HITS laser at 3.95x10^{14} W/cm^2 and the laser focused 2 mm before the center of the gas jet. The area under each curve was set to one for an easier visual comparison. Harmonics 29, 31, and 33 are shown in bright colors, while the other harmonics are shown in various greys. The 31st and 33rd harmonics did not decay all the way to zero and, as such, had a broader curve than did the harmonics further from the Ar Cooper minimum. Harmonic 13 was also very broad and did not decay to the same baseline as the other harmonics; however, this is likely due to harmonic 13 being relatively close to the Ar ionization threshold.

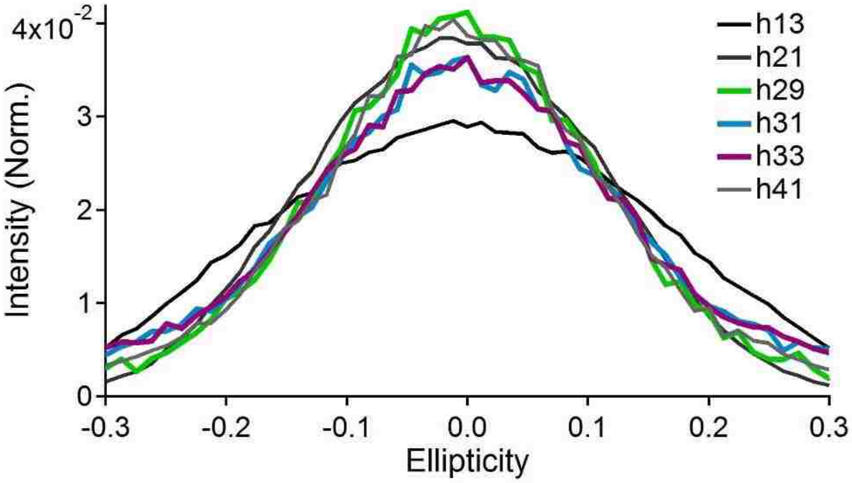

Figure 7.5. Normalized harmonic intensity curves as functions of laser ellipticity are shown for Ar harmonics 13, 21, 29, 31, 33, and 41. These data were collected with the HITS laser system at a peak intensity of 3.95x10^{14} W/cm^2 and the laser focused 2 mm in front of the center of the gas jet. Harmonics 31 and 33, while still having a Gaussian-like shape, were broader and had a slightly elevated baseline compared to the other harmonic curves. Harmonic 13, which is very near to the ionization threshold of Ar, was also very broad.

The normalized harmonic intensities, as shown in Figure 7.5, were fit to Equation 1.15, the model suggested by Moller, et al.,[21] for harmonic intensity as a function of ellipticity. Chi squared is a parameter that is a measure of the quality of a fit.[35] As the chi squared value approaches zero, the fit is approaching a perfect match to the data. Generally, a chi squared value of one or less signifies a good fit.[35] The chi squared values from the fits of each of the normalized harmonic intensity curves are plotted in Figure 7.6. As the harmonic order increased, the harmonic intensity decreased, even with linearly polarized light. As harmonic intensity decreases, the measurement error is expected to increase; so the chi squared values should also increase. In Figure 7.6 there was an abrupt rise in the chi squared at harmonic 29 followed by a slight decrease at harmonic 41 before the values began to gradually rise again.

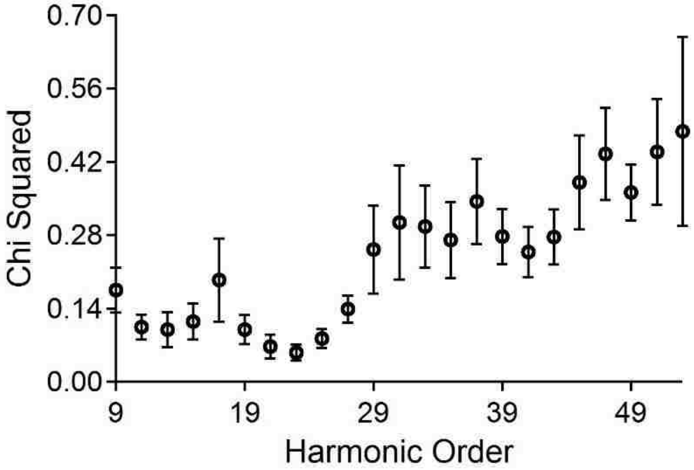

Figure 7.6. Chi squared values from Gaussian fits of the normalized Ar harmonic intensities as functions of laser ellipticity. These data were taken with the HITS laser system at 3.95x10^{14} W/cm^{2} and with the laser focused 2 mm in front of the center of the gas jet. A gradual decrease in the quality of the fit as the harmonic order increased was expected since the intensity of the harmonics decreased at higher harmonic orders. However, harmonics 29-41 had an unexpected increase in the chi squared values; this range of harmonic orders includes the harmonics which were affected by the Ar Cooper minimum.

7.3.2 Krypton Results

Argon is known to have a Cooper minimum at approximately 50 eV from both photoionization and HHG experiments; however, the Cooper minimum in Kr appears at a higher energy, 85 eV,[11,16] which is beyond the energy range of harmonics generated with an 800 nm laser. Thus, for comparison purposes, the same experiments, as presented above for Ar, were also performed with Kr as the medium.

The phase-matching between Ar and Kr for identical setups should be extremely similar. In Figure 7.7, the harmonic spectral envelopes from a variety of focusing conditions for both the HITS laser, (a) and (b), and the KLS laser, (c) and (d), were overlaid with the total photoionization cross section for Kr from Samson, et al.[11] The HITS setup for Ar and Kr was identical; however, the KLS setup for the Ar and Kr data used different pulsed valve. The Ar data, shown in Figure 7.1(c) and (d) was taken using a piezo pulsed valve, while the Kr data, shown in Figure 7.7(c) and (d) was taken using an Even-Lavie pulsed valve. As mentioned in Section 7.2, these two valves are expected to produce supersonic gas jets of different shapes near the nozzle. This was important because in these experiments the laser was focused very close to the nozzle in order to maximize the gas density of the medium. From Figure 7.7(a) and (b), just as in Figure 7.1(a) and (b), the optimum phase-matching appeared to occur around +2 mm, where the maximum number of harmonics was seen and the harmonic spectral envelope mapped decently to the

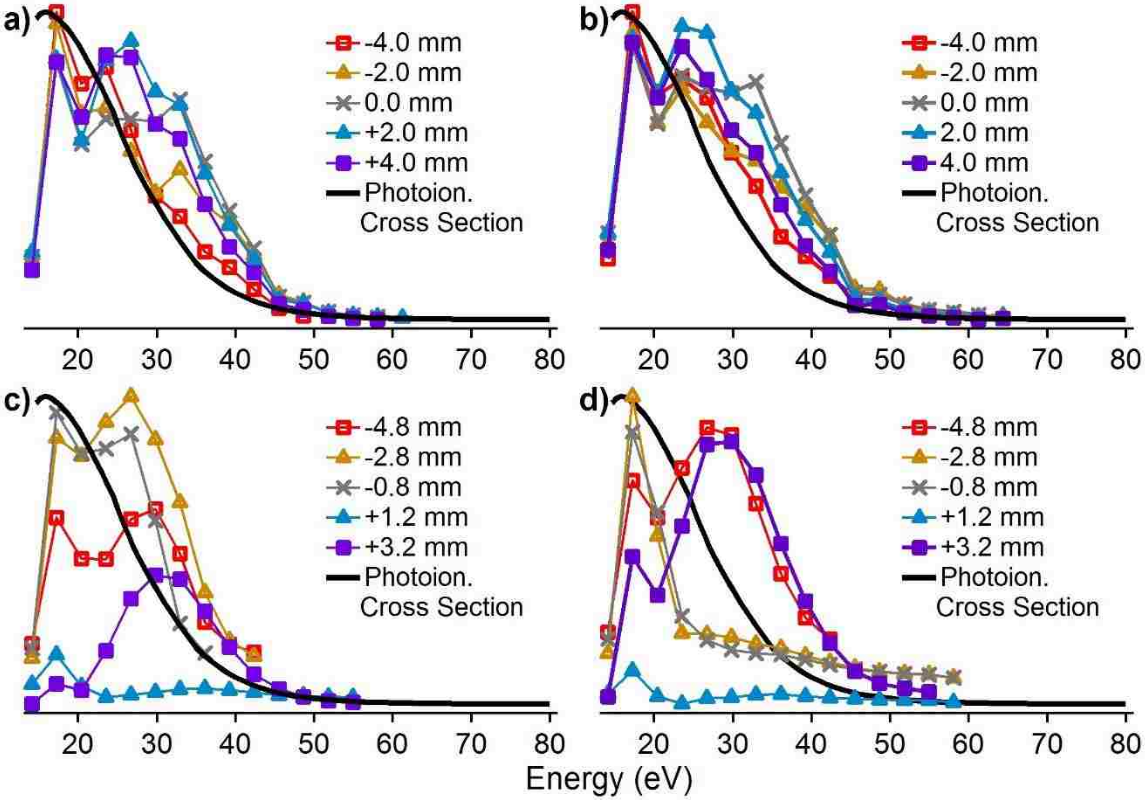

Figure 7.7. Comparison of the absolute photoionization cross section from Samson, et al. for Kr with HHG spectral envelopes spanning several focusing conditions. The photoionization cross section is a function of photon energy, and the HHG spectral envelopes are functions of harmonic energy, both in eV. The data in (a)-(b) were taken with the HITS laser system using a capillary for a sample inlet. The peak laser intensites were (a) 2.86x10^{14} W/cm^{2} and (b) 3.95x10^{14} W/cm^{2}. The data in (c)-(d) were taken with the KLS laser system using an Even-Lavie pulsed valve. The peak laser intensities were (c) 2.16x10^{14} W/cm^{2} and (d) 3.14x10^{14} W/cm^{2}. For the HITS data, the best focusing position appeared to be +2 mm, since these positions showed both the most harmonics and the best qualitative agreement with the photoionization cross section. Similarly, for the KLS data, the best focusing condition appeared to occur at +3.2 mm.

photoionization cross section. For the KLS data, shown in Figure 7.7(c) and (d), the best phase-matching appeared to occur when the laser was focused +3.2 mm in front of the center of the gas jet.

Similar to the analysis performed on the Ar data, the Kr spectral envelopes were all normalized to the spectral envelopes generated with linear light, and all other parameters were kept the same (i.e., the laser intensity and laser focusing conditions were kept constant). The normalized data for two different HITS laser intensities and three different focusing conditions, 0, -2 and +2 mm, are shown as contour plots in Figure 7.8. Harmonic 9 will not be discussed here since it is below or at the Kr ionization threshold, where different physical behavior of the harmonics was expected. A very broad feature appeared in the Kr contour plots, shown in Figure 7.8, spanning harmonics 19 through 31. In this feature, the harmonics appeared to require more laser ellipticity to decay to zero. Unlike with the feature which occurred in the Ar data, shown in Figures 7.2 and 7.4, the feature in Figure 7.8 did not appear to be constant, with small changes in focal position and changes in the laser intensity.

The contour plots of normalized Kr harmonic intensity, analogous to Figure 7.8, are shown in Figure 7.9 for data acquired with the KLS laser system at three different focusing conditions and two different laser intensities. Just as before, the vertical axes are laser ellipticity and the horizontal axes are harmonic order. For Figure 7.9, as in Figures 7.3, 7.4, and 7.8, the harmonic intensities were normalized to the harmonic intensity generated with linearly polarized light. One may notice that there was a feature occurring between harmonics 13 and 19 in the better phase-

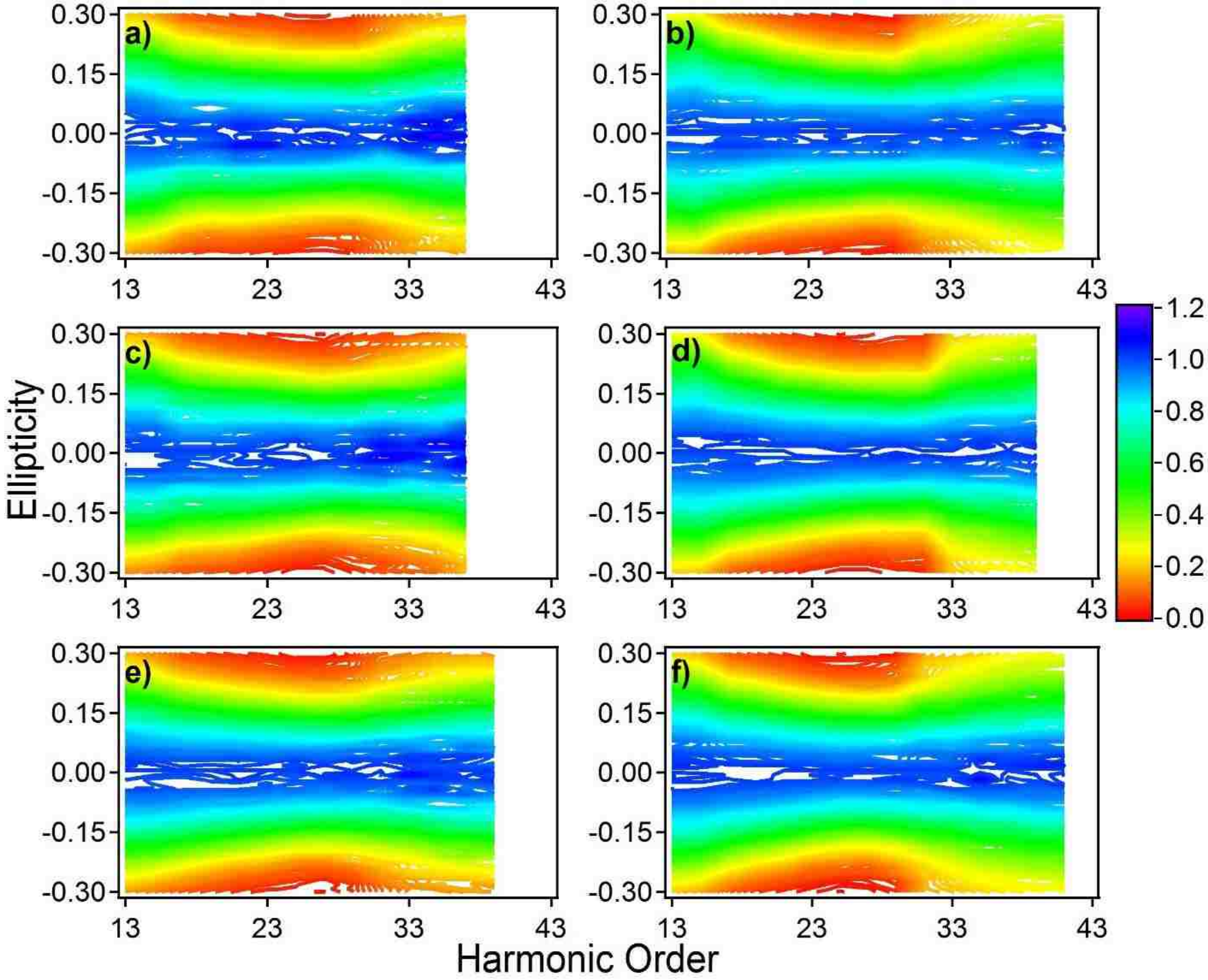

Figure 7.8. Contour plots of normalized Kr harmonic intensity as a function of laser ellipticity taken with the HITS laser system. The peak laser intensities were (a), (c), and (e) 2.86x10^{14} W/cm^2 and (b), (d), and (f) 5x10^{14} W/cm^2. The laser was focused (a)-(b) 2 mm behind the center of the gas jet, (c)-(d) at the center of the gas jet, and (e)-(f) 2 mm in front of the center of the gas jet. There was a broad feature occurring after the 33rd harmonic.

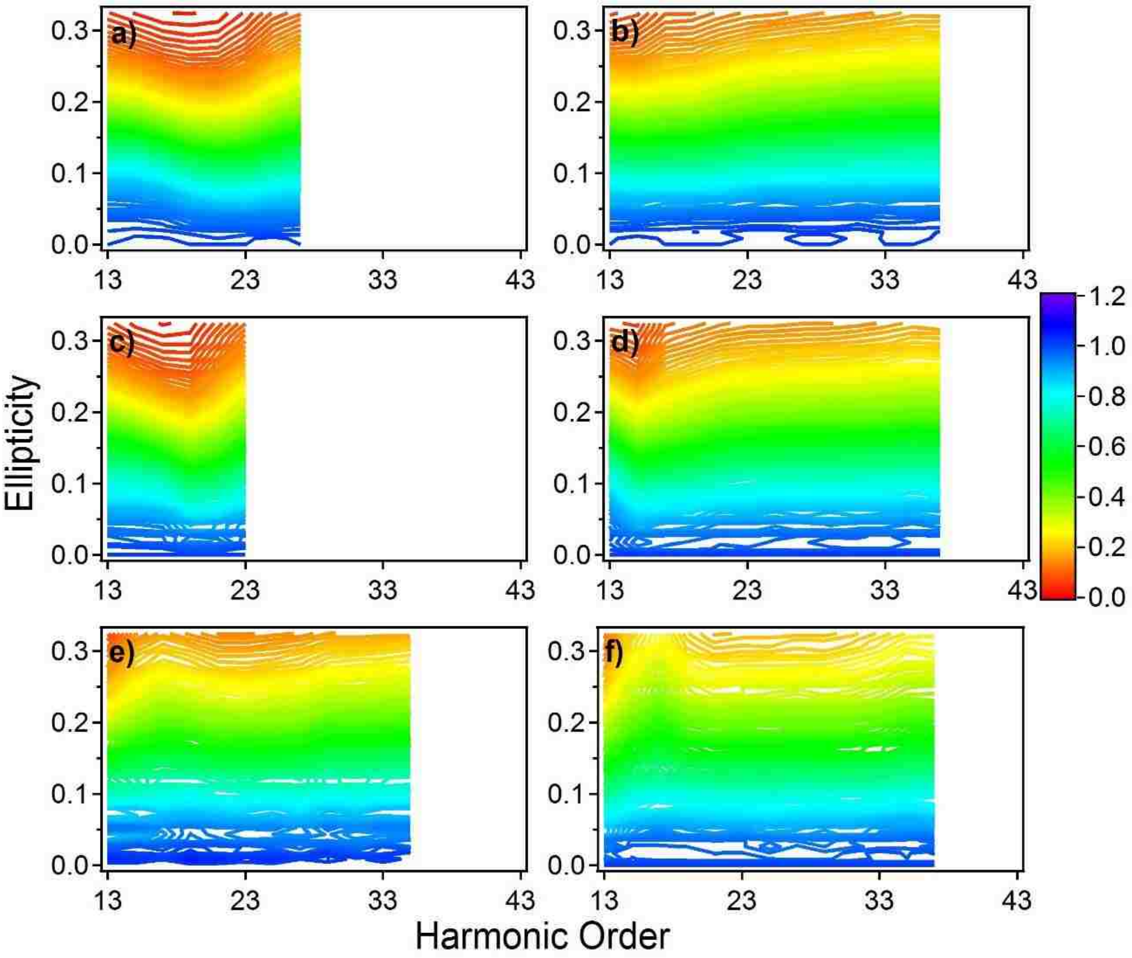

Figure 7.9. Contour plots of normalized Kr harmonic intensity as a function of laser ellipticity taken with the KLS laser system. The peak laser intensities were (a) and (c) 2.16×10^{14} W/cm^2 and (b) and (d) 3.71×10^{14} W/cm^2. The laser was focused (a)-(b) 1.8 mm behind of the center of the gas jet, (c)-(d) 0.8 mm behind of the center of the gas jet, and (e)-(f) 3.2 mm in front of the gas jet. Above the ionization threshold, the harmonic intensities appeared to decay relatively uniformly with increasing ellipticity.

matched data, shown in Figure 7.9(e) and (f). This feature was not present in all of the data taken at decent focusing positions, however. The remainder of the above threshold harmonics for Kr appeared to decrease relatively uniformly with increasing ellipticity.

The chi squared values obtained from fitting the harmonic decay with added ellipticity of the Kr HITS data is shown in Figure 7.10. In Figure 7.10 the vertical axis is chi squared value and the horizontal axis is harmonic order.There was an increase in the error of the fits starting at harmonic 29 and going through harmonic 41.

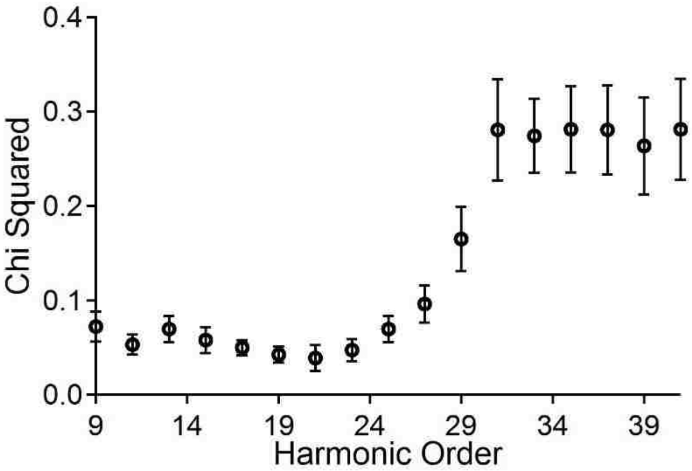

Figure 7.10. Chi squared values from Gaussian fits of the normalized Kr harmonic intensities as functions of laser ellipticity. The data shown were taken with the HITS laser system at 3.95x10^{14} W/cm^{2} and with the laser focused 2 mm in front of the center of the gas jet. A gradual decrease in the quality of the fit as the harmonic order increased was expected since the intensity of the harmonics decreased at higher harmonic orders. However, harmonics 31 and higher order had a large jump in chi squared value.

7.4 DISCUSSION

7.4.1 Discussion of Argon Results

From Figure 7.1, the best phase-matching for the Ar data taken with the HITS system and with the KLS occurred when the laser was focused around 2 mm and 3 mm, respectively, before the center of the gas jet. The discrepancies between the spectral envelopes and the phase-matching conditions between the two lasers were likely due to the difference in the Rayleigh range of the two laser systems.

A relatively narrow feature was visible in all the contour plots shown in Figure 7.2, centered at the 31st harmonic, which corresponded to a photon energy of 48.7 eV. The Ar Cooper minimum appears at 47 eV in photoionization experiments.[11,12] The feature persisted under several different phase-matching conditions, which provided evidence that this feature was from the electron rescattering dynamics with the atom. As the laser was moved further away from the focusing position which provided optimal phase-matching conditions, there were fewer visible harmonics. Also, at lower intensities, the number of visible harmonics decreased. However, under all the conditions at which the Ar data were collected, the feature at the 31st harmonic persisted, and it appeared to be less responsive to added ellipticity than the other harmonics. In Figure 7.4, even though the ellipticity was only added in a single direction, there was a feature, which occurred around the energy of the Ar Cooper minimum. In both the KLS and HITS data, this feature occurred at the 31st harmonic. Also, the feature around the Cooper minimum was much broader in the contours of the KLS data than it was in the contours of the HITS data. The laser intensity, as well as focusing, due to the Rayleigh range, were different between the two laser systems, so the shifting and broadening of the feature did not necessarily come as a surprise. The fact that the feature occurred in both data sets, under a variety of conditions, is strong evidence that this resistance to harmonic decay as a function of ellipticity was directly related to the presence of the Cooper minimum. As expected, in Figure 7.2, the different directions of ellipticity applied to the laser showed nearly identical harmonic behaviors.

By showing the individual harmonic intensity curves as a function of ellipticity, as was done in Figure 7.5, it became clear that the harmonics closest in energy to the Ar Cooper minimum did not respond to added laser ellipticity in completely the same way as did the other harmonics; however, their response was not completely different either. All of the harmonics appeared to decrease as a function of ellipticity with a Gaussian-like shape. The slope of this decrease, however, was smaller for the harmonics closest to the Cooper minimum, harmonics 31 and 33. Harmonics 31 and 33 showed a smaller slope, and therefore a broader curve, than the other harmonics. These harmonics also did not decrease to the same baseline as the other harmonics.

From Figure 7.6, when these harmonic intensity curves were fit to the model from Equation 1.15, the error of the fit was significantly higher for harmonics 29-41, further indicating that the decay of these harmonics did not follow the same pattern as the other harmonics.

7.4.2 Discussion of Krypton Results

The Kr data were collected to serve as a control, or comparison, for the Ar data since the harmonic energy range in this study was too low to detect the Kr

Cooper minimum. In Figure 7.7, the best phase-matching for the HITS data occurred at a laser focus position of +2 mm, which was expected since the conditions were the same for the Ar and Kr HITS data. For the Kr data obtained with the KLS laser system and the Even-Lavie pulsed valve, it appeared that the best phase-matching probably occurred when the laser was focused somewhere between 1.2 and 3.2 mm before the center of the gas jet. The HHG spectral envelope taken at 1.2 mm showed the maximum number of harmonics, however, the overall shape did not match well to that of the photoionization cross section. At 3.2 mm, the overall shape of the HHG spectra was better aligned with the photoionization cross section.

The contour plots of normalized Kr harmonic intensity in Figure 7.8 showed a broad feature occurring for the highest order harmonics, the 33rd through the 41st. This broad feature appears to be just the first half of something, as it does not decay. This may be due to the Kr Cooper minimum, which should occur around the 43rd harmonic or higher order. However, there is not a sharp feature, as there was in the Ar contour plots, shown in Figures 7.3 and 7.4. On the contrary, the Kr data contour plots shown in Figure 7.9, which were taken using the KLS laser, were relatively featureless, with all of the harmonics decaying rather uniformly with increasing ellipticity. The KLS Kr data also only extended through the 37th harmonic, where the HITS Kr data extended through the 41st harmonic. The narrow, lower energy features, which occurred in the Kr data shown in Figure 7.9, were not constant across broad phase-matching conditions and, thus, were not likely related to the dynamics of the atom.

The Ar ellipticity data showed clear trends, whereas the Kr data did not show as much evidence for trends which extend over a broad range of phase-matching conditions. The lack of obvious trends occurring in the Kr ellipticity dependent data was further evidence that the trends in the Ar ellipticity dependent data were from the Ar Cooper minimum.

7.5 SUMMARY

By analyzing the harmonic response as the laser ellipticity was increased under a variety of focusing conditions, the electron rescattering dynamics of the atom could be analyzed. In Ar, the harmonics closest in energy to the Cooper minimum responded differently to added laser ellipticity than did the other high-order harmonics generated. Closest to the Cooper minimum, the Ar harmonics required more ellipticity to decay than did the other harmonics. In Kr, as expected since there are no known electron dynamics in the energy region studied, all of the generated harmonics decayed uniformly, and no phase-matching independent trends arose.

These atomic studies provide convincing evidence that electron rescattering dynamics can be probed and further studied using laser ellipticity-dependent high-order harmonic generation. While this evidence is convincing, it is important for a model to be developed to help to extract the electron dynamical information since much information about the atomic medium and the laser is imbedded within each harmonic. These data showed that the harmonic decay as a function of laser polarization was clearly affected by the electron rescattering dynamics of the medium.

The ideas presented in this chapter should be further explored using longer wavelength lasers. By going to longer wavelengths, harmonics may be generated in the correct energy region of the Kr Cooper minimum. Showing that harmonics nearest in energy to the Kr Cooper minimum behave similarly to those around the Ar Cooper minimum would provide further evidence of using the ellipticity of the driving laser to probe the photorecombination electron rescattering dynamics.

Chapter 8, High-Order Harmonics Generated From Carbon Tetrafluoride Show Dependence on Laser Polarization, will continue the investigation of laser ellipticity-dependent HHG as a potential probe for electron rescattering dynamics. Ellipticity-dependent HHG data for carbon tetrafluoride, a molecule which does not require alignment, will be analyzed in a similar fashion.

7.6 REFERENCES

[1] P.B. Corkum, Phys. Rev. Lett. 71 (1993) 1994.

[2] K.J. Schafer, B. Yang, L.F. DiMauro, K.C. Kulander, Phys. Rev. Lett. 70 (1993) 1599.

[3] C.-G. Wahlstrom, J. Larrson, A. Persson, T. Starczewski, S. Svanberg, P. Salieres, P. Balcou, A. L'Huiller, Phys. Rev. A 48 (1993) 4709.

[4] M. Lein, N. Hay, R. Velotta, J.P. Marangos, P.L. Knight, Phys. Rev. A 66 (2002) 023805.

[5] P.K. Ghosh, Introduction to Photoelectron Spectroscopy, John Wiley & Sons, New York, 1983.

[6] M. Lewenstein, P. Balcou, M.Y. Ivanov, A. L'Huiller, P.B. Corkum, Phys. Rev. A 49 (1994) 2117.

[7] V.V. Strelkov, M.A. Khokhlova, A.A. Gonoskov, I.A. Gonoskov, M.Y. Ryabikin, Phys. Rev. A 86 (2012) 013404.

[8] H.J. Worner, H. Niikura, J.B. Bertrand, P.B. Corkum, D.M. Villeneuve, Phys. Rev. Lett. 102 (2009) 103901.

[9] J. Higuet, H. Ruf, N. Thire, R. Cireasa, E. Constant, E. Cormier, D. Descamps, E. Mevel, S. Petit, B. Pons, Y. Mairesse, B. Fabre, Phys. Rev. A 83 (2011) 053401.

[10] J.W. Cooper, Phys. Rev. 123 (1962) 681.

[11] J.A.R. Samson, W.C. Stolte, J. Electron. Spectrosc. Relat. Phenom. 123 (2002) 265.

[12] G.V. Marr, J.B. West, At. Data Nucl. Data Tables 18 (1976) 497.

[13] M.C.H. Wong, A.-T. Le, A.F. Alharbi, A.E. Boguslavskiy, R.R. Lucchese, J.-P. Brichta, C.D. Lin, V.R. Bhardwaj, Phys. Rev. Lett. 110 (2013) 033006.

[14] J.P. Farrell, L.S. Spector, B.K. McFarland, P.H. Bucksbaum, M. Guhr, M.B. Gaarde, K.J. Schafer, Phys. Rev. A 83 (2011) 023420.

[15] C. Jin, H.J. Worner, V. Tosa, A.-T. Le, J.B. Bertrand, R.R. Lucchese, P.B. Corkum, D.M. Villeneuve, C.D. Lin, J. Phys. B.: At. Mol. Opt. Phys. 44 (2011) 095601.

[16] A.D. Shiner, B.E. Schmidt, C. Trallero-Herrero, P.B. Corkum, J.-C. Kieffer, F. Legare, D.M. Villeneuve, J. Phys. B.: At. Mol. Opt. Phys. 45 (2012) 074010.

[17] K.-H. Hong, C.-J. Lai, V.-M. Gkortsas, S.-W. Huang, J. Moses, E. Granados, S. Bhardwaj, F.X. Kartner, Phys. Rev. A 86 (2012) 043412.

[18] C. Trallero-Herrero, C. Jin, B.E. Schmidt, A.D. Shiner, J.-C. Kieffer, P.B. Corkum, D.M. Villeneuve, C.D. Lin, F. Legare, A.T. Le, J. Phys. B.: At. Mol. Opt. Phys. 45 (2012) 011001.

[19] A.D. Shiner, B.E. Schmidt, C. Trallero-Herrero, H.J. Worner, S. Patchkovskii, P.B. Corkum, J.-C. Kieffer, F. Legare, D.M. Villeneuve, Nature Physics 7 (2011) 464.

[20] P. Dietrich, N.H. Burnett, M. Ivanov, P.B. Corkum, Phys. Rev. A 50 (1994) R3585.

[21] M. Moller, Y. Cheng, S.D. Khan, B. Zhao, K. Zhao, M. Chini, G.G. Paulus, Z. Chang, Phys. Rev. A 86 (2012) 011401.

[22] A. Flettner, J. Konig, M.B. Mason, T. Pfeifer, U. Weichmann, R. Duren, G. Gerber, Eur. Phys. J. D 21 (2002) 115.

[23] H. Xu, H. Xiong, B. Zeng, W. Chu, Y. Fu, J. Yao, J. Chen, X. Liu, Y. Cheng, Z. Xu, Opt. Lett. 35 (2010) 472.

[24] F. He, C. Ruiz, A. Becker, Opt. Lett. 32 (2007) 3224.

[25] T. Kanai, S. Minemoto, H. Sakai, Phys. Rev. Lett. 98 (2007) 053002.

[26] M.V. Frolov, N.L. Manakov, T.S. Sarantseva, A.F. Starace, Phys. Rev. A 86 (2012) 063406.

[27] G. Gbur, E. Wolf, J. Mod. Opt. 48 (2001) 1735.

[28] M.B. Gaarde, J.L. Tate, K.J. Schafer, J. Phys. B.: At. Mol. Opt. Phys. 41 (2008) 132001.

[29] B.R. Sickmiller, R.R. Jones, Phys. Rev. A 80 (2009) 031802(R).

[30] C. Winterfeldt, C. Spielmann, G. Gerber, Rev. Mod. Phys. 80 (2008) 117.

[31] B.P. Wilson, K.D. Fulfer, S. Mondal, X. Ren, J. Tross, E.D. Poliakoff, J. Jose, A.-T. Le, R.R. Lucchese, C. Trallero-Herrero, High order harmonic generation from SF6: Deconvolution of macroscopic effects, 2015.

[32] P. Salieres, A. L'Huiller, M. Lewenstein, Phys. Rev. Lett. 74 (1995) 3776.

[33] M. Kakehata, H. Takada, H. Yumoto, K. Miyazaki, Phys. Rev. A 55 (1997) R861.

[34] N.H. Burnett, C. Kan, P.B. Corkum, Phys. Rev. A 51 (1995) R3418.

[35] R.L. Plackett, Int. Stat. Rev. 51 (1983) 59.

CHAPTER 8
HIGH-ORDER HARMONICS GENERATED FROM CARBON TETRAFLUORIDE SHOW DEPENDENCE ON LASER POLARIZATION

This chapter continues the discussion which began in Chapter 7 on using laser ellipticity-dependent high order harmonic generation (HHG) to probe electron rescattering dynamics. While Chapter 7 discussed results from atomic media, this chapter explores results from a molecular medium, carbon tetrafluoride, which has two known shape resonances in photoionization from the $1t_1$ orbital.[1]

8.1 INTRODUCTION

The idea of using the laser ellipticity as a probe for electron rescattering dynamics in HHG studies was introduced in Chapter 7, Harmonics Near Ar Cooper Minimum Resist Decay With Added Laser Ellipticity: A Potential HHG Probe. Evidence for this probe was presented for the atomic target Ar, and it was shown that the harmonics closest in energy to the Ar Cooper minimum did not have the same response to increased laser ellipticity as did the surrounding harmonics. In this chapter, evidence for this probe is presented for a molecular target, specifically carbon tetrafluoride.

Carbon tetrafluoride (CF_4) is a tetrahedral molecule and, as such, cannot be optically aligned. The lack of optical alignment was not an issue for this study since the molecule, along with its molecular orbitals, has a relatively high degree of symmetry. Photoionization from the $1t_1$ orbtial of CF_4 is known to be affected by two shape resonances at photon energies 25 and 34 eV.[1,2]

8.2 ADDITIONAL EXPERIMENTAL DETAILS

The experimental setup and the HHG spectrometer were described in detail in Chapter 2, Section 2.4. The CF_4 HHG data were collected using the KLS laser system, as described in Chapter 2, Section 2.5.1, using an Even-Lavie pulsed valve for sample entry into the vacuum chamber. The data were collected over a range of laser focusing conditions and at a peak laser intensity of 3.21 W/cm^2. Ellipticity was added only in one direction to the laser pulse.

8.3 RESULTS

As was discussed in Chapter 7, phase-matching is incredibly important in high-order harmonic generation experiments. Experimentally, the optimum phase-matching conditions are found when the maximum number of harmonics are seen, and the HHG spectral envelopes map nicely to the photoionization cross section for the medium gas. Figure 8.1 shows the overlay of the HHG spectral envelopes for the laser focused 4.3 mm behind the center of the gas jet (red open squares), 2.3 mm in front of the center of the gas jet(blue closed triangles), and 5.3 mm in front of the center of the gas jet (purple closed squares), all overlaid with the partial photoionization cross section for ionization from the $1t_1$ orbital of CF_4 as published by Carlson, et al.[1] Only the region of the photoionization cross section where the shape resonance occurs is shown in Figure 8.1. The intensity of the partial photoionization cross section is scaled for easier comparison with the HHG data. The partial photoionization cross section is plotted as a function of photon energy, and the HHG spectral envelopes are shown as functions of harmonic energy; both energy scales are in eV. Positive focus positions correspond to the laser focus preceding the center of the gas jet, while negative positions correspond to the laser focus following the center of the gas jet. From Figure 8.1, the best phase-matching occurred when the laser pulse was focused 5.5 mm in front of the center of the gas jet.

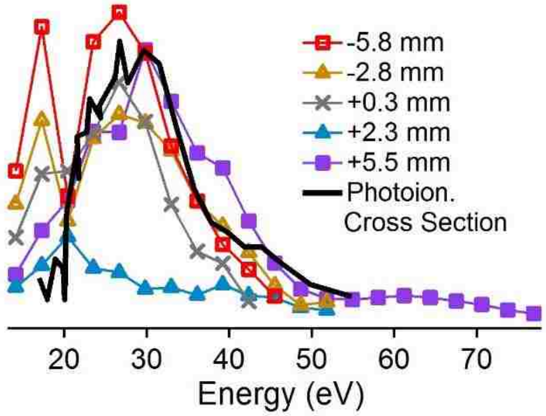

Figure 8.1. An overlay of CF_4 HHG spectral envelopes from several different laser focus positions and the partial photoionization cross section for ionization from the $1t_1$ orbital of CF_4 published by Carlson, et al.[1] Positive focus positions correspond to the laser focus preceding the center of the gas jet while negative positions correspond to the laser focus following the center of the gas jet. For the conditions used in this experiment, the optimal phase-matching occurred with the laser focused 5.5 mm before the center of the gas jet.

To analyze the effect of laser ellipticity on the individual harmonics, all of the spectral envelopes were normalized to the spectral envelope generated with linearly polarized light and all other parameters kept the same (i.e., the laser intensity and laser focusing conditions were kept constant). The normalized contour plots for CF_4 taken at six different focusing conditions are shown in Figure 8.2. Harmonics 9 and 11 were below or at the ionization threshold for CF_4 and, as such, will not be discussed in this dissertation.

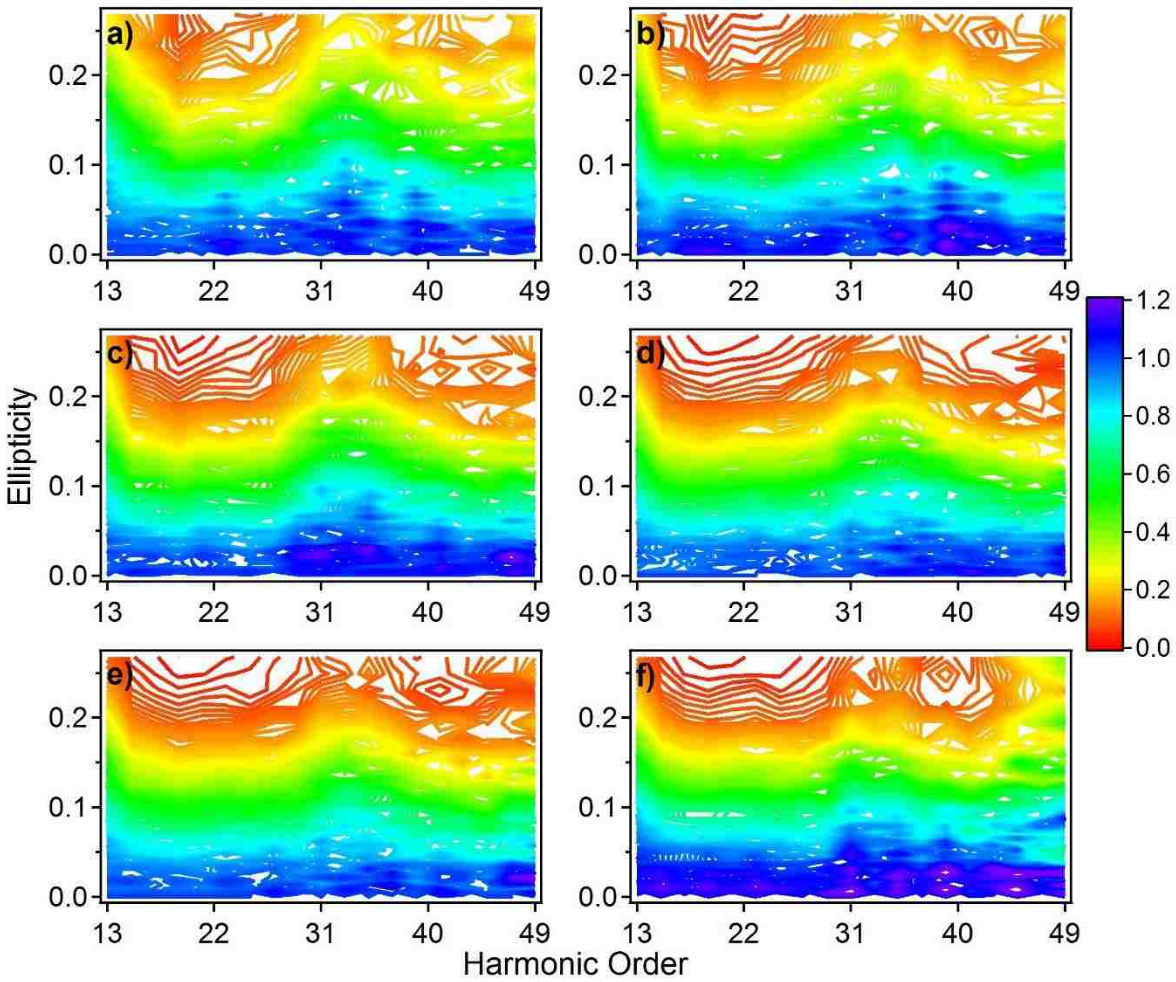

Figure 8.2. Contour plots of normalized CF_4 harmonic intensity as a function of ellipticity taken with the KLS laser system with the laser focused (a) 3.53 mm, (b) 4.03 mm, (c) 4.53 mm, (d) 5.03 mm, (e) 5.53 mm, and (f) 6.03 mm in front of the center of the gas jet. A weak, very broad feature centered at the 33rd harmonic occurred in all of the contour plots. This feature was present for all of the phase-matching conditions shown at which ellipticity data was collected.

To further analyze the effect of laser ellipticity on the CF_4 harmonic spectrum, the harmonic lineouts taken at different laser ellipticities were overlaid. In Figure 8.3, harmonic lineouts for laser ellipticities of 0, 0.1 and 0.2 are shown overlaid. The baselines for the CF_4 data were constant, as expected, and the harmonics decayed with increased laser ellipticity.

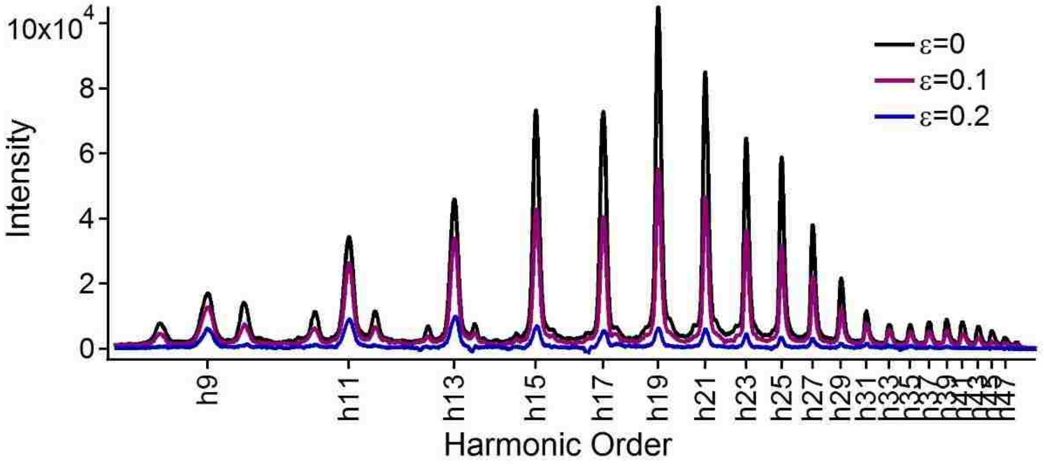

Figure 8.3. Harmonic lineouts from different laser ellipticity values. These data were taken with the laser focused 5.5 mm before the center of the gas jet. Ellipticity was added only in one direction for this data. The CF_4 harmonic signal decreased with increasing ellipticity, as expected; however, less laser ellipticity was required for the CF_4 harmonics to be depleted than for either of the atomic harmonics discussed in Chapter 7.

The harmonic intensities were each graphed as a function of laser ellipticity. The areas under these harmonic intensity curves were normalized for better comparison. An overlay of these curves for several of the harmonic orders is shown in Figure 8.4 for the CF_4 data obtained with the laser focused 5.5 mm in front of the center of the gas jet. All of the harmonic intensity curves are shown in a variety of grey tones.

The harmonic intensity curves were then fitted to the Gaussian model proposed by Moller, et al.[3] and shown in Equation 1.15 in Chapter 1. As mentioned in Chapter 7, Section 7.3.1, chi squared is a value which describes the fit quality. The chi squared value approaches zero as the fitted curve approaches an exact match to the actual data. Chi squared values from the fittings of the CF_4 harmonic intensity curves with Equation 1.15 are shown in Figure 8.5. As the harmonic order increased, the overall harmonic intensity decreased. As the intensity decreased, the error in the measurement was expected to increase, causing the chi squared values to also increase.

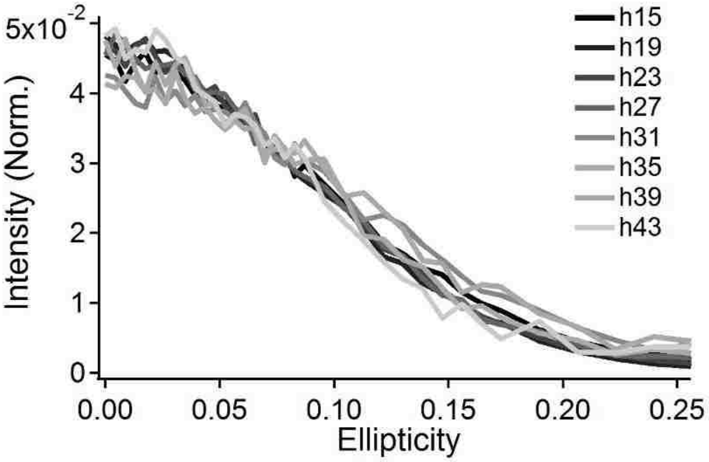

Figure 8.4. Normalized harmonic intensity curves as functions of laser ellipticity are shown for several harmonic orders. All of the harmonic intensity curves appeared to be very similar to one another.

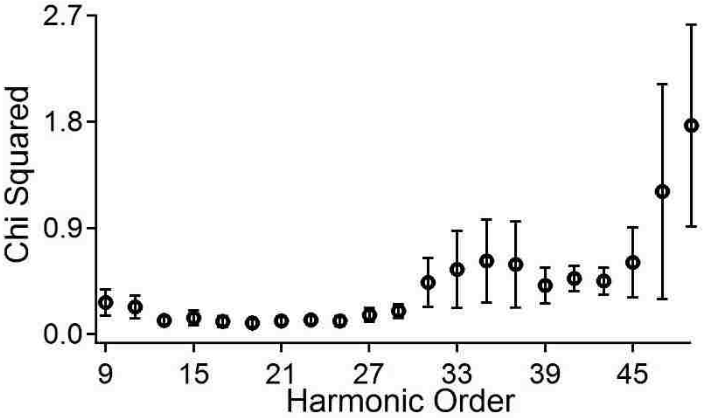

Figure 8.5. Chi squared values from Gaussian fits of the normalized harmonic intensity curves as functions of laser ellipticity. These data were taken with the laser focused 5.5 mm in front of the center of the gas jet. A gradual rise in the fitting error was expected as the harmonic order increased, since the higher ordered harmonics had lower intensities.

8.4 DISCUSSION

One may notice that the contour plots for the molecular HHG data were not as well defined as for the atomic HHG data. The harmonics generated in molecular media tended to be much lower in intensity than those generated in atomic media. As the harmonic intensity decreased, the statistical error in the measurement increased, which caused the contour to be less defined.

In the harmonic intensity contour plots, shown in Figure 8.2, there was a broad feature centered around the 33rd harmonic. This feature was broader than the feature centered at the Ar Cooper minimum in the KLS harmonic data, shown in Chapter 7, Figure 7.4. The broad feature, which occurred at the Ar Cooper minimum, extended over approximately five harmonics at its broadest point. However, this feature, in the CF_4 data, extended over approximately seven harmonics. The contour plot for the CF_4 data taken with the laser focused 5.5 mm before the center of the gas jet is shown again in Figure 8.6 on a harmonic energy scale in eV, as opposed to a harmonic order scale.

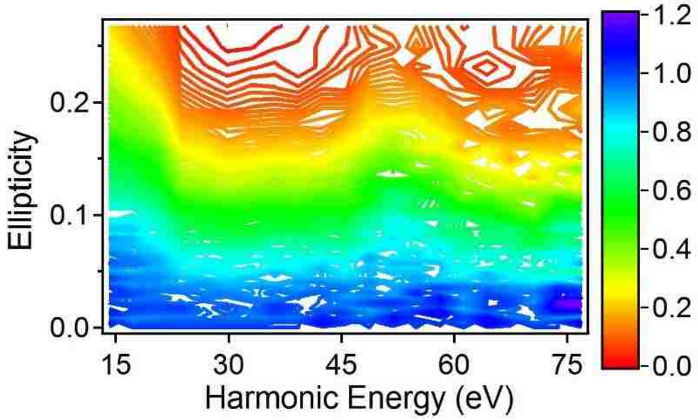

Figure 8.6. Contour plot of normalized harmonic intensity as a function of ellipticity for harmonics generated in CF_4 with the laser focused 5.5 mm in front of the center of the gas jet. The contour plot is shown on a harmonic energy scale in eV.

Figure 8.6 shows that the broad figure, which occurred in the CF_4 contour plots, was not actually in the correct energy range for the shape resonant features which are known to occur in photoionization from the $1t_1$ orbital of CF_4. One may recall from Figure 8.1 that the shape resonances affected the partial photoionization cross section for the $1t_1$ orbital from 20 to 50 eV. The feature which appeared in the HHG contour plots spanned the energy range of 45 to 65 eV. There are a few possible reasons for this discrepancy. First, it is difficult to know with certainty from which molecular orbital the electron tunneled and recombined. In an atom, the energy levels of the various orbitals are fairly spread out, so it is highly probable that in atomic HHG, the electron always tunnels and recombines from the highest occupied atomic orbital exclusively. In a molecule, on the other hand, the various orbitals can be quite close in energy. In fact, the three outermost valence orbitals of CF_4 all fall within 3 eV,[1] whereas in Ar, the highest occupied atomic orbital and its energetically nearest occupied orbital are separated by over 12 eV.[4] Since there are three molecular orbitals, very closely spaced in energy, in the valence shell of CF_4, it is possible that the electron tunnels from and recombines with either the $1t_1$, $4t_2$ or 1e orbitals. It has also been reported previously that the HHG spectrum can contain contributions from multiple orbitals.[5-10] Shape resonances are also known to affect photoionization from the $4t_2$ and 1e orbitals of CF_4.[1] In particular, photoionization from the $4t_2$ orbital of CF_4 is affected by shape resonances over the photon energy range from 20 to almost 50 eV, and the 1e orbital is affected over the photon energy range from 23 to 35 eV.[1] For all of the three outermost valence orbitals of CF_4, the shape resonance effects would be expected at a lower energy than the feature, which occurred in the HHG contour plots. Another explanation is the shape resonance effects may be shifted in photorecombination as compared to photoionization. It is known that the location of a Cooper minimum can shift in HHG;

also, shape resonances have been studied far less than Cooper minima in HHG experiments; so it is possible that added ellipticity may shift the effects of the shape resonance. A final explanation as to why the feature occurred at a higher energy than the reported shape resonances may simply be that this feature was not due to a shape resonance effect. Since there is not a model for harmonic behavior as a function of ellipticity which takes into account the electron rescattering dynamics, there is not much guidance published as to the cause of this feature and its particular energy location.

Another interesting observation about the effects of ellipticity on the intensities of harmonics generated in a molecular medium is that the molecular harmonics seemed to be more sensitive to laser ellipticity than atomic harmonics. As illustrated in Figures 8.2 and 8.3, when the laser had an ellipticity of 0.2, the harmonics had decayed to about 5-6% of their intensity with linear light. Similarly, as evident from the Ar data, when the laser had an ellipticity of 0.2, the harmonics had only decayed to about 20% of their intensity with linear light. Thus, the CF_4 harmonics were visible over a smaller range of laser ellipticities than were the atomic data. The HHG process likely differs slightly for molecules and atoms due to the increased complexity of electronic structure for molecules.

The normalized harmonic intensity curves as functions of laser ellipticity, shown in Figure 8.4, appeared very similar for all of the harmonic orders above the CF_4 ionization threshold. Also, the chi squared values for the fittings of the CF_4 normalized harmonic intensity curves, shown in Figure 8.5, did not shown any significant features, meaning that all of the normalized curves fit decently to the

Gaussian model. The uniformity in the normalized intensity curves and the lack of features in the chi squared values for the CF_4 data differ from the Ar data, where clear trends appeared near the Cooper minimum. This difference is evidence that laser ellipticity affects shape resonant features differently than it does Cooper minima.

8.5 SUMMARY

The effects of laser ellipticity on harmonics around shape resonances differed significantly from those around a Cooper minimum. The visible trends in the harmonic intensity contour plots of CF_4 appeared at a higher energy than expected from the shape resonances known from photoionization studies. This shift in energy may have been a result of multiple orbital contributions, may suggest a difference in how laser ellipticity affects harmonics near a shape resonance, or, perhaps, may be due to some dynamic, which was not even anticipated. This study has provided evidence that laser ellipticity affects atomic and molecular harmonics differently. Until it is possible to incorporate electron rescattering dynamics into a model for the harmonic behavior as a function of laser ellipticity, many of the questions that this study has illuminated must remain unanswered.

8.6 REFERENCES

[1] T.A. Carlson, A. Fahlman, W.A. Svensson, M.O. Krause, T.A. Whitley, F.A. Grimm, M.N. Piancstelli, J.W. Taylor, J. Chem. Phys. 81 (1984) 3826.

[2] E.M. Nascimento, L.E. Machado, L.M. Brescansin, M.-T. Lee, J. Electron. Spectrosc. Relat. Phenom. 130 (2003) 101.

[3] M. Moller, Y. Cheng, S.D. Khan, B. Zhao, K. Zhao, M. Chini, G.G. Paulus, Z. Chang, Phys. Rev. A 86 (2012) 011401.

[4] A. Kramida, Y. Ralchenko, J. Reader, N.A. Team, NIST Atomic and Spectra Database (ver. 5.2). National Institue of Standards and Technology, Gaithersburg, MD, 2014.

[5] C. Jin, J.B. Bertrand, R.R. Lucchese, H.J. Worner, P.B. Corkum, D.M. Villeneuve, A.-T. Le, C.D. Lin, Phys. Rev. A 85 (2012) 013405.

[6] B.K. McFarland, J.P. Farrell, P.H. Bucksbaum, M. Guhr, Science 322 (2008) 1232.

[7] J. Li, P. Liu, H. Yang, L. Song, S. Zhao, H. Lu, R. Li, Z. Xu, Optics Express 21 (2013) 7599.

[8] Z. Diveki, A. Camper, S. Haessler, T. Auguste, T. Ruchon, B. Carre, P. Salieres, R. Guichard, J. Caillat, A. Maquet, R. Taieb, New Journal of Physics 14 (2012) 023062.

[9] H.J. Worner, J.B. Bertrand, P. Hockett, P.B. Corkum, D.M. Villeneuve, Phys. Rev. Lett. 104 (2010) 233904.

[10] O. Smirnova, Y. Mairesse, S. Patchkovskii, N. Dudovich, D.M. Villeneuve, P.B. Corkum, M.Y. Ivanov, Nature 460 (2009) 972.

CHAPTER 9
CONCLUSIONS AND OUTLOOK

The common aim of the studies discussed in this dissertation was to study how photoelectrons both enter (photorecombination) and exit (photoionization) systems, or in other words, to study the electron rescattering events occurring during photoionization and photorecombination. More specifically, the goals of this dissertation can be broken down into three sections: (1) observing vibrational mode-specific non-Franck-Condon behavior due to electron rescattering dynamics in low symmetry molecules, (2) disentangling the valence shell electronic structure of the pyrimidine-type nucleobases, and (3) using elliptically polarized light in high-order harmonic generation to probe electron rescattering events affecting photorecombination.

The first goal, observing vibrational mode-specific non-Franck Condon behavior, was addressed in Chapters 3 and 4; breakdown of the Franck-Condon Principle was studied for acrolein and the singly halogenated thiophenes. Specific vibrational branching ratios of acrolein's $\tilde{X}\ {}^{2}A'$ ionic state were affected by shape resonances during the photoionization process. With each of the singly halogenated thiophenes, 2-chlorothiophene, 3-chlorothiophene, 2-bromothiophene, and 3-bromothiophene, vibrational branching ratios for halogen-specific modes showed evidence of non-Franck-Condon behavior during photoionization leading to the $B\ {}^{2}A'$ ionic states likely due to a combination of resonant and non-resonant phenomena. Observing breakdown of the Franck-Condon principle, and thus a correlation between nuclear and electronic degrees of freedom, for specific vibrational modes in the photoionization of low symmetry molecules was shown to be feasible by the studies shown in Chapters 3-4 of this dissertation. Molecules have rich electron dynamics to be explored. For future work in this area, there are many more molecules to be studied, and, with the aid of scattering calculations, these particular dynamics may be further explored and explained. Studies of this nature are important in order to further the understanding of shape resonant electron trapping processes in molecules, and how such processes affect the chemical nature of molecules.

Chapters 5 and 6 of this dissertation addressed the second aim of these studies, disentangling the valence electronic structure of the pyrimidine-type nucleobases, thymine, uracil, and cytosine, using high-resolution photoelectron spectroscopy. These molecules are biologically relevant and, therefore, have been the focus of many previous studies. However, experimental determination of their electronic structures had been inconclusive until the studies presented in Chapter 5 were performed. The pseudo-Franck-Condon analysis of the nucleobases discussed in Chapters 5-6 of this dissertation, not only allowed for the binding energies of the electronic states to be determined, but it also provided experimental evidence of the low-energy shape resonances thought to be highly important in charge transfer processes through DNA. There is, however, plenty more to be done with the nucleobases experimentally.

From the data presented in Chapters 5-6, there is evidence of only one cytosine tautomer contributing to the photoelectron spectrum; however, it is not clear which of the five possible tautomers is the contributor. Again, the tautomerization of gas-phase cytosine has been studied previously, however there is much disagreement over which tautomers should be present, and dominant, at the temperatures used in these studies. Perhaps mass-spectrometry experiments on sublimated cytosine under similar conditions to the experiments presented in Chapters 5-6 could provide further evidence of the initial dimerization process which has been suggested to lead to the slightly less stable tautomers.[1] These experiments might also provide further insight to the appropriate ratios of cytosine tautomers under various temperature conditions.

Furthermore, there are still the purine-type nucleobases, adenine and guanine. While the electronic structure of adenine is relatively agreed upon, guanine has proven to be quite difficult to study, particularly in the gas phase. Running these high-resolution photoelectron spectroscopy experiments on guanine would require very tight control over the temperature of the setup, since guanine is less thermally stable in the gas-phase than the pyrimidine-type nucleobases. However, much like cytosine, the tautomerization of guanine is also not well understood. So, photoelectron spectroscopy experiments, like those described in Chapters 5 and 6 of this dissertation, on guanine could prove to be both interesting and useful to the scientific community.

The last goal, presented in Chapters 7-8, was using the polarization of the laser pulse during high-order harmonic generation (HHG) as a probe for electron rescattering events in atoms and molecules. This is of great interest since these rescattering events are known to impact HHG [2-9] and since currently there are no well-established probes for such processes in HHG. The results presented in Chapters 7 and 8 for atomic and molecular media are promising; however, it is important for theory to exist which takes into account electron rescattering dynamics for comparison purposes. Once a better theory is established to describe the harmonic response to increasing laser ellipticity, these experiments should be repeated for other molecular systems, both symmetric and also less symmetric, alignable systems. It would also be of great interest to repeat these experiments with an optical parametric amplifier, OPA, to extend the fundamental laser to longer wavelengths. At longer wavelengths, the spectral envelope would encompass higher energies enabling the analysis of harmonics in the regime of the Kr Cooper minimum or other higher energy electron rescattering dynamics.

The work presented in this dissertation explored electron rescattering dynamics during photoionization and photorecombination processes for both atomic and molecular systems. Photoionization studies were used to analyze vibrational-mode specific electron rescattering dynamics leading to correlations between electronic and vibrational motion for low symmetry polyatomic systems. Pseudo-Franck-Condon analyses of photoelectron spectra over a broad range of incident energies were used to disentangle electronic structural details of the pyrimidine-type nucleobases. As for photorecombination, data was presented for the use of laser ellipticity as a probe in the HHG process for electron rescattering dynamics in the medium. Running through all three of these subsets of projects is the common thread of photoelectrons’ entrance and exit of systems.

9.1 REFERENCES

[1] Z. Yang, M.T. Rodgers, Phys. Chem. Chem. Phys. 6 (2004) 2749.

[2] C.-G. Wahlstrom, J. Larrson, A. Persson, T. Starczewski, S. Svanberg, P. Salieres, P. Balcou, A. L'Huiller, Phys. Rev. A 48 (1993) 4709.

[3] H.J. Worner, H. Niikura, J.B. Bertrand, P.B. Corkum, D.M. Villeneuve, Phys. Rev. Lett. 102 (2009) 103901.

[4] J. Higuet, H. Ruf, N. Thire, R. Cireasa, E. Constant, E. Cormier, D. Descamps, E. Mevel, S. Petit, B. Pons, Y. Mairesse, B. Fabre, Phys. Rev. A 83 (2011) 053401.

[5] A.D. Shiner, B.E. Schmidt, C. Trallero-Herrero, H.J. Worner, S. Patchkovskii, P.B. Corkum, J.-C. Kieffer, F. Legare, D.M. Villeneuve, Nature Physics 7 (2011) 464.

[6] K.-H. Hong, C.-J. Lai, V.-M. Gkortsas, S.-W. Huang, J. Moses, E. Granados, S. Bhardwaj, F.X. Kartner, Phys. Rev. A 86 (2012) 043412.

[7] A.D. Shiner, B.E. Schmidt, C. Trallero-Herrero, P.B. Corkum, J.-C. Kieffer, F. Legare, D.M. Villeneuve, J. Phys. B.: At. Mol. Opt. Phys. 45 (2012) 074010.

[8] C. Trallero-Herrero, C. Jin, B.E. Schmidt, A.D. Shiner, J.-C. Kieffer, P.B. Corkum, D.M. Villeneuve, C.D. Lin, F. Legare, A.T. Le, J. Phys. B.: At. Mol. Opt. Phys. 45 (2012) 011001.

[9] M.C.H. Wong, A.-T. Le, A.F. Alharbi, A.E. Boguslavskiy, R.R. Lucchese, J.-P. Brichta, C.D. Lin, V.R. Bhardwaj, Phys. Rev. Lett. 110 (2013) 033006.

VITA

Kristen D’Ann Fulfer, a native of San Antonio, TX, received her bachelor’s degree in chemistry and mathematics at Texas State University - San Marcos in 2009. Thereafter, she made the decision to enter graduate school in the Department of Chemistry at Louisiana State University. She expects to receive her doctor of philosophy degree in May 2015.